Distribution Agreement

In presenting this thesis or dissertation as a partial fulfillment of the requirements for an advanced degree from Emory University, I hereby grant to Emory University and its agents the non-exclusive license to archive, make accessible, and display my thesis or dissertation in whole or in part in all forms of media, now or hereafter known, including display on the world wide web. I understand that I may select some access restrictions as part of the online submission of this thesis or dissertation. I retain all ownership rights to the copyright of the thesis or dissertation. I also retain the right to use in future works (such as articles or books) all or part of this thesis or dissertation.

Signature:

_____ _____

Kevin Yehl Date

Fundamental properties and applications of surface confined enzymes in gene regulation and molecular motors

By

Kevin Yehl

Doctor of Philosophy

Chemistry

_____

Khalid Salaita

Advisor

_____

David Lynn

Committee Member

_____

Vince Conticello

Committee Member

Accepted:

_____

Lisa A. Tedesco, Ph.D.

Dean of the James T. Laney School of Graduate Studies

_____

Date

Fundamental properties and applications of surface confined enzymes in gene regulation and molecular motors

By

Kevin Yehl

B.S. University of South Carolina, 2004

Advisor: Khalid Salaita, Ph.D.

An abstract of

A dissertation submitted to the Faculty of the

James T. Laney School of Graduate Studies of Emory University

in partial fulfillment of the requirements for the degree of

Doctor of Philosophy

in Chemistry

2015

Abstract

Fundamental properties and applications of surface confined enzymes in gene regulation and molecular motors

By Kevin Yehl

The vast majority of enzymes function in confined environments within or near lipid membranes, or within a supramolecular assembly containing many biomolecules. Examples range from receptor tyrosine kinases to motor proteins and the ubiquitous enzymes involved in DNA replication and protein synthesis. Confined enzymatic reactions are also widely employed in clinical chemistry and biotechnology. Despite its prevalence, we still have a limited ability to predict and control the properties of catalytic reactions upon confinement of the enzyme and substrate. The major goal of this thesis is to study the properties of confined catalytic reactions and to take advantage of insights for improved therapeutic and bio-sensing applications.

In Chapter 1, we describe the historical context and summarize representative literature on the topic of surface confined catalytic reactions. The chapter includes a discussion of general properties of catalytic reactions in comparison to solution, and the theoretical underpinning of differential properties on surfaces. Chapter 2 describes our efforts to develop and test model systems to study the impact of catalyst immobilization. DNAzymes, or catalytic oligonucleotides, were immobilized onto gold nanoparticles and used as a model system to study the effects of enzyme packing density and orientation, linker length and composition, and passivation on activity. From these findings, design rules were developed to synthesize highly active DNAzyme nanoparticles, which were shown to readily enter mammalian cells, possess enhanced nuclease resistance and

catalytic activity, and can regulate gene expression in a dose dependent manner. Importantly, in this chapter, we showed that DNAzyme nanoparticle conjugates down-regulate GDF15 mRNA expression by 60% in a cell culture model. GDF15 has clinical relevance for the treatment of many types of cancers, and particularly Herceptin® resistant metastatic breast cancer.

In Chapter 3, we expanded upon these studies in a more therapeutically relevant model to show that DNAzyme nanoparticles are highly modular and can regulate TNFα protein expression by targeting the corresponding mRNA in a rat model. The goal of these studies was to develop an anti-inflammatory therapy to prevent heart failure post cardiac infarction. The hypothesis was that the resulting tissue damage caused by cardiac infarction is due to an over-active immune response (up-regulation of TNFα), which could be minimized by down-regulating TNFα. We showed that DNAzyme nanoparticles targeting TNFα were more efficient when compared to siRNA or to antisense nanoparticles. In vivo experiments using a rat model of cardiac infarction showed that animals treated with DNAzyme nanoparticles targeting TNFα mRNA had a ~40% improvement in heart function, as determined by fractional shortening measurements of the rat's infarct tissue.

Chapter 4 describes the study of surface-immobilized catalytic reactions as models for molecular machines and motors. Following earlier results demonstrating the therapeutic potential of DNAzyme nanoparticles, we wondered how reactions would proceed if the substrate was surface immobilized. We anticipated that the particles would move along the surface to maximize Watson-Crick base pairing in a 'burnt bridge' mechanism of translocation. We chose to investigate the RNase H enzyme, which catalyzes the hydrolysis of RNA in RNA-DNA duplexes at orders of magnitude greater efficiency than DNAzymes.

In these studies, we showed that multivalent DNA modified particles (*diameter* = 5 μm, 10^7 DNA/particle) move along an RNA-monolayer surface in the presence of RNase H and translocate through a unique rolling mechanism. Thus, we termed these motors DNA monowheels (DMWs). This unique mechanism of translocation produces emergent properties enabling the motors to reach rapid speeds up to 5 μm/min and processivity of several hundreds of μm's, thus surpassing the fastest synthetic DNA-based motor by three orders of magnitude and approaching the capabilities of biological motor proteins. Interestingly, these motors displayed the first experimental example of self-avoiding diffusion. Due to the rolling mechanism of motion, we were able to program DMWs to move in a linear fashion by incorporating anisotropy into the particle "chassis" structure. Accordingly, this was the first example of directional motion without the influence from an external field or patterned track. Because of the motor robustness, size, and molecular sensitivity, we showed that DNA monowheels could be used to detect single nucleotide mutations using a simple smartphone readout, thus demonstrating the simplicity and usefulness of DNA-based motors towards real world applications.

Finally, Chapter 5 provides a perspective discussing the potential for studying confined multi-enzyme model systems to more accurately recapitulate living systems. Such constructs are anticipated to have emergent, synergistic properties that impact the fields of sensing and gene editing technologies.

Fundamental properties and applications of surface confined enzymes in gene regulation and molecular motors

By

Kevin Yehl

B.S. University of South Carolina, 2004

Advisor: Khalid Salaita, Ph.D.

A dissertation submitted to the Faculty of the

James T. Laney School of Graduate Studies of Emory University

in partial fulfillment of the requirements for the degree of

Doctor of Philosophy

in Chemistry

2015

Acknowledgements

First and foremost, I thank my advisor Khalid Salaita. He accepted me into his group in his first year as a professor and entrusted in me that I could play an integral part in jump starting his lab. This confidence and his resounding support has further instilled my passion for science, which I am ever grateful for. In addition, his patience, creativity, and most importantly, his enthusiasm has provided excellent mentorship and is what has shaped me into the scientist I am today and will become. I also thank my committee members Professors David Lynn and Vince Conticello for their support and always offering advice and challenging me to think about my research from different perspectives. Also, a special thanks to Professor David Lynn for allowing me a rotation in his lab and exposing me to extremely exciting science. I also thank the other Professors that have allowed me to conduct exciting research in their labs as well during my scientific career, Professors Ken Shimizu, Stefan Kubik, Stefan Lutz, and Xiaogang Liu.

As for previous and current lab members, I thank you for being patient with my singing, dancing, and joking, but most importantly, thank you for making lab a fun place to go. Special thanks to lab members that have been with me from the very beginning, Daniel Stabely, Carol Jurchenko, Yoshie Narui, and Yang Liu. Your friendship, work ethic, and assistance has proven invaluable throughout this process. Special thanks to Yang Liu and Kornelia Galior for our scientific discussions, collaborations, hot pot dinners and tennis lessons. Also, thanks to all other lab friends, Yun Zhang, Yuan Chang, Dr. Weiwei Zheng, Dr. Zheng Liu, Victor Ma, Jessica Petree, Josh Brockman, Roxanne Glazier, Han Su, and Edward Fan. I am continually impressed with your talents and am excited to see the

directions you take the lab. Also, special thanks to people behind the scenes that have helped and influenced me along the way, Ann Dasher, Steve Krebs, Patti Barnett.

I would also like to thank the friends I have made during this process. Ashly and Michael Daugherty for our dinner parties, Brandon Greene for "our" brewing sessions, Eric Miller for our soccer games and delicious hospital lunches, and Jim Vickers for keeping it strange and awesome. Without amazing friends like you, succeeding in this process would not be possible.

I especially thank my family for their continual love and support. You have played major roles in directing me towards this degree. Specifically, my twin brother Chris's early passion (6 years old) towards archeology and astronomy, which first peaked my interest towards science; my Uncle Jim for coming up with homework assignments when I "accidentally" left my homework from primary school; my parents for their passion towards education which was evident by the multitude of science magazines lying around, long nights helping me with science fair projects, and supporting me to go to science camps; my sister Jennifer for being my tutor for intro biology; my older brother Michael for being an excellent role model and convincing me to major in chemistry and conduct undergraduate research; my step brothers and sisters for their support; and most importantly to a future family member and best friend, Erin Schuler, for your unconditional love, support, and enthusiasm in helping us in fulfilling our life's passions and achieving our fullest potential.

List of Frequently Used Abbreviations

Abbreviation	Full Name
BHQ™	black hole quencher™
DMW	DNA monowheel
DTT	dithiothreitol
Dz	deoxyribozyme
DzNP	deoxyribozyme gold nanoparticle
FAM6	6-fluorescein
GDF15	growth differentiation factor 15
HER2	human epidermal growth factor receptor 2
RNase H	ribonuclease H
RNase A	ribonuclease A
RPLPO	human large ribosomal protein
siRNA	short interfering RNA
TGF-β	transforming growth factor β
TNF-α	tumor necrosis factor α

Table of Contents

List of Figures

List of Tables

Chapter 1: Properties and applications of surface confined enzymes

1.1 Introduction

1.1.1 Prevalence throughout biology

In living systems, many chemical reactions occur at surfaces or in confined spaces, such as the plasma membrane and cell wall or within organelles. In fact, nearly a third of all proteins are predicted to be associated with biological membranes.[1] This is important because enzyme confinement can lead to drastically different properties compared to their soluble counterparts; altered substrate selectivity, increased stability, and even increased activity. Surface confinement of enzymatic reactions enables important biological functions, ranging from energy production, cellular motility, and metabolite synthesis, and such mechanisms may impact fields ranging from biomedical sensing to therapies and renewable energy. Realizing this potential, many groups have studied surface confined enzymatic reactions as early as the 1950's, however, the consequences of confinement are still difficult to predict *a priori*.[2] Development of model systems giving mechanistic insights is needed in order to provide design rules to develop next generation technologies. The following sections will discuss: (1) the general features of surface-confined enzymatic reactions as gleaned from studying model reactions. This section will put into perspective why it is difficult to predict enzyme activity upon immobilization. (2) Applications involving surface confined reactions with a particular emphasis on synthetic motors. Finally the chapter will conclude with a statement of the aim and scope for this thesis.

1.2 Theory on surface confinement of enzymatic reactions

Enzyme confinement can be defined as an enzymatic chemical reaction occurring at a surface. This can be achieved through immobilization of either the enzyme or substrate

(**Figure 1.1**), which can have its own advantages or disadvantages depending on the application.[3]

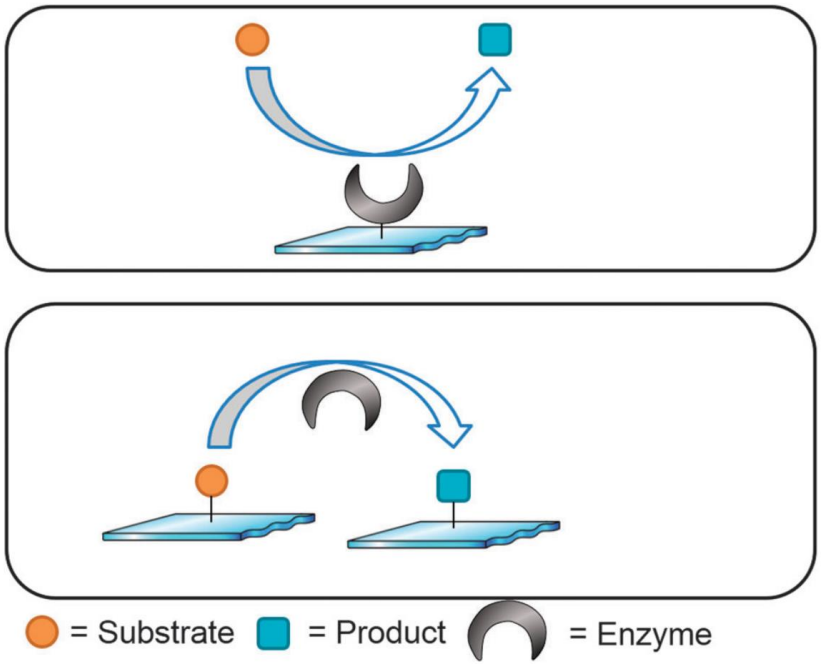

Figure 1.1. A schematic illustrating the two approaches to confine enzymatic reactions, which involve enzyme (top) or substrate (bottom) immobilization. Reprinted from Reference 3 with permission from the publisher.

1.2.1 Immobilization techniques

To date, there are many methods available to immobilize enzymes or substrates onto solid supports, which can be organized into two general classes, non-covalent or covalent attachment.[4] Both strategies have their own merits and limitations. The non-covalent approach, where an enzyme is simply adsorbed onto a surface, is a simple functionalization technique and immobilizes the enzyme to the surface through multiple contacts along the enzyme structure. This can lead to an enhancement in enzyme stability; however, there is limited control over enzyme orientation. For example, if both the catalytic core of the enzyme and the surface are hydrophobic, then the enzyme will be bound to the surface through van der Waals interactions in an orientation inhibiting substrate binding (**Figure**

1.2a).[5] However, there are other supports that can be used depending on the enzyme being immobilized. For example, dextran or ionic supports would be more optimal for immobilizing an enzyme with a hydrophobic core because the enzyme would be immobilized through hydrogen bonding or ionic interactions, thus likely orienting the catalytic core to enable substrate binding (**Figure 1.2b,c**).

Covalent immobilization is a more complicated approach but can allow for greater control over enzyme orientation, especially if the enzyme is site-specifically immobilized to the surface using a heterobifunctional linker (**Figure 1.2d**). However, if an enzyme contains multiple reactive sites, then multiple orientations are possible. Otherwise, tedious protein engineering is required to either incorporate a site specific tag or mutate out all other non-specific immobilization sites. If enzyme mutations are made, then additional tests are needed in order to verify that the modifications do not denature the enzyme and alter its function. However, many groups are working on methods to streamline approaches to easily incorporate site specific modifications with minimal structural perturbations.[6-8]

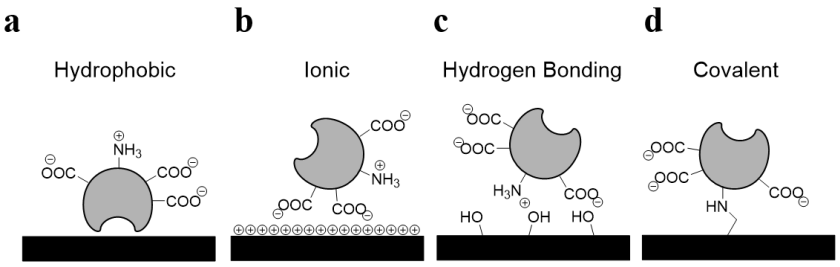

Figure 1.2. Schematic illustrating the various strategies and orientations a surface confined enzyme can have depending on the method.

1.2.2 Stability

Typically, when enzymes are immobilized, they become more stable to thermal or chemical denaturation. There has been a correlation between increased enzyme stability

and the rigidity of enzyme immobilization, which can be controlled through adjusting the number of contacts between the enzyme and surface or immobilizing the enzyme using short rigid linkers.[9,10] However, both strategies typically lead to a decrease in enzyme activity. This can be attributed to stabilizing the enzyme structure through contribution of additional enzyme-surface contacts that have to be disrupted in order to unfold the enzyme. However, if these interactions are too strong, they can denature the enzyme as well. In addition to stability against denaturation, enzymes that are surface confined are typically more resistant against hydrolytic enzymes. This is due to a combination of factors, which include inhibition of the hydrolytic enzyme caused by the local micro-environment and requiring greater energy to unfold the surface immobilized enzyme into the active conformation required for hydrolysis. Because of these effects, enzymes have been shown to improve up to five orders of magnitude in stability due to surface confinement.[10,11]

1.2.3 Enhanced catalysis

In some cases, surface immobilizations can even enhance enzyme activity, although this is more the exception than the rule.[12] A major goal in the field is to rationally design such systems as opposed to fortuitously discovering them. For this to be achieved, a better mechanistic understanding into why certain enzymes gain activity when immobilized is required. Enhancement in activity can be caused by various mechanisms or a combination of them. The most common mechanism is alteration in the local micro-environment.[2] Changes in the micro-environment can adjust the local pH of catalytic residues to a more optimal regime.[13] In addition, the solid support can have weak interactions with the substrate to increase the effective local substrate concentration, resulting in an improved binding constant.[14] However, if the surface repels the substrate or binds too strongly with

the product, an inhibitory effect can be observed. Another factor that can improve enzyme function is alteration in enzyme structure caused by surface immobilization.[2] For example, lipase enzymes require a conformational change involving opening of a peptide lid to switch the enzyme into the active form. Depending on the solid support, when lipases are immobilized, the enzymes are locked into the active state, thus enhancing activity.[15] Enzyme or substrate valency can also have a profound effect on activity.[3,16,17] Increasing enzyme valency typically slows down k_{off} but increases substrate affinity, which in turn can enhance catalysis.[18] In addition, increasing substrate valency typically leads to an improvement in enzyme processivity.[16] Many signal amplification strategies have been designed around this phenomenon.[3,16] However, there is typically an optimal density before steric inhibition occurs, resulting in a bell-shaped trend for enzyme activity as a function of enzyme density.[19] Most commonly, what is thought to be enhancement in enzyme activity is actually due to an increase in enzyme stability from immobilization, where the soluble form is easily denatured or degraded. For example, immobilization of trypsin, a protease enzyme, prevents self-degradation and can lead to up to a10^5 fold enhancement in stability.[11]

1.3 Prevalence of surface confined enzymatic reactions

1.3.1 Industry

Enzyme confinement has had a major impact on industrial processes.[20] The first example of using immobilized enzymes for a commercial process was in the late 1960s by a Japanese company where they immobilized l-amino acid acylase for the production of l-amino acids from a mixture of racemic amino acid derivatives.[21] Surface immobilization of the enzyme provided significant improvement in enzyme stability and also allowed

facile separation of the enzyme from the reaction mixture so that it could be cycled many times. Since this development, immobilized enzymes have been incorporated into many industrial processes, ranging from food processing where pectinases are used to break down complex polysaccharides to remove bitter tastes, all the way to the pharmaceutical and pesticide industry, where enzymes are especially valuable because of the increased regulations requiring production of enantio-pure compounds.[20] In order to fully appreciate the prevalence of surface confined enzymes in industrial processes, **Table 1.1** summarizes some of the best-known examples.

Large scale industrial processes utilizing immobilized biocatalysts

Enzyme	Form[a]	Process	Product scale (ton per year)
Glucose isomerase	CWC, IME, CIE	High fructose corn syrup from corn syrup	10^7
Nitrile hydratase	CWC	Acrylamide from acrylonitrile	10^5
Lipase	IME	Transesterification of food oils	10^5
Lactase	IME	Lactose hydrolysis, GOS synthesis	10^5
Lipase	IME	Biodiesel from triglycerides	10^4
Penicillin G acylase	CIE	Antibiotic modification	10^4
Aspartase	CWC, IME	L-Aspartic acid from Fumaric acid	10^4
Thermolysin	IME	Aspartame synthesis	10^4
Lipase	IME, CIE	Chiral resolution of alcohols and amines	10^3

[a] CWC = cross-linked whole cell; IME = immobilized enzyme; CIE = covalently immobilized enzyme.

Table 1.1. A table summarizing the large scale industrial processes that involves surface confined enzymes. Reprinted from Reference 20 with permission from the publisher.

1.3.2 Bio-medical Applications

Surface confined enzymatic reactions have been key to revolutionizing the bio-medical sciences. For example, enzyme-linked immunosorbent assay (ELISA) is a surface confined enzymatic reaction that allows for facile detection and amplification of analytes (**Figure1.3a**).[22] This technique has been the major workhorse for cell biology labs and has been incorporated into many commercial sensing platforms to detect and track the spread of diseases (*i.e. AIDS, West Nile, Ebola…*). In addition, glucose sensors require immobilized glucose oxidase to quantify levels of glucose in the blood (**Figure 1.3b**). This

quantification is crucial for diabetic patients in regulating insulin intake in order to prevent hyperglycemia. Moreover, many groups are working to expand the scope for this sensing platform to detect a host of other analytes.[23,24] This in turn will allow onsite detection as opposed to sending samples away to a centralized lab, which can take days to analyze the results. DNA sequencing is another field that has been revolutionized by surface confined enzymatic reactions. DNA sequencing is crucial for bio-medical research, in addition to a range of other applications, such as medical diagnosis, virology, and forensics. Next generation sequencing technology relies on sequencing by synthesis approach, which involves a polymerase to synthesize a DNA template immobilized to a surface or bead.[25] One of the more promising technologies is pyrosequencing illustrated in **Figure 1.3c**, where DNA sequences are processed and immobilized onto micro-beads that are confined to microchannels. By flowing a solution of base monomers over the microchannels, base coupling can be detected through the pyrophosphate byproduct, which is a substrate for an enzymatic cascade that produces light. Therefore, the DNA sequence can be determined depending on which monomers produce light.[25]

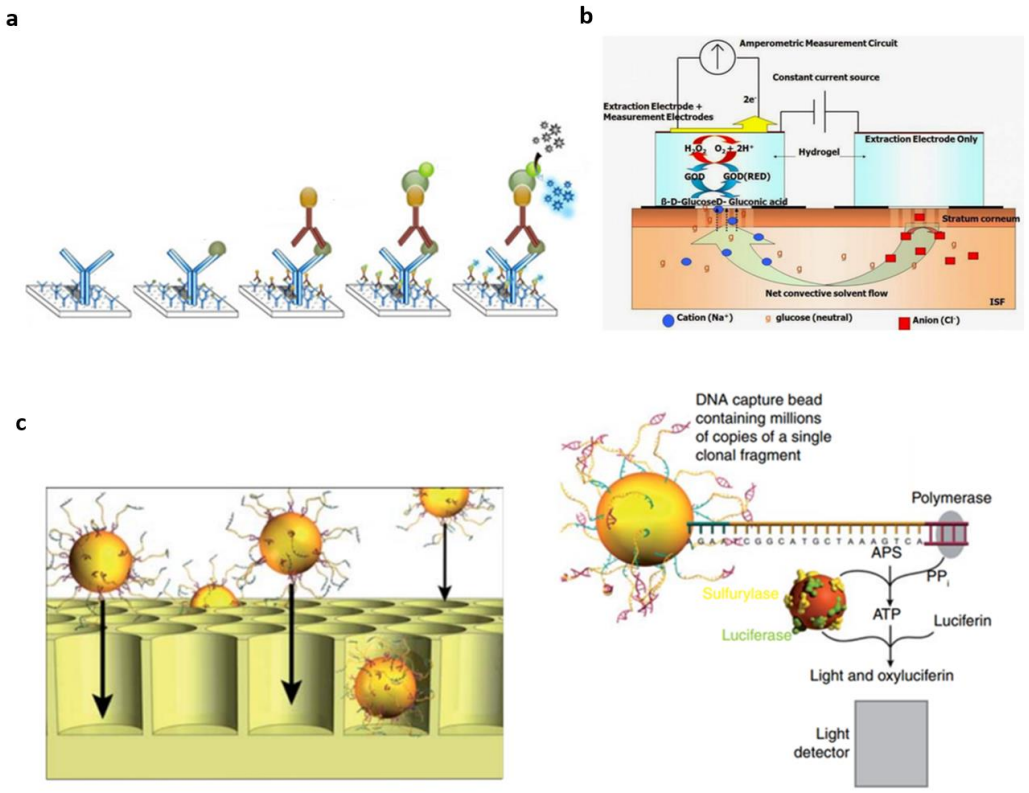

Figure 1.3. Schematic illustrations of important biotechnologies that utilize surface confined enzymes; ELISA (**a**), glucose sensors (**b**), and next generation DNA sequencing (**c**). Reprinted from References 22, 24, and 25 with permission from the publisher.

1.3.3 Synthetic Motors

Biological motor proteins are required for all living systems and involve surface confined enzymatic reactions. Specifically, higher order organisms require proteins that walk along filamentous tracks to produce force or deliver cargo. These proteins are quite spectacular in that they dynamically alter their interaction with the track through conformational changes coupled to ATP hydrolysis. This enables directional motion for several microns at rapid micron per second velocities. Replicating such function is a fundamentally challenging problem and holds great potential to revolutionizing several fields.

1.3.3.1 Seminal studies

To date, the most promising systems involve DNA-based motors, owing to their predictable and tunable Watson-Crick base pairing. Monumental studies carried out by Seeman and Pierce et al. first demonstrated that synthetic motors powered by DNA hybridization can attain molecular control of motion against the entropy of random Brownian diffusion (**Figure 1.4a, b**).[26,27] In fact, these motors were shown to perform useful work by assembling nanoparticles together across a nano-assembly line (**Figure 1.4c**).[28] These exciting results have led to many conceived applications ranging from bottom up assembly of commercial products with atomic level precision; nanoscale chemical reactors that can synthesize complex molecules through proximal arrangement of reactive groups; actuating materials that possess functions similar to that of muscles; and intelligent therapeutics able to seek, recognize, and treat diseased cells.

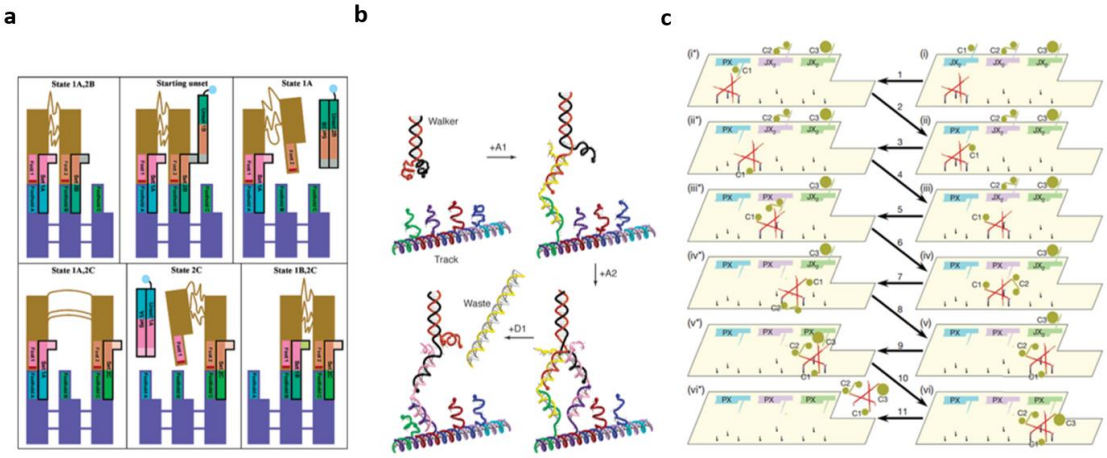

Figure 1.4. Schematic showing the design for the first molecular motors that can move unidirectionally. These motor are powered by DNA hybridization through sequential addition of specific fuel strands that release or bind the foot to the track causing a single step forward in an inchworm fashion (**a**) or an arm over arm mechanism (**b**). (**c**) Schematic of a DNA walker used to assemble nanoparticles to perform useful work. Reprinted from References 26-28 with permission from the publisher.

However, these initial molecular motor prototypes are not autonomous, which significantly limits their usefulness. Addressing this concern, the groups of Pierce, Seeman and Turberfield designed motors that can move autonomously using hairpin DNA fuel (**Figure 1.5**).[29-31] This elegant design enables temporal control of cascading reactions (i.e. fuel consumption) that is initiated by the progress of the DNA motor along the track. The hairpin structure inactivates the fuel strand, such that it can only be activated and consumed upon the progress of the motor along the track, resulting in exposure of an activation sequence. Though autonomous, these motors are slow and limited by the amount of useful work that can be performed. However, motors powered by surface confined enzymatic reactions can address this concern and represent the most promising approach to fully realizing the potential of molecular motors.

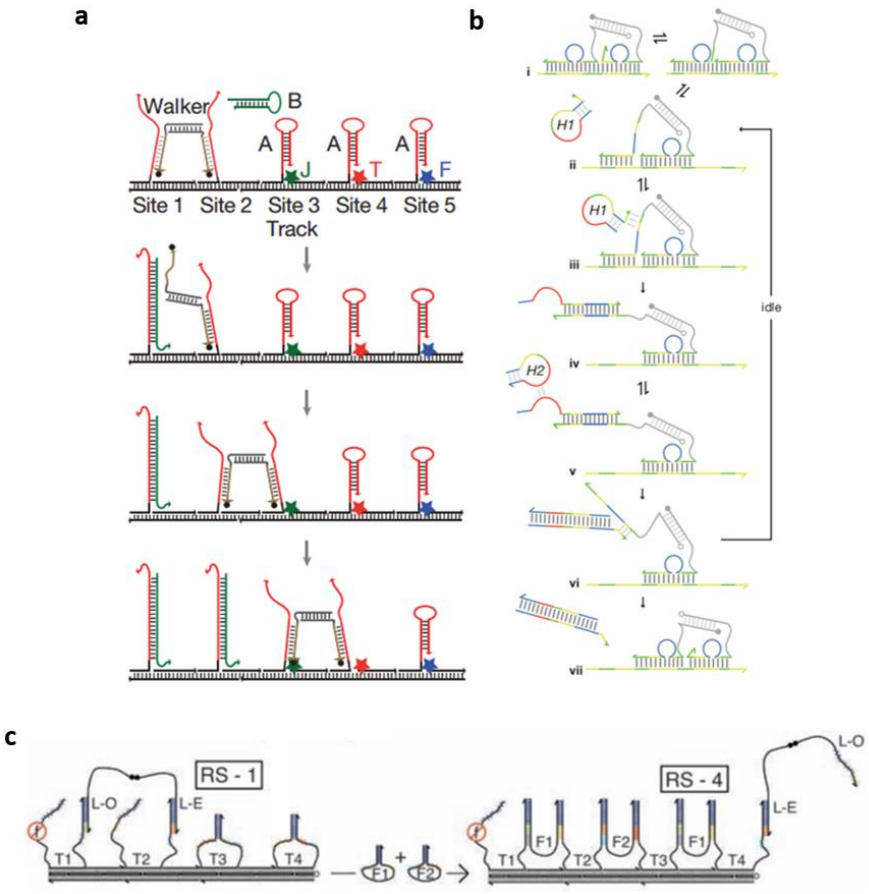

Figure 1.5. Schematic illustrations showing the design of autonomous DNA motors powered by DNA hybridization with hairpin fuel with uncoordinated (**a**) or coordinated (**b** and **c**) feet motion. Adapted with permission from References 29-31.

1.3.3.2 Role of surface confined enzymatic reactions on the progress of molecular motors

1.3.3.2.1 Burnt bridge mechanism

Inspired by the fact that motor proteins are fueled by ATP hydrolysis, many groups have designed autonomous synthetic motors fueled by phosphodiester hydrolysis.[32-40] Of this class, two approaches have been devised involving either DNAzyme or endonuclease surface confined catalysis. The general principle responsible for autonomous and directional motion for these motors is the "burnt bridge" mechanism, where the track is selectively hydrolyzed only where the motor is bound, thus biasing motor diffusion toward the non-hydrolyzed sections of the track.[41] It is important to note that even though phosphate hydrolysis powers motor translocation, these motors are significantly different than their motor protein counterparts in that motor proteins do not destroy their tracks. Despite these differences, these DNA-based motors offer capabilities that can greatly complement biological motor proteins such that they can individually be programed to carry out specific tasks. Also, since the fuel is the track itself, this design no longer necessitates the need for soluble fuel and therefore increases motor efficiency. The following section will focus on approaches undertaken using DNAzyme based motors, whereas the subsequent section will discuss endonuclease-powered motors.

1.3.3.2.2 DNAzyme based motors

DNAzymes are catalytic sequences of DNA that can catalyze a variety of chemical reactions.[42,43] In the context of DNA-based motors, DNAzymes specific for the hydrolysis of RNA are typically used.[33,35,36,40] For example, Chengde Mao et al. developed the first

DNAzyme based motor where DNAzyme 10-23 was designed to translocate three steps along a DNA scaffold track containing pendant DNA-RNA chimera footholds (**Figure 1.6a**).[33] DNAzyme 10-23 is a Mg^{2+} dependent DNAzyme possessing a 15 *bp* catalytic core responsible for RNA hydrolysis and is flanked by two recognition arms to allow for programmable selectivity. The monopod motor was designed to possess asymmetric recognition arms (*upper* = 7; *lower* = 15) such that the lower arm relative to the track contains a longer recognition sequence compared to that of the upper arm. This design enables motor association with the track and rapid dissociation of hydrolyzed product from the upper arm of the DNAzyme. The resulting free upper arm is then able to hybridize with the adjacent foothold to initiate a strand displacement reaction. Cycling between these two reactions (hydrolysis and strand displacement) autonomously progresses the DNAzyme along the track in an inchworm type mechanism (**Figure 1.6b**).

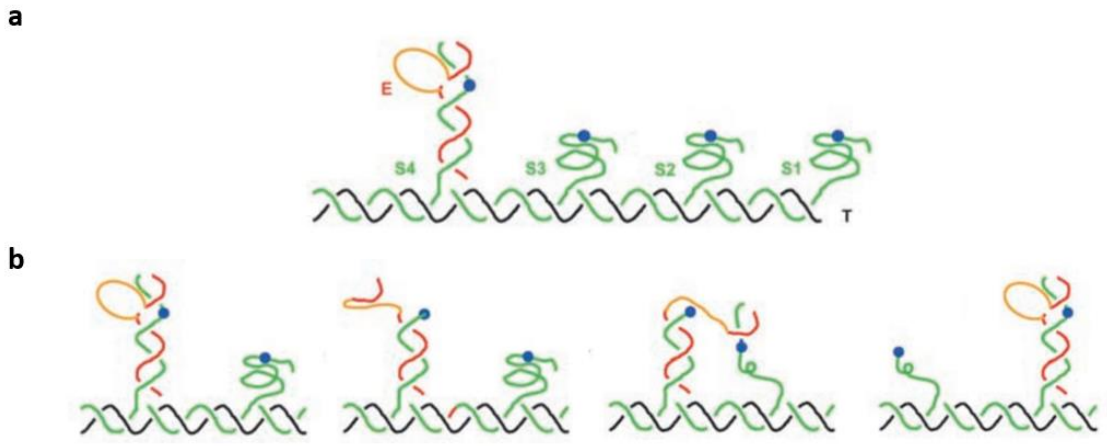

Figure 1.6. (**a**) DNAzyme based motor and track design. (**b**) The translocation mechanism for the DNAzyme motor where the DNAzyme hydrolyzes the fuel templated along the track. Hydrolysis leads to product release and strand displacement with adjacent foothold to progress the motor along the track in an inchworm fashion. Reprinted from Reference 33 with permission from the publisher.

Independently, Milan Stojanovic et al. studied how DNAzyme multivalency affects motor catalytic efficiency.[35] Using a streptavidin chassis, they synthesized motors varying in the number of 8-17 DNAzyme legs (l = 1-6) and lengths of the recognition sequence (d = 14-18 *bp*) (**Figure 1.7a**). These motors were termed molecular spiders due to their proposed stepping mechanism and "resemblance" to spiders. To measure the catalytic efficiency for various molecular spiders, they monitored the rate of hydrolysis of a high density of substrate immobilized to a 3D dextran matrix using surface plasmon resonance. They conclude that the motors possessed biased diffusion and found that an increase in leg number and duplex length increases motor processivity, yet decreases catalytic rate. This was determined by monitoring the rate of RNA hydrolysis under flow conditions, where the non-processive motors were washed away (**Figure 1.7b**). However, they were unable to directly monitor motor displacements due to the limited resolution.

In a highly collaborative study, Milan Stojanovic, Nils Walter, Erik Winfree, and Hao Yan et al. expanded upon these findings by individually tracking molecular spider displacements and showed that molecular spider motors do possess biased diffusion that is dictated by the pattern of the track (**Figure 1.7c**), thus validating theory regarding diffusion of molecular spider motors.[36,44] Here they monitored the progress of molecular spiders along variously patterned DNA origami tracks using real-time AFM or super resolution fluorescence TIRF imaging. They found that the molecular spiders could "crawl" from start to finish at speeds approximately 3 nm/min at ~60% fidelity. Impressively, this landmark study shows that robot algorithms can be programmed into substrate patterned tracks to be carried out by the molecular spider robots, though the efficiency, speed, and fidelity need to be greatly optimized for future applications.

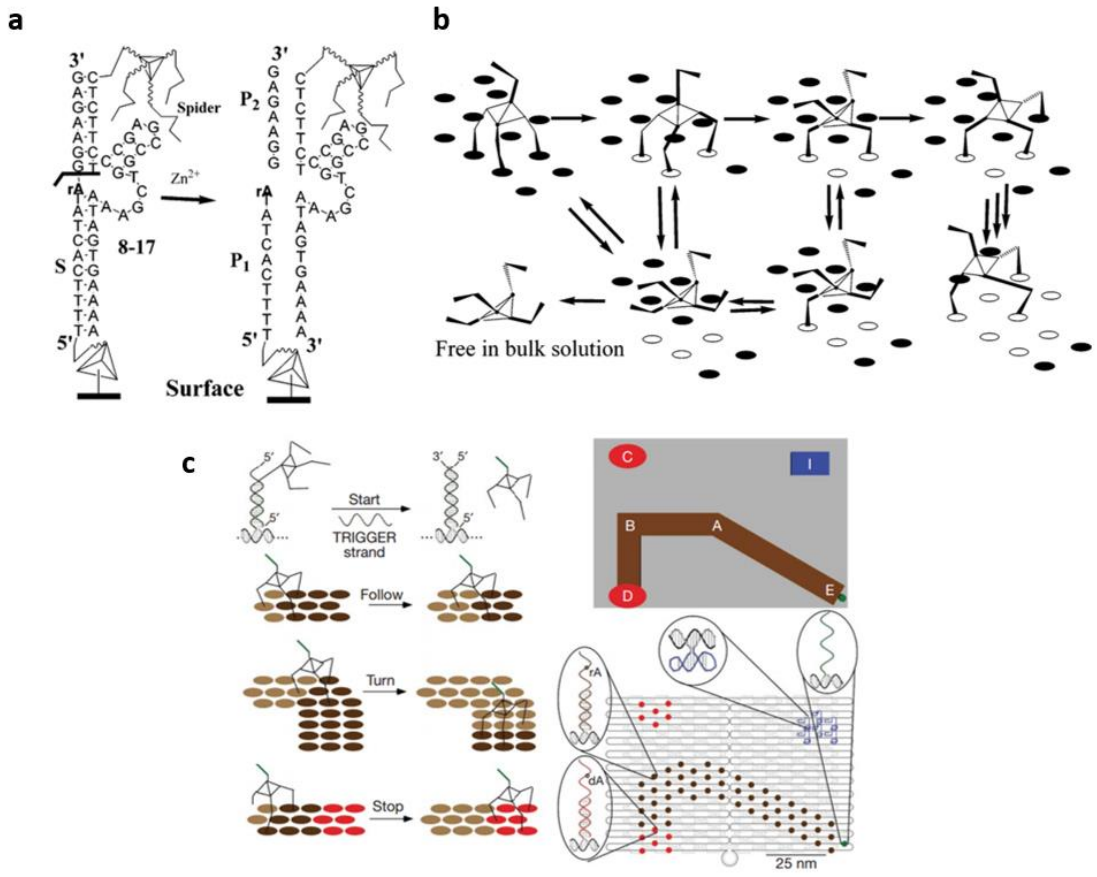

Figure 1.7. (**a**) Hydrolysis of the surface immobilized DNAzyme substrate by the DNAzyme-based molecular spider, which is composed of four DNAzyme legs immobilized to a streptavidin body. (**b**) The proposed stepping mechanism for the DNAzyme-based molecular spider. (**c**) Molecular spider traversing a DNA origami template prescriptive landscape. Reprinted from References 35 and 36 with permission from the publisher.

To determine the distance that DNAzyme based motors can travel and to demonstrate that DNAzyme based motors are capable of doing useful work, akin to that of biological motor proteins, Jong Choi *et al.* tracked 10-23 DNAzyme coated quantum dots walking along substrate functionalized carbon nanotube tracks (**Figure 1.8**).[40] They found that the particle velocities and the distances traveled did not change when varying the number of DNAzymes per particle (2-30), so a single DNAzyme motor was likely responsible for

moving the particle along the track. Under optimal conditions ([Mg^{2+}] = 100 mM and pH = 8), Jong Choi et al. showed that DNAzyme motors can translocate QD cargo ~1 µm over 24 hours, which corresponds to an average velocity of ~1 nm/min. Surprisingly, DNAzyme motors even in the absence of divalent metal ions and in the presence of 100 mM K^{+} were also highly processive, traveling µm distances but at 3 fold lower velocities (0.3 nm/min). The two key experimental designs allowing Jong Choi et al. to determine how far DNAzyme based motors can walk was (1) the stability of the QD fluorescence allowing for long term tracking, which is required due to the slow motor velocities, and (2) the high aspect ratio of the tracks, where the tracks are several µm's long yet tens of nanometer in diameter. Importantly, these set of studies show that autonomous DNA-based motors can translocate particle cargo distances greater than that of DNA origami tiled tracks, thus achieving useful work.

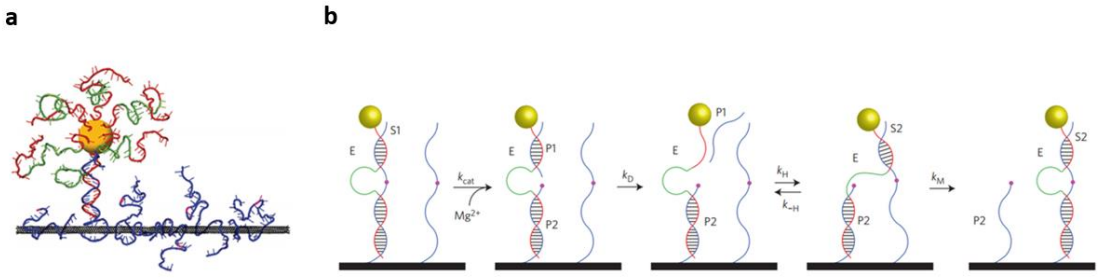

Figure 1.8. (**a**) DNAzyme driven translocation of a quantum dot cargo along a substrate functionalized carbon nanotube track. (**b**) Translocation mechanism of the DNAzyme functionalized quantum dot. Reprinted from Reference 40 with permission from the publisher.

Translating DNA motors beyond being a model system for studying motor proteins is a major goal and hurdle in transforming the field of DNA-based machines to the next stage of development. David Liu et al. has highlighted one such potential application using DNA-

based motors, where DNAzymes were shown to synthesize an oligoamide polymer with single monomer resolution by translating a DNA template sequence (**Figure 1.9**).[37] Specifically in this proof-of-concept study, David Liu et al. showed that an autonomous DNAzyme motor with a terminal amine group can walk along a DNA duplex track containing three substrate footholds, where the foothold substrates were functionalized with pendant NHS ester functionalized monomers. Motor translocation resulted in catalysis and polymerization of the oligoamide through arranging the reactive groups in close proximity, resulting in 45% polymer yield. The key design for this system is that the coupling reaction is faster than the motor velocity. Conveniently, DNAzyme motors are highly tunable in that the velocity can easily be tailored towards a specific polymer. This landmark study demonstrates that DNA motors have the capability of translating information from a DNA polymer track into another polymer, thus functioning as a DNA ribosome, hence why David Liu et al. termed the motor a DNAsome. However, as the polymer chain grows, the accuracy for arranging the reactive groups significantly diminishes, which next generation DNAsomes will need to address in order to evolve these motors into functional technologies.

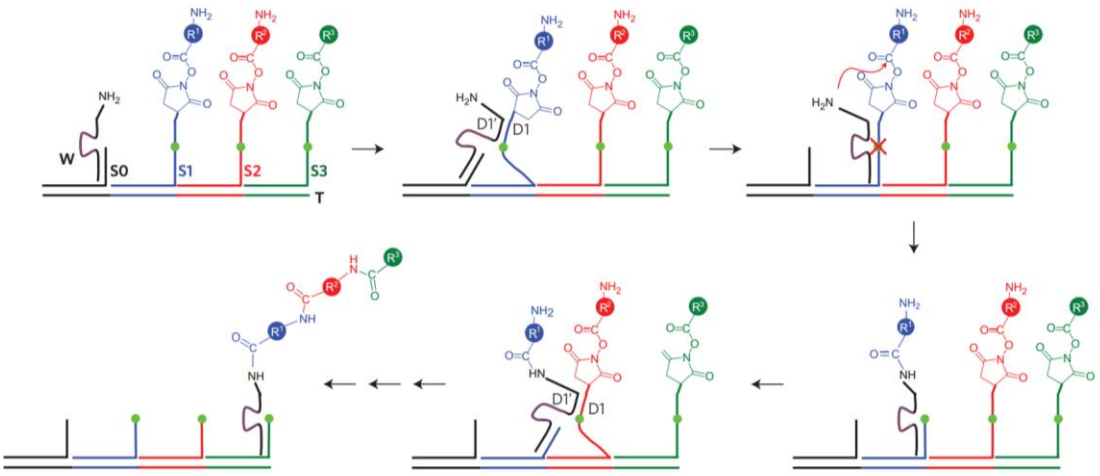

Figure 1.9. A DNAzyme based motor (DNAsome) programmed to synthesize a polymer in a sequence specific manner by walking along a substrate templated track. Reprinted from Reference 37 with permission from the publisher.

1.3.3.2.3 Endonuclease powered motors

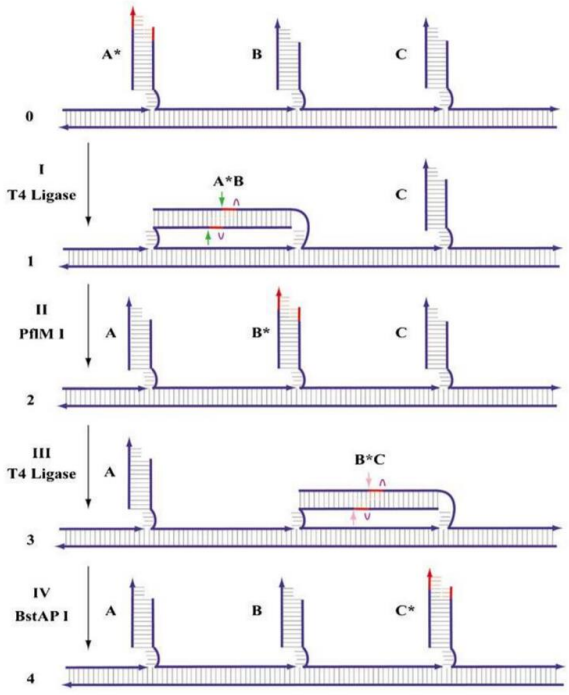

Figure 1.10. Design of the first autonomous DNA-based motor that is enzymatically powered by both ligase and endonuclease enzymes. Reprinted from Reference 32 with permission from the publisher.

Using soluble, biological enzymes to power nano-mechanical devices (rather than DNAzymes) offers significant benefits, such as 1) superior enzyme efficiency 2) separating the force-generating machinery from the nano-device, and 3) allowing for the potential to integrate nano-devices with biological systems. The first demonstration of this principle was developed by the groups of Hao Yan, Andrew Turberfield, and John Reif, where the translocation of a DNA motor along a track was powered by both ligase and endonuclease enzymes requiring ATP as fuel (**Figure 1.10**).[32] In this design, the DNA walker consists of a recognition sequence for the T4 ligase and the PflM I and BstAP endonucleases. The track that the nano-device moves along is comprised of three DNA duplex anchorage sites that are evenly spaced along a DNA duplex scaffold and are connected to the scaffold through a single stranded hinge region. Each duplex anchorage site possesses a ssDNA sticky overhang that is complementary to

the monopod motor. In the presence of T4 ligase and ATP, the DNA motor is ligated to the adjacent anchorage site, thus forming a continuous duplex that contains the recognition sequence for PflM I endonuclease. Upon endonuclease hydrolysis, the DNA walker is released from the first anchorage site and steps to the adjacent site. This process is repeated to move the walker to the final site but instead using the BstAP endonuclease. In principle, this motor can transverse much longer distances only limited by enzyme efficiency and track length. However, for these studies, they only designed the motor to take two steps, which was only 25% efficient (determined by a series of gel shift assays). Though the efficiency is low, this study is a milestone in the DNA-based motor field in that it is the first example of autonomous, linear motion of a nano-mechanical device.

Simplifying this approach, Turberfield et al. designed a motor that can autonomously move along a DNA track through a burnt bridge mechanism powered by only an endonuclease enzyme (**Figure 1.11a**).[34] Upon hybridization to the track, the DNA machine in conjunction with the N.BbvC IB endonuclease is able to selectively catalyze the hydrolysis of the complementary track foothold, which Turberfield et al. terms the 'stator'. N.BbvC IB is an engineered restriction enzyme that recognizes a 7 base pair sequence that selectively nicks the complementary stator strand. This hydrolysis event leads to release of the top half of the hydrolyzed product relative to the track resulting in an exposed toehold overhang, which can catalyze the strand displacement reaction with the adjacent stator strand. This sequence of reactions are repeated such that the DNA cargo can walk to the third and final stator of the track, containing a single base mutation to inhibit N.BbvC IB hydrolysis and trap the motor. The processive motion and motor velocity was quantified through a kinetic fluorescence assay, where the DNA machine was labeled with a quencher

and the stator overhangs labeled with spectrally distinct fluorophores. The florescence kinetic assay showed sequential quenching and fluorescence recovery corresponding to the fluorophore position along the track. The fitted rates of the kinetic assay equated to the DNA monopod traveling at speeds of ~5 nm/min.

Turberfield et al. expanded upon these findings to show that an endonuclease powered monopod motor can walk much longer distances using a DNA origami track possessing 16 stator strands in a line, equating to ~100 nm in length.[38] Using real time AFM, Turberfield et al. showed direct stepwise movement of the DNA motor along the track where 35% of the motors were able to walk the full ~100 nm length at an average velocity of ~5 nm/min. In addition to demonstrating that endonuclease powered monopod motors can transverse long, linear distances, Turberfield et al. also showed that this class of motor can navigate a network of tracks.[39] In this study, they showed that the motor can correctly choose the desired path either through external control through addition of oligonucleotide cues at ~90% efficiency or internal control by the motor itself at ~70% efficiency. Similar to the molecular spiders, programmable motion allows for cargo sorting, molecular computing, and dynamic networks for assembly lines.

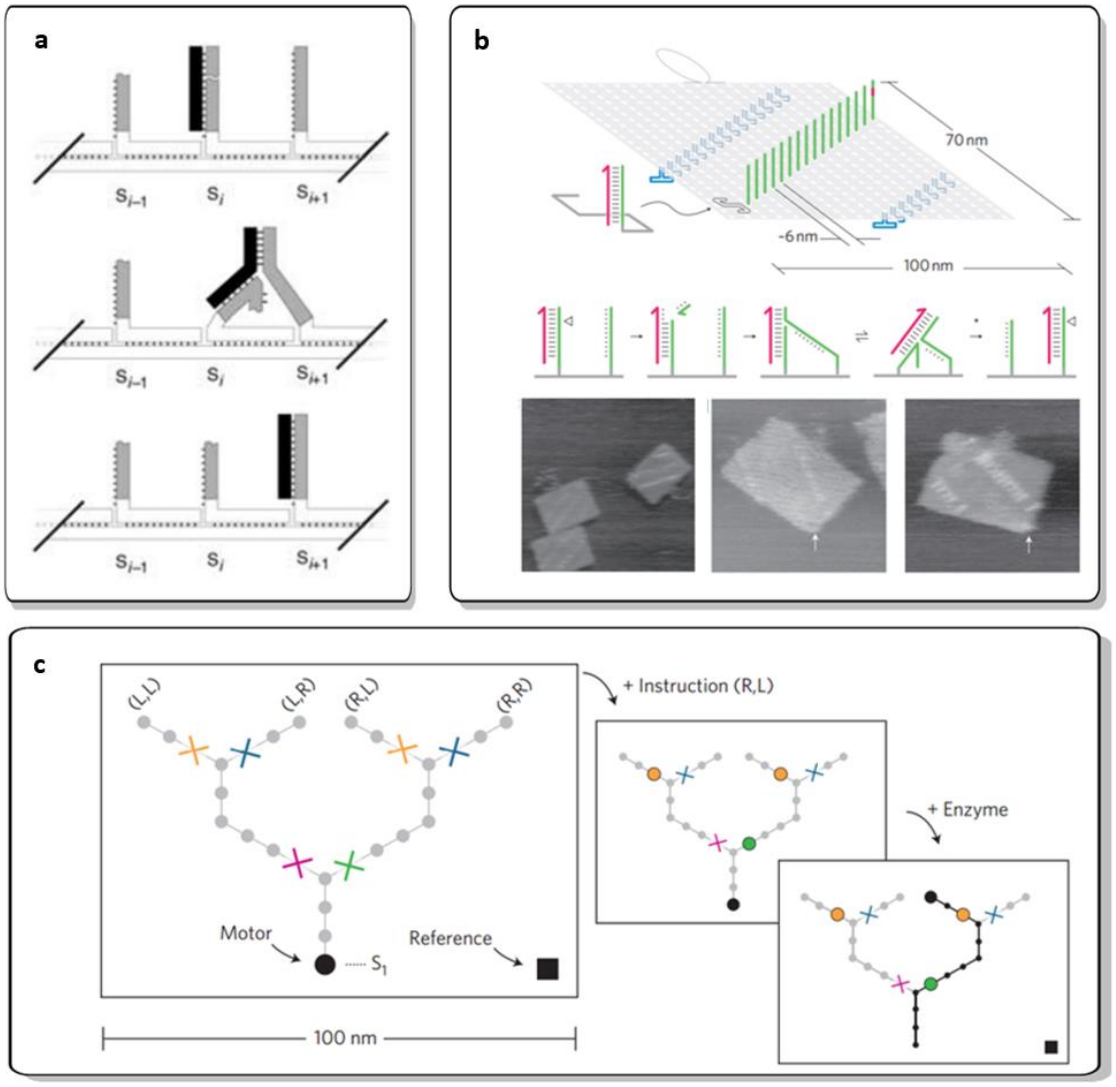

Figure 1.11. (**a**) Stepping mechanism of an endonuclease powered monopod motor. (**b**) Long, linear transport of an endonuclease powered motor transversing a DNA origami patterned track. Realtime AFM was used to directly image the motor translocation along the track. (**c**) Schematic design of a network of tracks templated by DNA origami where the desired path is unblocked through external addition of an unblocking strand or by pre-programming a catalytic domain into the motor body that catalyzes the unblocking strand displacement reaction (blocked sections represented by colored X's). Reprinted from References 34, 38, and 39 with permission from the publisher.

Though DNA-based motors have made great progress since the initial studies carried out by labs of Seeman and Pierce, the motor speed and efficiency need to be greatly

enhanced in order to transition motors into becoming a functional technology. Systematic studies of model systems investigating confined enzyme activity may be the key to addressing this challenge.

1.4 Aim and Scope

As is evident, enzymes are becoming more and more integrated in industrial processes, therapeutics, and sensors; however, we still have a limited understanding of their activity when confined to surfaces. In addition, confined enzymatic reactions have the potential to revolutionize the field of DNA-based motors. Therefore, in this dissertation, I will describe the developments of model systems characterizing enzyme activity when confined to surfaces, with the particular emphasis on the collective properties resulting from multivalent enzyme assemblies. Initially, in **Chapter 2**, I will discuss the activity of DNAzyme 10-23 when immobilized to a gold nanoparticle scaffold. This system was selected for study because of the unique optical and chemical properties of gold nanoparticles and the importance of DNAzyme 10-23 in gene regulation, sensing, and DNA based motors. Results summarizing the role of enzyme valency, enzyme orientation, linker length, linker composition, and passivation on DNAzyme 10-23 activity will be presented. From these findings, highly active DzNPs will be synthesized to study their effectiveness as a gene regulatory agent both *in vitro* (**Chapter 2**) and *in vivo* (**Chapter 3**).

In addition to studying the biological relevance of these particles, we will also explore the physical properties of DNAzyme nanoparticle conjugates when exposed to a substrate that is also polyvalent and immobilized. Due to the initial studies showing limited catalytic activity of immobilized DNAzymes, a more efficient enzyme, RNase H, will be used for these model systems (**Chapter 4**). **Chapter 5** will recap the findings and discuss the

interesting synergistic properties that could emerge by combining these two enzymes onto a single catalytic particle.

1.5 References

(1) Lander, E. S.; Consortium, I. H. G. S.; Linton, L. M.; Birren, B.; Nusbaum, C.; Zody, M. C.; Baldwin, J.; Devon, K.; Dewar, K.; Doyle, M.; FitzHugh, W.; Funke, R.; Gage, D.; Harris, K.; Heaford, A.; Howland, J.; Kann, L.; Lehoczky, J.; LeVine, R.; McEwan, P.; McKernan, K.; Meldrim, J.; Mesirov, J. P.; Miranda, C.; Morris, W.; Naylor, J.; Raymond, C.; Rosetti, M.; Santos, R.; Sheridan, A.; Sougnez, C.; Stange-Thomann, N.; Stojanovic, N.; Subramanian, A.; Wyman, D.; Rogers, J.; Sulston, J.; Ainscough, R.; Beck, S.; Bentley, D.; Burton, J.; Clee, C.; Carter, N.; Coulson, A.; Deadman, R.; Deloukas, P.; Dunham, A.; Dunham, I.; Durbin, R.; French, L.; Grafham, D.; Gregory, S.; Hubbard, T.; Humphray, S.; Hunt, A.; Jones, M.; Lloyd, C.; McMurray, A.; Matthews, L.; Mercer, S.; Milne, S.; Mullikin, J. C.; Mungall, A.; Plumb, R.; Ross, M.; Shownkeen, R.; Sims, S.; Waterston, R. H.; Wilson, R. K.; Hillier, L. W.; McPherson, J. D.; Marra, M. A.; Mardis, E. R.; Fulton, L. A.; Chinwalla, A. T.; Pepin, K. H.; Gish, W. R.; Chissoe, S. L.; Wendl, M. C.; Delehaunty, K. D.; Miner, T. L.; Delehaunty, A.; Kramer, J. B.; Cook, L. L.; Fulton, R. S.; Johnson, D. L.; Minx, P. J.; Clifton, S. W.; Hawkins, T.; Branscomb, E.; Predki, P.; Richardson, P.; Wenning, S.; Slezak, T.; Doggett, N.; Cheng, J. F.; Olsen, A.; Lucas, S.; Elkin, C.; Uberbacher, E. Initial sequencing and analysis of the human genome. *Nature* **2001**, *409*, 860.

(2) Schmid, R. D. Introduction: Immobilized Enzymes: Past, Present and Prospects. *Carrier-Bound Immobilized Enzymes: Principles, Applications and Design* **2005**, 1.

(3) Gray, C. J.; Weissenborn, M. J.; Eyers, C. E.; Flitsch, S. L. Enzymatic reactions on immobilised substrates. *Chem Soc Rev* **2013**, *42*, 6378.

(4) Hanefeld, U.; Gardossi, L.; Magner, E. Understanding enzyme immobilisation. *Chem Soc Rev* **2009**, *38*, 453.

(5) Basso, A.; Braiuca, P.; Cantone, S.; Ebert, C.; Linda, P.; Spizzo, P.; Caimi, P.; Hanefeld, U.; Degrassi, G.; Gardossi, L. In silico analysis of enzyme surface and glycosylation effect as a tool for efficient covalent immobilisation of CalB and PGA on Sepabeads (R). *Adv Synth Catal* **2007**, *349*, 877.

(6) ElSohly, A. F., Matthew. Development of Oxidative Coupling Strategies for Site-Selective Protein Modification. *Accounts Chem Res* **2015**.

(7) Jewett, J. C.; Bertozzi, C. R. Cu-free click cycloaddition reactions in chemical biology. *Chem Soc Rev* **2010**, *39*, 1272.

(8) Chen, Y. X.; Triola, G.; Waldmann, H. Bioorthogonal Chemistry for Site-Specific Labeling and Surface Immobilization of Proteins. *Accounts Chem Res* **2011**, *44*, 762.

(9) Gupta, M. N. Thermostabilization of Proteins. *Biotechnol Appl Bioc* **1991**, *14*, 1.

(10) Blanco, R. M.; Calvete, J. J.; Guisan, J. M. Immobilization-Stabilization of Enzymes - Variables That Control the Intensity of the Trypsin (Amine) Agarose (Aldehyde) Multipoint Attachment. *Enzyme Microb Tech* **1989**, *11*, 353.

(11) Guisan, J. M.; Bastida, A.; Cuesta, C.; Fernandezlafuente, R.; Rosell, C. M. Immobilization Stabilization of Alpha-Chymotrypsin by Covalent Attachment to Aldehyde Agarose Gels. *Biotechnol Bioeng* **1991**, *38*, 1144.

(12) Mateo, C.; Palomo, J. M.; Fernandez-Lorente, G.; Guisan, J. M.; Fernandez-Lafuente, R. Improvement of enzyme activity, stability and selectivity via immobilization techniques. *Enzyme Microb Tech* **2007**, *40*, 1451.

(13) Barnett, L. B.; Bull, H. B. The Optimum Ph of Adsorbed Ribonuclease. *Biochim Biophys Acta* **1959**, *36*, 244.

(14) Goldstei.L. Microenvironmental Effects on Enzyme Catalysis - Kinetic Study of Polyanionic and Polycationic Derivatives of Chymotrypsin. *Biochemistry-Us* **1972**, *11*, 4072.

(15) Adlercreutz, P. Immobilisation and application of lipases in organic media. *Chem Soc Rev* **2013**, *42*, 6406.

(16) Chien, M. P.; Thompson, M. P.; Gianneschi, N. C. DNA-nanoparticle micelles as supramolecular fluorogenic substrates enabling catalytic signal amplification and detection by DNAzyme probes. *Chem Commun* **2011**, *47*, 167.

(17) Zhang, D. H.; Yuwen, L. X.; Peng, L. J. Parameters Affecting the Performance of Immobilized Enzyme. *J Chem-Ny* **2013**.

(18) Kim, D. M.; Umetsu, M.; Takai, K.; Matsuyama, T.; Ishida, N.; Takahashi, H.; Asano, R.; Kumagai, I. Enhancement of Cellulolytic Enzyme Activity by Clustering Cellulose Binding Domains on Nanoscaffolds. *Small* **2011**, *7*, 656.

(19) Zhang, D. H.; Yuwen, L. X.; Li, C.; Li, Y. Q. Effect of poly(vinyl acetate-acrylamide) microspheres properties and steric hindrance on the immobilization of Candida rugosa lipase. *Bioresource Technol* **2012**, *124*, 233.

(20) DiCosimo, R.; McAuliffe, J.; Poulose, A. J.; Bohlmann, G. Industrial use of immobilized enzymes. *Chem Soc Rev* **2013**, *42*, 6437.

(21) Tosa, T.; Mori, T.; Fuse, N.; Chibata, I. Studies on Continuous Enzyme Reactions .V. Kinetics and Industrial Application of Aminoacylase Column for Continuous Optical Resolution of Acyl-Dl-Amino Acids. *Agr Biol Chem Tokyo* **1969**, *33*, 1047.

(22) Yalow, R. S.; Berson, S. A. Immunoassay of Endogenous Plasma Insulin in Man. *J Clin Invest* **1960**, *39*, 1157.

(23) Xiang, Y.; Lu, Y. Using personal glucose meters and functional DNA sensors to quantify a variety of analytical targets. *Nature chemistry* **2011**, *3*, 697.

(24) Su, J.; Xu, J.; Chen, Y.; Xiang, Y.; Yuan, R.; Chai, Y. Q. Personal glucose sensor for point-of-care early cancer diagnosis. *Chem Commun* **2012**, *48*, 6909.

(25) Metzker, M. L. APPLICATIONS OF NEXT-GENERATION SEQUENCING Sequencing technologies - the next generation. *Nat Rev Genet* **2010**, *11*, 31.

(26) Sherman, W. B.; Seeman, N. C. A precisely controlled DNA biped walking device. *Nano Lett* **2004**, *4*, 1203.

(27) Shin, J. S.; Pierce, N. A. A synthetic DNA walker for molecular transport. *Journal of the American Chemical Society* **2004**, *126*, 10834.

(28) Gu, H. Z.; Chao, J.; Xiao, S. J.; Seeman, N. C. A proximity-based programmable DNA nanoscale assembly line. *Nature* **2010**, *465*, 202.

(29) Yin, P.; Choi, H. M. T.; Calvert, C. R.; Pierce, N. A. Programming biomolecular self-assembly pathways. *Nature* **2008**, *451*, 318.

(30) Omabegho, T.; Sha, R.; Seeman, N. C. A Bipedal DNA Brownian Motor with Coordinated Legs. *Science* **2009**, *324*, 67.

(31) Green, S. J.; Bath, J.; Turberfield, A. J. Coordinated Chemomechanical Cycles: A Mechanism for Autonomous Molecular Motion. *Phys Rev Lett* **2008**, *101*.

(32) Yin, P.; Yan, H.; Daniell, X. G.; Turberfield, A. J.; Reif, J. H. A unidirectional DNA walker that moves autonomously along a track. *Angew Chem Int Edit* **2004**, *43*, 4906.

(33) Tian, Y.; He, Y.; Chen, Y.; Yin, P.; Mao, C. D. Molecular devices - A DNAzyme that walks processively and autonomously along a one-dimensional track. *Angew Chem Int Edit* **2005**, *44*, 4355.

(34) Bath, J.; Green, S. J.; Turberfield, A. J. A free-running DNA motor powered by a nicking enzyme. *Angew Chem Int Edit* **2005**, *44*, 4358.

(35) Pei, R.; Taylor, S. K.; Stefanovic, D.; Rudchenko, S.; Mitchell, T. E.; Stojanovic, M. N. Behavior of polycatalytic assemblies in a substrate-displaying matrix. *Journal of the American Chemical Society* **2006**, *128*, 12693.

(36) Lund, K.; Manzo, A. J.; Dabby, N.; Michelotti, N.; Johnson-Buck, A.; Nangreave, J.; Taylor, S.; Pei, R. J.; Stojanovic, M. N.; Walter, N. G.; Winfree, E.; Yan, H. Molecular robots guided by prescriptive landscapes. *Nature* **2010**, *465*, 206.

(37) He, Y.; Liu, D. R. Autonomous multistep organic synthesis in a single isothermal solution mediated by a DNA walker. *Nat Nanotechnol* **2010**, *5*, 778.

(38) Wickham, S. F. J.; Endo, M.; Katsuda, Y.; Hidaka, K.; Bath, J.; Sugiyama, H.; Turberfield, A. J. Direct observation of stepwise movement of a synthetic molecular transporter. *Nat Nanotechnol* **2011**, *6*, 166.

(39) Wickham, S. F. J.; Bath, J.; Katsuda, Y.; Endo, M.; Hidaka, K.; Sugiyama, H.; Turberfield, A. J. A DNA-based molecular motor that can navigate a network of tracks. *Nat Nanotechnol* **2012**, *7*, 169.

(40) Cha, T. G.; Pan, J.; Chen, H. R.; Salgado, J.; Li, X.; Mao, C. D.; Choi, J. H. A synthetic DNA motor that transports nanoparticles along carbon nanotubes. *Nat Nanotechnol* **2014**, *9*, 39.

(41) Mai, J.; Sokolov, I. M.; Blumen, A. Directed particle diffusion under "burnt bridges" conditions. *Phys Rev E* **2001**, *64*.

(42) Silverman, S. K. Deoxyribozymes: Selection Design and Serendipity in the Development of DNA Catalysts. *Accounts Chem Res* **2009**, *42*, 1521.

(43) Zhang, X. B.; Kong, R. M.; Lu, Y. Metal Ion Sensors Based on DNAzymes and Related DNA Molecules. *Annual Review of Analytical Chemistry, Vol 4* **2011**, *4*, 105.

(44) Antal, T.; Krapivsky, P. L. Molecular spiders with memory. *Phys Rev E* **2007**, *76*.

Chapter 2: Nanoparticle Immobilized Deoxyribozymes: Model system for studying enzyme confinement and RNAi-independent gene regulation

2.1 Introduction

Herein, we aimed to investigate deoxyribozymes gold nanoparticle (DzNPs) conjugates as a model to investigate how spatial organization and nanoparticle confinement affect the properties of enzymes. We chose a deoxyribozyme (DNAzyme) as a model enzyme due to its simplistic structure compared to proteins, synthetic accessibility, and ease of modification. DNAzymes are catalytic DNA molecules that are widely used in the areas of bio-computational logic gates and circuits (DNA-computing),[1] programmable materials,[2] ultrasensitive UO_2^{2+} and Pb^{2+} metal-ion detection,[3,4] for understanding gene function and as therapeutics.[5] The most commonly studied DNAzyme is the '10-23' DNAzyme and consists of a 15-base enzymatic core flanked by two arms, and functions as a site- and sequence- specific RNAase.[6] Consequently, the 10-23 DNAzyme has been tested as a therapeutic in animal models due to its ability to block translation of tumorigenic genes.[7-11]

Gene regulation using DNAzymes is very attractive due to the inherent ease and low cost of synthesis, high selectivity, and significant catalytic efficiency.[12] Moreover, DNAzymes will catalytically inhibit translation in a manner that is independent of RNA interference (RNAi), thus circumventing the need for using a short interfering RNA (siRNA) to hijack the RNA-induced silencing complex.[5,7-11] However, modulating gene expression and transitioning this class of functional nucleic acids *in vivo* will not be possible without solving the issues of cellular delivery and intracellular stability.[12,13] A wide range of sophisticated chemical modifications to the DNAzyme backbone, its nucleic bases, and the secondary structure of its 5' and 3' termini increase the intracellular stability of catalytic oligonucleotides to varying degrees, but the challenge of

delivery with minimal toxicity is persistent.[14,15] Therefore, a second motivation for studying the properties of DzNP conjugates was their potential in solving the problem of cellular delivery and intracellular stability.

We synthesized polyvalent DNAzyme-gold nanoparticle (DzNP) conjugates to generate a nanozyme (**Figure 2.1**, **Table 2.1**). A nanozyme is typically defined as a self-assembled multivalent catalytic particle that functions as a single entity and that generally displays enhanced substrate binding, stability, and in some cases, higher activity than the individual catalytic subunits.[16] This concept of multi-enzyme complexes is widely employed in Nature. For example, enzymes are assembled at the lipid membrane or arranged by scaffolding proteins to enhance substrate channeling or alter catalytic activity.[17] Moreover, typically, enzyme confinement onto nanoparticles can greatly enhance enzyme activity.

The DNA-gold nanoparticle conjugate is an attractive platform because the structural conformation of DNA molecules immobilized onto gold nanoparticles has been well characterized and due to the novel properties these assemblies possess.[18-20] DNA-gold nanoparticle conjugates are highly stable and have shown successful intracellular gene regulation through antisense and RNAi mechanisms.[21,22] This is due to their enhanced binding affinities,[23] resistance to nuclease degradation,[24] high cellular uptake,[25] and diminished cellular toxicity[26] when compared to free oligonucleotides. DNA gold nanoparticle conjugates also display highly cooperative hybridization with sharp thermal melting curves when hybridized to complementary DNA gold nanoparticles.[27] Consequently, we rationalized that DzNPs would show superior properties as a gene regulation agent in addition to providing a model platform to explore the fundamental

role of supramolecular organization in tuning the catalytic efficiency of nanozymes. In this chapter, we report the synthesis and characterization of 10-23 DzNPs, show that these nanozyme assemblies are sensitive to DNA density and orientation, and can catalytically regulate intracellular gene expression through site selective cleavage of target messenger RNA (mRNA). Together, this work demonstrates a facile route to design, deploy, and trigger DNAzymes within cells.

Very little is known about the structural conformation of the active catalytic loop of DNAzymes. A crystal structure of an inactive 10-23 DNAzyme-substrate complex was solved and showed a Holliday junction conformation (composed of two DNAzymes and two RNA substrates) with dimensions of 50×40×40Å.[28] Even though the crystal structure of the active 15 base catalytic loop of the 10-23 DNAzyme is not available, this X-ray structure suggests that severe steric crowding may occur within the context of a high density polyvalent DNA nanoparticle conjugate. Therefore, we sought to determine if the steric environment of an RNA-cleaving DzNP would inhibit catalysis. Previous studies by Lu and coworkers used catalytic RNA-cleaving DNAzyme '8-17' to amplify the reporter signal in analytical assays for transition metals.[3,4,29,30] In those systems, the DNAzyme was hybridized to linker strands that bridged the terminal sequences of DNA-

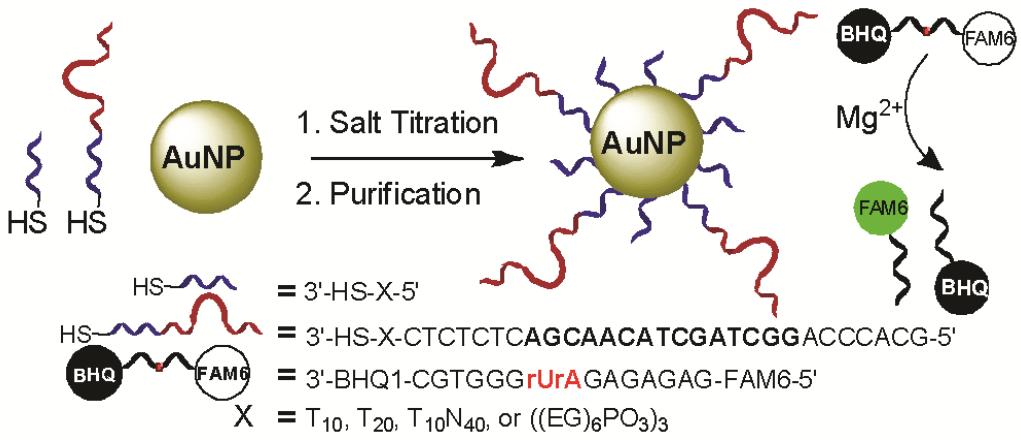

Figure 2.1. A schematic of the strategy used to generate DNAzyme gold nanoparticle conjugates (DzNPs). A binary mixture of two oligonucleotides, DNAzymes and passivating strands, were used to control the steric environment at the particle surface. The catalytic activity of DzNPs was determined by measuring the rate of fluorescence increase, which represents the rate of substrate hydrolysis and de-quenching.

functionalized nanoparticles, and therefore the DNAzymes were separated from the gold core.[3,4,29,30] Recently, 80 nm iron oxide particles functionalized with 1.6 DNAzymes/particle were synthesized for HCV gene regulation; however, it remains unclear how direct DNAzyme conjugation (or general enzyme conjugation) to the NP surface alters catalytic activity.[31, 32, 33]

2.2 Results and Discussion

2.2.1 DzNP synthesis and catalysis

In a typical DzNP synthesis, we reduced 3'thiol-modified oligonucleotides (50 μM), then mixed with gold nanoparticles suspended in phosphate buffered saline (pH 7.4) at a final DNA, and particle concentration of 3 μM, and 6 nM, respectively. The solution was then stabilized with sodium dodecyl sulfate and salted to 0.7 M NaCl over a period of 3 hours with intermittent sonication (**Section 2.3 Materials and Methods**).[34] The oligonucleotide density of the purified $DzT_{10}NPs$, where T_{10} refers to the thiolated poly T spacer linking the DNAzyme to the nanoparticle, was 160 ±10 oligonucleotides/particle based on a fluorescence DNA quantification kit (Invitrogen). To verify particle integrity, TEM and UV-Vis analysis were performed before and after particle functionalization,

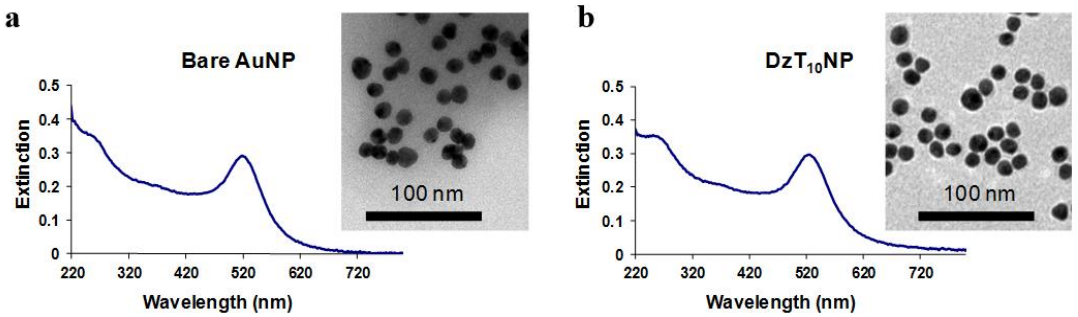

Figure 2.2. Representative UV-vis spectrum and TEM of citrate stabilized gold nanoparticles (**a**) and DzT_{10} modified gold nanoparticles (**b**).

and indicated that the particles remained dispersed following modification with DNAzymes (**Figure 2.2**). The catalytic activity of these particles was determined by measuring the rate of hydrolysis of a diribonucleotide within a DNA substrate that was functionalized with a 5' 6-fluorescein (FAM6) and a 3' black hole quencher^{TM} (BHQ^{TM}) (**Figure 2.1, Table 2.1**). This reaction rate was measured using a temperature-controlled fluorometer and reported as k_{obs} using a fluorescence calibration curve for a 3'FAM6 modified oligonucleotide standard, where k_{obs} is defined as the rate of product formation normalized by the enzyme concentration (min^{-1}), which is equal to the DzNP concentration or the soluble DNAzyme concentration in each experiment. **Figure 2.3a** shows representative reaction kinetics for DzT_{10}NPs and free DzT_{10} (**See Table 2.1 for sequences**) under identical conditions (25 °C, 4.2 nM = [DzT_{10}] and [DzT_{10}NP], 1 μM substrate, 20 mM Tris pH=7.4, 300 mM NaCl, and 50 mM Mg^{2+}). The initial rate of the reaction was determined from the linear slope of the plot (t <80 min). The k_{obs} for soluble DzT_{10} and DzT_{10}NP were 0.017 and 0.134 min^{-1}, respectively. In all our analyses, we chose to compare a DzNP, rather than its individual sub-units, to a single DNAzyme molecule in accordance with past literature.[21,23] This is typical because the nanoparticle

functions as an ensemble entity inside living cells.[21] For comparison, the individual enzyme subunits in DzNPs showed an activity of 0.0025 min^{-1} when assuming a 33% hybridization efficiency.[35] We also found that DzNPs are stable under these conditions, and particles that were used in catalysis reactions for 12 hrs only showed a 20% decrease in activity when they were re-used the following day (**Figure 2.3b**). Importantly, this data confirms that the DzNPs are robust and retain catalytic activity despite the dense oligonucleotide environment on the nanoparticle.

2.2.2 Role of surface density and linker chemistry on catalysis

To systematically study the effect of surface packing density and steric crowding on the rate of catalysis, a series of DzNPs were synthesized using a binary mixture of two oligonucleotides that included a T_{10} passivating sequence along with the DzT_{10}. In this series, the total ssDNA concentration was kept constant while adjusting the molar concentrations of 3'thiol modified DzT_{10} and T_{10}. Because both oligonucleotides have the same T_{10} spacer, the DNA composition of gold nanoparticles was expected to reflect that of the bulk solution.[35] The goal was to tune the average spacing between adjacent

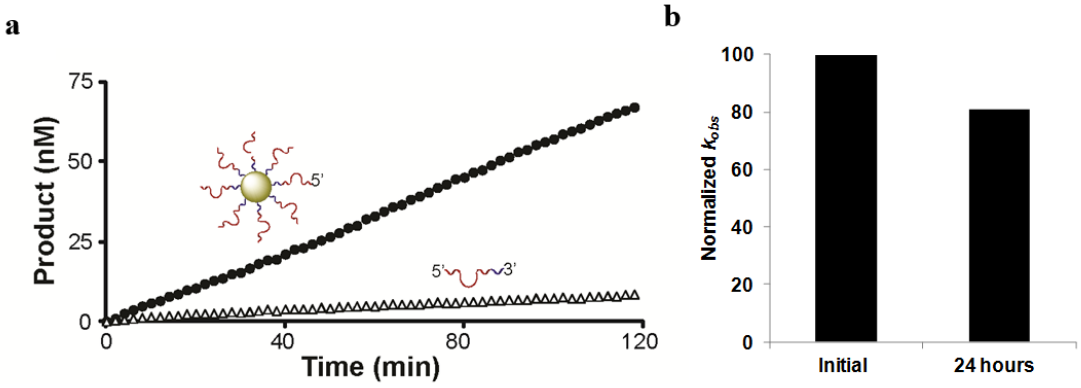

Figure 2.3. (**a**) A representative kinetic plot showing the rate of catalysis for 4.2 nM $DzT_{10}NP$ ([AuNP]=4.2nM) (closed circles) and DzT_{10} (triangles) enzymes ([Mg^{2+}]= 50 mM). (**b**) A bar graph showing the initial and final catalytic activity of $Dz((EG_6)PO_3)_3NP$ after incubation at 25

°C for 24 hrs during a catalytic run. At t = 24 hrs, the nanoparticles were isolated and used in another reaction with new substrate in reaction buffer (20 mM Tris pH 7.4, 300 mM NaCl, and 10 mM $MgCl_2$) and the initial rate constant of the reaction was reported.

DNAzymes and consequently tune steric crowding. The total number of DNA molecules per particle was measured using a commercial fluorescence assay (**Figure 2.4a**).[35] To further verify these measurements, DNA was released from the particle surface using dithiothreitol (DTT) and the DNAzyme concentration was determined by using the observed rate constant of substrate hydrolysis as compared to a calibration standard of soluble DNAzyme (**Figure 2.4a**). **Figure 2.4b** shows a plot of the initial rate constant of DzNPs with a range of enzyme packing densities compared to soluble DNAzyme under standard reaction conditions (25 °C, 4.2 nM = [$DzT_{10}NP$], 1 μM substrate, 20 mM Tris pH=7.4, 300 mM NaCl, and 10 mM Mg^{2+}). For direct molecule to molecule comparison, see **Figure 2.4c**. We found that at lower enzyme packing densities (15-60 enzymes/particle) the activity of each particle shows a linear increase as a function of the number of DNAzymes per particle. However, particles with packing densities exceeding 60 DNAzymes per particle show saturation in activity. This trend suggests that steric packing limits the maximum activity of each DzNP assembly. As a corollary, this limit in maximum activity equates to each catalytic oligonucleotide requiring a footprint that is at least ~11 nm^2 on the particle surface in order to achieve its maximum activity under these conditions.

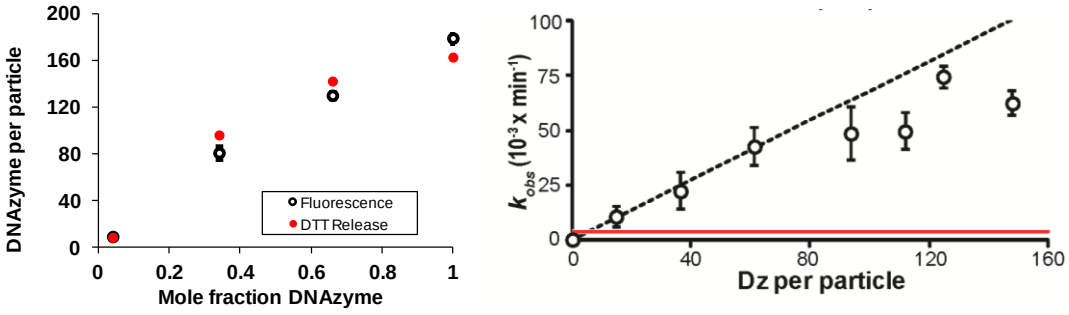

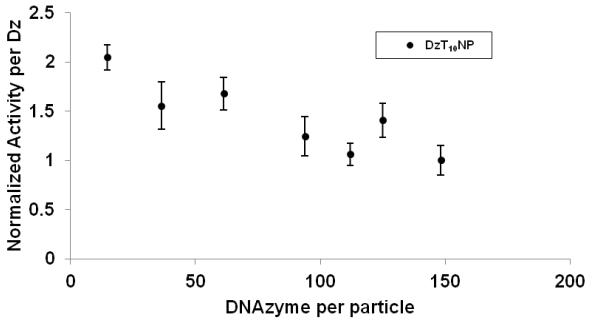

Figure 2.4. (**a**) A plot showing the DNAzyme surface density as determined by two independent methods. The first method is based on an oligonucleotide fluorescence quantification kit (open circles). The second approach measures the catalytic activity of DTT-released DNAzyme and the concentration was quantified using a standard calibration curve (red circles). Error bars represents the standard deviation of three measurements. (**b**) A plot showing k_{obs} for the hydrolysis of a series of DzNPs that vary in DNAzyme surface density at $[Mg^{2+}]$= 10 mM. The horizontal red line denotes the activity of free DzT_{10} (4.2 nM). The diagonal dashed line is a best fit (R^2=0.99) through the lower density DzNP data points (≤ 60 DNAzymes/particle). All error bars represent the standard deviation of three measurements. (**c**) Catalytic activity per DNAzyme of a series of DzT_{10}NPs that vary in DNAzyme surface density. The k_{obs} values were normalized to the activity of Dz from the non-passivated, fully packed particle (4.2×10^{-4} mol min^{-1} Dz^{-1}). Error bars are the standard deviation of three measurements.

Given that the hybridization efficiency and gene regulation efficacy have been shown to be dependent on the chemical nature of the group anchoring an oligonucleotide to a gold nanoparticle, we decided to next investigate the catalytic properties of DzNPs modified with the following poly T and ethylene glycol phosphate linkers: T_{10}, T_{20}, $T_{10}N_{40}$, and $((EG)_6PO_3)_3$ (**Table 2.1**). The measured oligonucleotide density of fully packed particles was 148 ±10, 137 ±10, 80 ±1, and 195 ±2 oligonucleotides/particle for the T_{10}, T_{20}, $T_{10}N_{40}$, and $((EG)_6PO_3)_3$ linkers, respectively. The differences in packing densities were hypothesized to be due to a combination of steric crowding and interaction of the linker nucleobases with the gold surface. Given these DNA densities, we expected that longer linkers would generate DzNPs with increased catalytic efficiency, as this

difference would be due to reduced steric inhibition for longer linkers. Surprisingly, no clear trend was observed between k_{obs} and increasing linker length (**Figure 2.5**). In fact, $DzT_{10}N_{40}NP$ (0.032 min^{-1}) had a decrease in activity when compared to $DzT_{10}NP$ (0.062 min^{-1}) and $DzT_{20}NP$ (0.062 min^{-1}), which had identical activities (**Figure 2.5**). The ethylene glycol phosphate $((EG)_6PO_3)_3$ linker generated the most densely packed particles (~195 Dz molecules/particle), and when these particles were compared to $DzT_{10}NP$ and $DzT_{20}NP$, they showed a 56% increase in k_{obs} (**Figure 2.5**). Since polyethylene glycol linkers are known to minimize non-specific adsorption on surfaces,[36],[34] the results suggest that chemisorption of DNAzyme active site nucleobases to the gold surface alters catalytic activity, and may play a more significant role in tuning the catalytic activity of DzNPs.

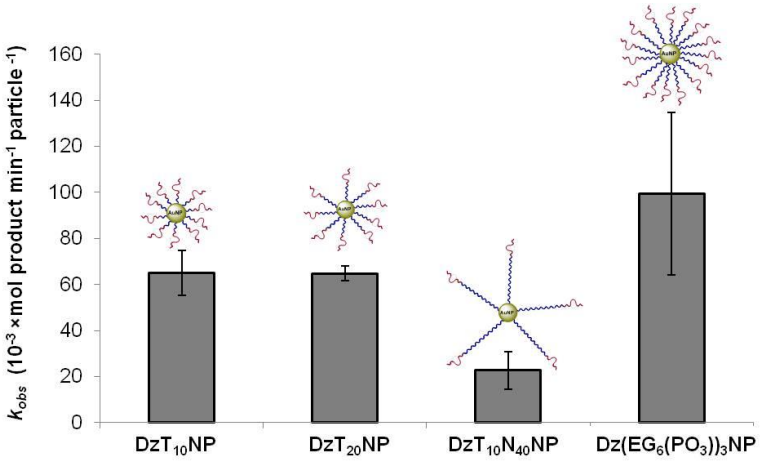

I.D.	#DNA/NP
$DzT_{10}NP$	148±10
$DzT_{20}NP$	137±10
$DzT_{10}N_{40}NP$	80±1
$Dz(EG_6(PO_3))_3$	195±2

Figure 2.5. A bar graph summarizing the catalytic activity of DzNPs synthesized using a variety of different linkers with schematic representations of the fully packed DzNPs showing DNAzyme (red) density and linker (blue) length. The k_{obs} values were calculated by measuring the linear slope of the initial rate of reaction from the kinetic plot (T<80 min.) ([$MgCl_2$]=10mM). Error bars are the standard deviation of three measurements. The table summarizes the corresponding DNA densities.

2.2.3 Role of DNAzyme orientation on catalytic activity for DzNP

The role of non-specific interactions in DzNP catalytic activity was verified when we measured the rate of substrate hydrolysis using gold nanoparticles functionalized with

DNAzymes anchored through a 5' thiol ($Dz_{rev}T_{10}$) rather than the 3' terminus anchor. The DNA density on these particles was 180 ±10 oligonucleotides/particle, but we found that their activity was nearly abolished (**Figure 2.6a, circles**). When $Dz_{rev}T_{10}$NPs were treated with DTT in order to release the surface-bound DNA, the free DzT_{10} fully recovered its activity, thus displaying a 3200% increase in catalytic activity (**Figure 2.6a, triangles**). The drastic difference in activity between DzT_{10}NP and $Dz_{rev}T_{10}$NP (900% difference) (**Figure 2.6b, compare circles**) suggests that the catalytic core is asymmetric in its sensitivity to the supporting gold nanoparticle surface.[37] Importantly, $Dz_{rev}T_{10}$NPs remained inactive even when their packing densities were reduced to 90 Dz/NP (~50% packed) either with or without T_{10} passivation (**Figure 2.6b, triangles**). Furthermore, when these particles are treated with mercaptoethanol, the DNAzyme surface density is decreased, but again, the activity of the $Dz_{rev}T_{10}$NPs remained suppressed (**Figure 2.6c,d**). Together, these observations agree with systematic mutagenesis analysis studies on the 10-23 DNAzyme catalytic domain that have shown a high degree of sensitivity at many bases near the 5' terminus of the active site.[38] Therefore, DNAzyme orientation needs to be carefully examined in DzNP design, which should be a general consideration that is broadly relevant to other biological nanozymes.

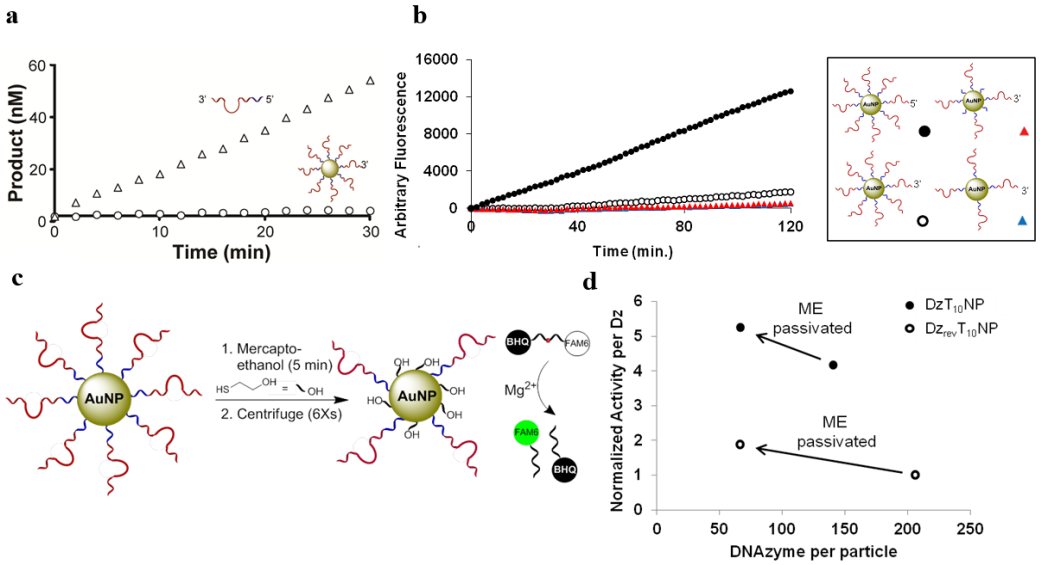

Figure 2.6. (**a**) A kinetic plot showing rate of catalysis of $Dz_{rev}T_{10}NP$ (open circles) and DTT displaced $Dz_{rev}T_{10}$ (open triangles) from the particle. (**b**) Catalysis of fully packed and 50% packed $Dz_{rev}T_{10}NP$. A kinetic plot showing the rate of hydrolysis of a quenched substrate for fully packed $Dz_{rev}T_{10}$ NP (open circles) and 50% packed (T_{10} passivated: closed red triangles and non-passivated: closed blue triangles) $Dz_{rev}T_{10}NP$. The data indicates that the reduction in steric crowding does not restore $Dz_{rev}T_{10}NP$'s activity to the level of $DzT_{10}NP$ (closed black circles). (**c**) Activity of mercaptoethanol (ME) passivated DzNPs. (**d**) A schematic showing the use of ME passivation of DzNP to reduce Dz-Au interactions. The catalytic activity of the passivated particles was determined by measuring the rate of fluorescence increase, which represents the rate of substrate hydrolysis and de-quenching.

2.2.4 Photo-thermal activation of DNAzymes

Photodynamic control of gene regulation agents, such as DNAzymes, is a highly desirable property, and various synthetic strategies have been employed to demonstrate this capability.[39-41] Because the gold nanoparticle was found to significantly inhibit the DNAzyme anchored through its 5' terminus, we thought that photo-induced DNA release would be a suitable proof-of-concept to demonstrate a triggered catalytic function (**Figure 2.7a**). We released $Dz_{rev}T_{10}$ from the particle by irradiation with a 532 nm pulsed laser, which is known to selectively cleave the thiol-gold bond at certain laser powers (**Figure 2.7b**).[42] Importantly, this strategy offers significant advantages because it is

synthetically facile and compatible with 2-photon and visible irradiation, in contrast to the recently developed azo-benzene and caged-nucleotide based approaches that require excitation at UV wavelengths.[43,44]

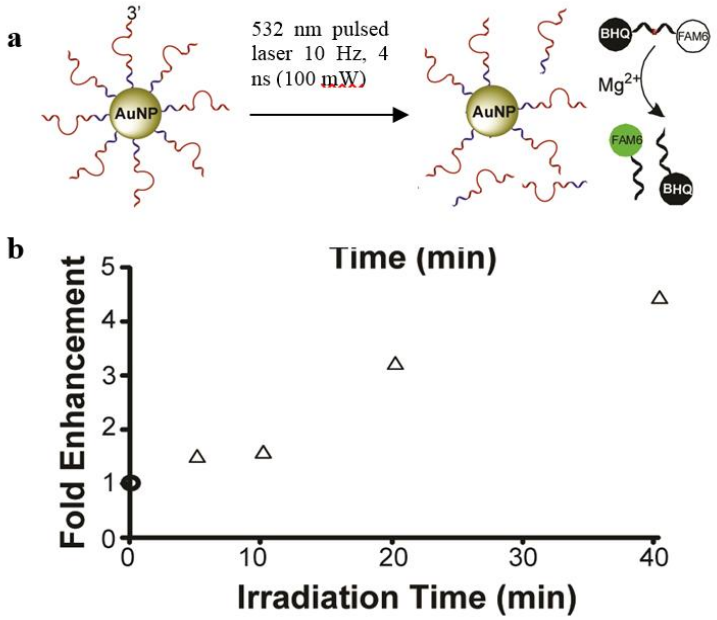

Figure 2.7. (**a**) Schematic showing laser irradiation (top) to release $Dz_{rev}T_{10}$ from the particle to enhance catalysis. (**b**) A plot showing k_{obs} as a function of irradiation time where the rate constant was normalized to particle at t = 0 min (open circle). Nd:YAG laser was operated at 10 Hz, 4 ns pulse width, generating 125 mW/cm^2 power.

2.2.5 DzNP cellular uptake and resulting gene regulation

Having shown that properly designed DzNPs are catalytically active in buffer conditions, we next set out to investigate their activity under conditions that mimic the cellular environment by exposing the particles to nucleases and serum. To test DzNP resistance towards nucleases, the catalytic activity of free DzT_{10} and DzT_{10}NP was measured before and after incubation with a model nuclease, DNase I. **Figure 2.8a** shows that after DNase I treatment (120 min), the soluble enzyme retained only 10% of its original activity, while the DzNPs retained 90% of its original activity. This result is in

agreement with previous reports showing that polyvalent DNA modified gold nanoparticles shield oligonucleotides from hydrolytic cleavage by DNases.[24] We also tested the activity of DzNPs that are exposed to 10% fetal bovine serum for 24 hrs, and found the particles to remain active (**Figure 2.8b**).

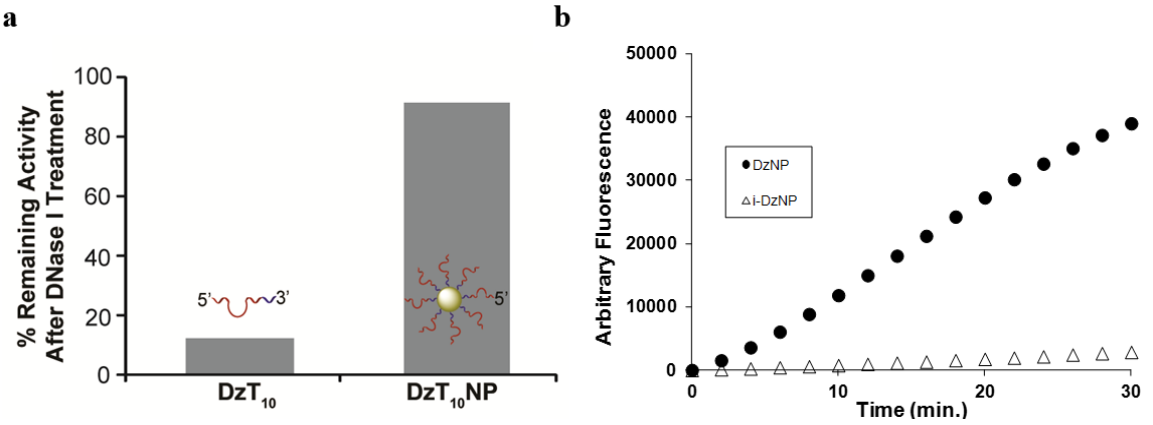

Figure 2.8. (**a**) Bar graph showing the relative catalytic activity of DzT_{10} and $DzT_{10}NP$ after exposure to DNase I for 120 min at 37 °C. (**b**) A kinetic plot showing the rate of hydrolysis of a quenched substrate substrate for active (DzNP) and inactive (i-DzNP) DzNPs. Both particles were treated with cell culture media (DMEM) supplemented with 10% fetal bovine serum (FBS) for 24 hours at a particle concentration of 1.25 nM and a total volume of 500 µL. After 24 hours, the particles were centrifuged down and media was discarded and reaction buffer added, thus bringing the final particle concentration to 4.2 nM and standard reaction conditions (1 µM substrate, 20 mM Tris pH 7.4, 300 mM NaCl, and 10 mM $MgCl_2$). The slight background rate observed for the in-active DzNPs is the result of residual RNase that is typically found in serum.

To determine whether DzNPs enter mammalian cells and catalytically regulate gene expression, we designed DzNPs with recognition arms specific towards the TGF-β related growth differentiation factor 15 (GDF15) mRNA sequence ($Dz_{GDF15}NP$, **Table 2.1**).[45] GDF15 was selected as a proof-of-concept due to its clinical association with disease progression and resistance to chemotherapy in breast, prostate, ovarian, and colorectal cancer, and its knockdown has been shown to inhibit proliferation.[46-48] Moreover, GDF15 is found to contribute, in part, to the development of resistance to the anti-HER2 therapeutic trastuzumab (Herceptin, Genetech, Inc.).[49] HER2 is overexpressed

in approximately 20-30% of metastatic breast cancers, and trastuzumab is the first line of treatment for this subset of tumors. Acquired resistance to trastuzumab will typically develop in patients within one year of therapy.[50] Moreover, viral vector-based knockdown of GDF15 has been shown to rescue some of the sensitivity to trastuzumab in breast cancer cell line models that acquire resistance.[49] These results provide the therapeutic rationale for targeting GDF15.

The GDF15 specific DNAzyme included two 2'-O-methyl RNA bases that were incorporated within both the 5' and 3' termini, which is a common modification to reduce nuclease degradation in cell studies.[21] To distinguish between antisense and DNAzyme-catalyzed hydrolysis mechanisms, we introduced a single base mutation in the DNAzyme catalytic core (G1 to A1) to generate catalytically inactive nanoparticles (i-Dz_{GDF15}NP, **Table 2.1**).[6,38] Negative control particles (Dz_{NC}NP) were also synthesized and their DNA sequences included two randomized N8 arms flanking the 15-mer catalytic loop to control for off-target effects (**Table 2.1**). The oligonucleotide density was quantified in these three types of particles and found to be 200 ±10, 230 ±40, and 111 ±10 DNAzymes per particle for i-Dz_{GDF15}NP, Dz_{GDF15}NP, and Dz_{NC}NP, respectively. After confirming that DzNPs readily enter mammalian cells (**Figure 2.9a**), HCC1954 HER2-over-expressing breast cancer cells were treated with 5 nM of particles for 48 hrs, and then analyzed using real-time PCR to quantify GDF15 mRNA expression levels relative to the house keeping gene RPLPO (component of the 60S ribosomal subunit). The dosage of 5 nM particles was selected since the 20 nM dose showed some toxicity under these conditions (results not shown). The average GDF15 expression levels relative to RPLPO are shown in **Figure 2.9b** and are reported as relative GDF15 copy number ($2^{\Delta C_t}$). The

error represents the standard error of the mean (SEM), and was calculated from three independent experiments, where each experiment generally consisted of three wells and the PCR expression level within each well was measured three times. ANOVA statistical analysis was performed on the data and indicates that the enzymatic nanoparticles, Dz_{GDF15}NP, reduce GDF15 expression by ~57% relative to negative control particles with a *p* value less than 0.005, whereas i-Dz_{GDF}NPs showed an average of ~4% knockdown, similar to reported literature values for antisense oligonucleotides gold nanoparticles,[21] but was within experimental error of Dz_{NC}NPs. Since both types of DNA-modified nanoparticles are complementary to the GDF15 mRNA, they are expected to reduce GDF15 expression levels through a common antisense mechanism, and the difference in the activity between active and inactive nanoparticles can be attributed to the contributions of the catalytic oligonucleotides. Optimized lentiviral shRNA-based knockdown of GDF15 in this cell lines has been reported to display a ~50% reduction in GDF15 expression as measured by PCR,[49] which is comparable to the efficacy of 5 nM Dz_{GDF15}NPs.

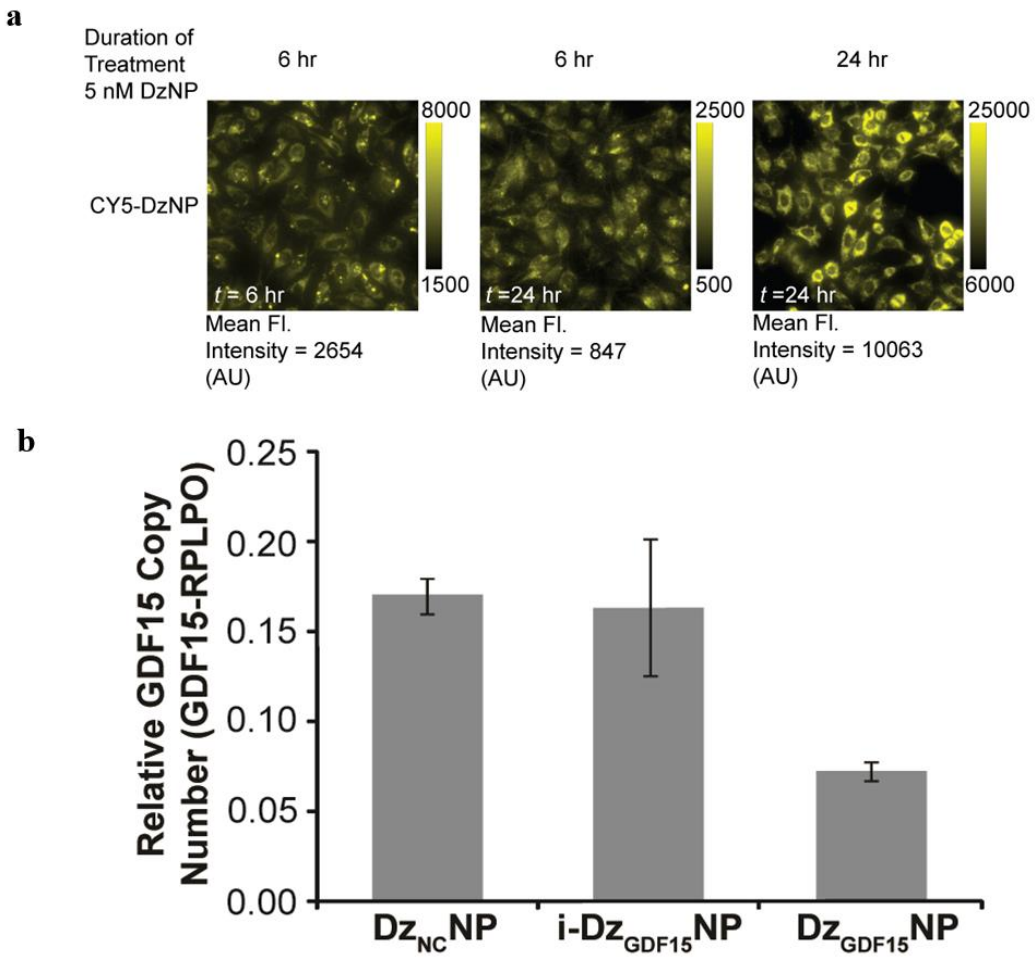

Figure 2.9. (**a**) Qualitative observation of DzNP cellular entry. Fluorescent images of HeLa cells treated with 5 nM DzNPs that were hybridized to a complementary oligonucleotide conjugated to a Cy5 fluorescent probe. Fluorescence images were collected at 6 and 24 hour time points. One sample was treated with DzNPs for 6 hrs while the second sample was treated for a 24 hr duration. The fluorescence image at the earlier time point (t = 6 hr) shows punctuate signal within the cytoplasm of cells. Cells that were imaged at the 24 hr time point show more uniform and less punctate fluorescence intensity within the cytoplasm. In addition, the cells continually take up DzNPs and cells that were treated for 24 hrs show one order of magnitude larger fluorescence intensity when compared to cells that were only treated with DzNPs for 6 hrs. (**b**) Real-time PCR analysis of GDF15 mRNA expression of HCC1954 cells, which were treated with catalytic ($Dz_{GDF15}NP$) and non-catalytic (i-$Dz_{GDF15}NP$) DzNPs targeting GDF15 mRNA and nonspecific catalytic ($Dz_{NC}NP$) DzNPs at a concentration of 5 nM for 48hrs. The catalytic particles down regulated GDF15 mRNA 57% relative to nonspecific particles (p<0.005) and 53% relative to non-catalytic particles (p=0.015).

2.3 Conclusions

We generated DNAzyme '10-23' NPs and determined some of the design parameters that control catalysis, such as loading density, linker length, linker composition, and DNAzyme orientation. These rules will guide the design of enzymatic DNA-nanomaterials, thus providing a new direction in the growing field of DNAzyme-based therapeutics as new catalytic oligonucleotides are discovered. We demonstrate that DzNPs can knockdown GDF15 expression through a catalytic mechanism of action within cells in an RNA interference-independent pathway. Given that DNAzyme function is complementary to that of siRNA-based gene regulation, there is potential in a dual DzNP and siRNA-NP strategy and especially if one intends to target genes that regulate RISC function. The ability to incorporate DNAzyme-based computing, metal ion and small molecule sensing inside a cell will provide new opportunities in synthetic biology.

2.4 Materials and Methods

2.4.1 DNA sequences

ID	Sequence (5'-3')
$Dz T_{10}$ (Free)	GCACCCAGGCTAGCTACAACGACTCTCTCT$_{10}$
$Dz T_{10}$	GCACCCAGGCTAGCTACAACGACTCTCTCT$_{10}$(CH$_2$)$_3$SH
$Dz_{rev} T_{10}$	HS(CH$_2$)$_6$T$_{10}$GCACCCAGGCTAGCTACAACGACTCTCTC
$Dz T_{20}$	GCACCCAGGCTAGCTACAACGACTCTCTCT$_{20}$(CH$_2$)$_3$SH
$Dz T_{10} N_{40}$	GCACCCAGGCTAGCTACAACGACTCTCTCN$_{40}$T$_{10}$(CH$_2$)$_3$SH
$Dz((EG)_6PO_3)_3$	GCACCCAGGCTAGCTACAACGACTCTCTC((EG)$_6$PO$_3$)$_3$(CH$_2$)$_3$SH
T_{10}	T$_{10}$(CH$_2$)$_3$SH
Substrate	6FAM-GAGAGAGrArUGGGTGC-BHQ
Calibration Probe	GAGAGAGAUGGGTGC-6FAM
Dz_{GDF15}	mGmAGTGCAAGGCTAGCTACAACGATCTGAGGGT$_8$mUmU(CH$_2$)$_3$SH
i-Dz_{GDF15}	mGmAGTGCAA**A**GCTAGCTACAACGATCTGAGGGT$_8$mUmU(CH$_2$)$_3$SH
Dz_{NC}	mNmNNNNNNNGGCTAGCTACAACGANNNNNNNNT$_8$mUmU(CH$_2$)$_3$SH

r=ribonucleotide, 6FAM=6-carboxyfluorescein, BHQ=Black Hole Quencher™, m=2'-O-methyl RNA base, red=catalytic core, **underlined and bold**= inactive point mutation

Table 2.1. List of oligonucleotide sequences.

2.4.2 Synthesis of gold nanoparticles

Citrate-stabilized gold nanoparticles (14 ±1.6 nm) were prepared using published procedures.[51] A 500 mL solution of 1 mM hydrogen tetrachloroaurate (III) trihydrate solution was brought to a vigorous boil, and once boiling, 50 mL of a 38.8 mM sodium citrate tribasic dihydrate solution was added and allowed to reflux for 15 minutes. The reaction mixture was filtered using a 0.45 μm acetate filter, producing monodisperse AuNPs. The resonance wavelength of the gold nanoparticles was determined using UV-vis spectrometry and particle size was determined using transmission electron microscopy (TEM).

2.4.3 Preparation of DzNPs

Disulfide-modified oligonucleotides at either the 5' or 3' end were purchased from Integrated DNA Technologies (IDT). The disulfide was reduced to a free thiol by incubating 35 nmols of lyophilized oligonucleotide with 700 μL of disulfide cleavage buffer (0.1 M dithiothreitol (DTT), 170 mM phosphate buffer at pH = 8.0) for 3 hours at room temperature. The reduced oligonucleotides were purified using a NAP^{TM}-25 column (GE Healthcare, Piscataway, NJ) with Nanopure water as the eluent. Subsequently, 30 nmols of DNA were added to 7.5 mL of 14 nm gold nanoparticles (10 nM) bringing the final concentration of oligonucleotide, and gold nanoparticles to ~3.2 μM, and ~7.3 nM, respectively. The pH of the solution was adjusted to pH = 7.4 by adding 93.8 μL of 100 mM phosphate buffer, thus bringing the phosphate buffer concentration to 9 mM. The particles were stabilized by adding sodium dodecyl sulfate (SDS) to the solution and bringing its final concentration to 0.1% (g/ml) by using a stock solution of 10% SDS. The particles were successively salted with eight NaCl additions

that were spaced 20 minutes apart using a stock solution of 2.0 M NaCl and 10 mM phosphate buffer. The final NaCl concentration of the DNA-AuNP solution was increased to 0.7 M. The first two NaCl additions increased the concentration by 0.05 M increments while the remaining six NaCl additions increased the NaCl concentration by 0.1 M increments. The particles were immediately sonicated for 10 seconds after each salt addition to maximize DNA packing, as indicated in literature protocols.[34] The fully salted particles were then incubated overnight, in the dark and at room temperature. We found that the 10-23 active catalytic core of the DNAzyme had a tendency to drive the formation of nanoparticle aggregates at 0.7 M NaCl due to partial self-complementarity of sequences. The formation of these aggregates did not result in any observable reduction in the quality of the particles (as measured by UV-vis, TEM, catalysis, DNA density). The following day, the particles were centrifuged four times, reconstituted in Nanopure water each time, and stored at 4 °C for future use for a maximum duration of 1 month.

2.4.4 TEM imaging of DzNPs

Transmission electron microscopy (TEM) samples were prepared by pipetting an 8 nM gold nanoparticle solution onto a TEM grid. TEM was conducted on a JEOL JEM-1210 transmission electron microscope. The mean nanoparticle diameter was used to obtain the extinction coefficient, and particle concentrations were subsequently determined using a NanoDrop 2000C spectrophotometer.

2.4.5 Calculation of the number of deoxyribozyme molecules per AuNP

The commercial Quant-iT™ OliGreen® ssDNA kit or measuring the rate of hydrolysis of a quenched substrate by released DNAzyme was used to determine the total

DNA or DNAzyme density per particle. Both methods yield comparable oligonucleotide concentration values. The Quant-iT™ OliGreen® ssDNA kit required preparing a calibration curve by diluting a DNA stock solution (4 μg/mL) composed of the same thiolated oligonucleotides there were used during particle functionalization to 0.1, 0.2, 0.5, 0.75, 1, and 2 μg/mL and a final volume of 100 μL in TE buffer. DzNP solutions were prepared by diluting an 8 nM stock solution to 0.4, 0.6, and 0.8 nM with TE buffer. The Dz oligonucleotides were released from the particle through oxidizing/dissolving the gold with potassium cyanide (KCN) by adding 1 μL of a 5 M stock solution of KCN to each well, including the calibration wells to be consistent. The solutions were incubated with KCN for 30 minutes to ensure complete dissolution. After complete dissolution of the gold nanoparticles, 100 μL of the freshly prepared 1X Quant-iT™ OliGreen® solution was added to each well and fluorescence intensities (485/528 nm excitation/emission) of each well were then measured using a Bio-Tek Synergy HT plate reader to determine the total DNA density. The DNAzyme density was calculated assuming the DNA ratio on the particle was the same as that in solution during the functionalization process. To confirm the oligonucleotide density per AuNP values that were measured using the Quant-iT assay, DNAzyme concentrations were determined by using the observed rate constant of substrate hydrolysis as compared to a calibration standard of soluble DNAzyme. Oligonucleotides were released from the particle surface by incubating 1 nM DzNP solutions with 100 mM dithiothreitol (DTT) for 5 hours. After incubation, catalysis buffer was added (20 mM Tris pH 7.4, 300 mM NaCl, and 10 mM $MgCl_2$) along with 1 μM substrate, and initial rates of catalysis were measured (as described

below). The initial rates were compared to a calibration curve of free DNAzyme activity that was measured under identical reaction conditions.

2.4.6 Measurement of DzNP activity

DNAzyme catalytic activity was determined by measuring the fluorescence intensity as a function of time, which indicated the rate of hydrolysis of a DNA/RNA chimera substrate that was functionalized with a 5' 6-fluorescein (FAM6) and a 3' Black Hole Quencher™ (BHQ). Fluorescence was measured using a temperature-controlled Bio-Tek Synergy HT plate reader. All experiments were conducted under the same reaction conditions unless otherwise stated: 25 °C, 4.2 nM Dz or DzNP, 1 μM substrate, 20 mM Tris pH 7.4, 300 mM NaCl, and 10 mM $MgCl_2$). The rate constant of product formation was quantified in units of mol min^{-1} by using a fluorescence calibration curve for a 3'FAM6 modified oligonucleotide standard (Calibration Probe, **Table 2.1**). The initial rate of the reaction was determined from the initial slope of the plot (t <80 min). During catalysis, it was observed that only in the presence of both substrate and 10 mM Mg^{2+}, DzNPs formed aggregates that settled to the bottom of the reaction vessel. We believe that this is due to a non-cross-linking DNA hybridization aggregation phenomenon, which was reported previously.[52] To verify that these aggregates are the catalytic entity responsible for catalysis, the reaction solution was exchanged and catalysis was subsequently measured. Very little change in rates were observed, indicating that DNAzyme gold nanoparticle conjugates remain anchored to the gold nanoparticle surface (**Figure 2.3b**).

2.4.7 Determination of nuclease resistance

DNase I was acquired from New England BioLabs, Inc. and used as indicated by the manufacturer. DNase I was incubated with 1.9 μM DzT_{10} and 10.4 nM $DzT_{10}NP$ (DzT_{10}=1.9 μM) at a DNase I concentration of 2.5 units/mL in 1 X DNase I reaction buffer (10 mM Tris-HCl, pH =7.6, 2.5 mM $MgCl_2$, and 0.5 mM $CaCl_2$) with a final volume of 40 μL at 37°C for 2 hours. Afterwards, DNase I was inactivated by heating to 75°C for 10 minutes. Tris (pH 7.4), NaCl, substrate, and $MgCl_2$ were then added, thus bringing the total volume to 150 μL and replicating the standard reaction conditions (except [DzT_{10}] = 500 nM). Retention of activity was measured by normalizing the enzymatic activity to the DNAzyme activities prior to addition of DNase I under identical conditions.

2.4.8 Cell culture and DzNP mediated gene knockdown

HCC1954 (CRL 2338) cells were obtained from ATCC and were maintained in RPMI supplemented with 10% FBS and 1% penicillin-streptomycin in standard culture conditions (37 °C, 5% CO_2). Cells were seeded in a 12 well plate at a concentration of 30,000 cells/well and were allowed to adhere overnight under standard cell culture conditions. Nanoparticles were sterilized by filtering through a 0.2 μm filter prior to addition to the cell media. To achieve the desired nanoparticle concentration, the filtered particles were centrifuged at high speed (13,200 rpm) for 40 min and then resuspended in a known volume of complete RPMI medium. 5 nM Dz-gold nanoparticle solution was allowed to incubate with the cells for 48 hrs. The medium containing particles was subsequently removed and the cells were gently washed with PBS. This procedure was repeated twice to remove any potential remaining residual traces of nanoparticles. Total

RNA was then isolated using an RNA isolation kit (Sigma, Cat. # RTN-70) and used following the manufacturer's instructions. A total of 48 ng of RNA was used to synthesize cDNA using the the Qiagen Sensiscript cDNA synthesis kit (Cat #205213). Real-time PCR was performed using Taqman gene expression primers for GDF15 (Cat. # Hs00171132_m1) and housekeeping gene, RPLPO (Cat. # 433761-1006022) from Applied Biosystems. The data was analyzed using the ΔC_T method and reported as such.

2.4.9 Chemical activation of DNAzyme catalytic activity (thiol displacement)

A 1 M stock solution of DTT was freshly prepared for each experiment prior to DTT release of DNAzymes from the AuNP. DzNPs were diluted in a 96 well plate to 4.7 nM in reaction buffer (not including substrate). DTT was subsequently added bringing the final DTT concentration to 100 mM. The particles were incubated in this solution for 12 hours. The substrate was added the following day in order to initiate catalysis. Note that the final DzNP concentration was 4.2 nM which matched the standard catalysis conditions described above.

2.4.10 Photo-thermal activation of DNAzymes

A 100 µL aliquot of DzNPs at a 2 nM concentration was added to a glass bottom 96 well SensoPlate^{TM} (Greiner Bio-One) (O.D. = 0.32). The samples were then irradiated by frequency doubled Q-switched Nd:YAG laser (Spectra-Physics) operating at 532 nm with a pulse width of 10 ns and a repetition rate of 10 Hz for 0, 5, 10, 20, and 40 minutes (*See image and schematic below*). The power density was determined using a power meter (Melles Griot) by measuring the power of the un-attenuated beam, then attenuating the beam to 50% power using an iris where the beam diameter is approximately equal to the diameter of the iris at half maximum power. This power density was determined to be

125 mW / cm^2. The optical density of the samples was inferred from the well plate fill level (*i.e.* pathlength) and relative nanoparticle concentrations with known extinction coefficients at 532 nm (3.464×10^8 $cm^{-1}M^{-1}$) at approximately 0.32 O.D., which ensured uniform sample irradiation. After illumination, the activity of the released DNAzyme was measured by adding 1 μM substrate and reaction buffer (20 mM Tris pH 7.4, 300 mM NaCl, and 10 mM $MgCl_2$) and measuring the initial rate of substrate hydrolysis.

a

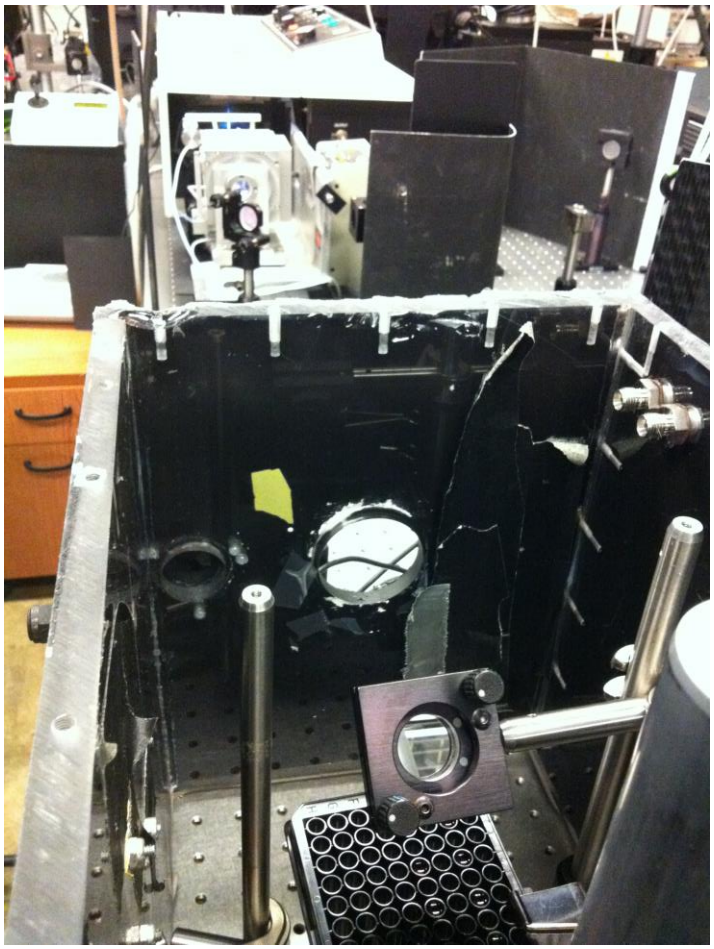

b

Figure 2.10. Photo (**a**) and schematic (**b**) of laser set up.

2.4.11 Mercaptoethanol (ME) passivation of DzNPs

$DzT_{10}NP$ and $Dz_{rev}T_{10}NP$ (6 nM) were passivated with ME (12 mM) for 5 and 15 minutes respectively in Nanopure water. After incubation, the particles were washed 6 times by centrifuging the particles for ten minutes at 13,500 RPM into pellets, decanting the supernatant, and resuspending in Nanopure water. The DNAzyme surface density was measured as described above (DNA density assay). Catalysis was measured at the following reaction conditions: 25 °C, 0.75 nM DzNP, 1 μM substrate, 20 mM CHES pH 8.6, 150 mM NaCl, and 50 mM $MgCl_2$.

2.5 References

(1) Elbaz, J.; Lioubashevski, O.; Wang, F. A.; Remacle, F.; Levine, R. D.; Willner, I., DNA Computing Circuits Using Libraries of DDNAzyme Subunits. *Nature Nanotechnology* **2010**, *5*, 417-422.

(2) Chien, M. P.; Thompson, M. P.; Gianneschi, N. C., DNA-Nanoparticle Micelles as Supramolecular Fluorogenic Substrates Enabling Catalytic Signal Amplification and Detection by DNAzyme Probes. *Chem. Commun.* **2011**, *47*, 167-169.

(3) Lee, J. H.; Wang, Z. D.; Liu, J. W.; Lu, Y., Highly Sensitive and Selective Colorimetric Sensors for Uranyl (UO_2^{2+}) : Development and Comparison of Labeled and Label-Free DNAzyme-Gold Nanoparticle Systems. *J. Am. Chem. Soc.* **2008**, *130*, 14217-14226.

(4) Mazumdar, D.; Liu, J. W.; Lu, G.; Zhou, J. Z.; Lu, Y., Easy-to-use Dipstick Tests For Detection of Lead in Paints Using Non-Cross-Linked Gold Nanoparticle-DNAzyme Conjugates. *Chem. Commun.* **2010**, *46*, 1416-1418.

(5) Fokina, A. A.; Meschaninova, M. I.; Durfort, T.; Venyaminova, A. G.; Francois, J. C., Targeting Insulin-like Growth Factor I with 10-23 DNAzymes: 2 '-O-Methyl Modifications in the Catalytic Core Enhance mRNA Cleavage. *Biochemistry (Mosc).* **2012**, *51*, 2181-2191.

(6) Santoro, S. W.; Joyce, G. F., A General Purpose RNA-cleaving DNA Enzyme. *Proc. Natl. Acad. Sci. U. S. A.* **1997**, *94*, 4262-4266.

(7) Niewiarowska, J.; Sacewicz, I.; Wiktorska, M.; Wysocki, T.; Stasikowska, O.; Wagrowska-Danilewicz, M.; Cierniewski, C. S., DNAzymes to Mouse Beta 1 Integrin mRNA *in vivo*: Targeting the Tumor Vasculature and Retarding Cancer Growth. *Cancer Gene Ther.* **2009**, *16*, 713-722.

(8) Elahy, M.; Dass, C. R., Dz13: c-Jun Downregulation and Tumour Cell Death. *Chem Biol Drug Des* **2011**, *78*, 909-912.

(9) Fahmy, R. G.; Dass, C. R.; Sun, L. Q.; Chesterman, C. N.; Khachigian, L. M., Transcription Factor Egr-1 Supports FGF-Dependent Angiogenesis During Neovascularization and Tumor Growth. *Nat. Med.* **2003**, *9*, 1026-1032.

(10) Mitchell, A.; Dass, C. R.; Sun, L. Q.; Khachigian, L. M., Inhibition of Human Breast Carcinoma Proliferation, Migration, Chemoinvasion and Solid Tumour Growth by

DNAzymes Targeting the Zinc Finger Transcription Factor EGR-1. *Nucleic Acids Res.* **2004**, *32*, 3065-3069.

(11) Zhou, J.; Yang, X. Q.; Xie, Y. Y.; Zhao, X. D.; Jiang, L. P.; Wang, L. J.; Cui, Y. X., Inhibition of Respiratory Syncytial Virus of Subgroups A and B Using Deoxyribozyme DZ1133 in Mice. *Virus Res.* **2007**, *130*, 241-248.

(12) Dass, C. R.; Choong, P. F. M.; Khachigian, L. M., DNAzyme Technology and Cancer Therapy: Cleave and Let Die. *Mol. Cancer Ther.* **2008**, *7*, 243-251.

(13) Baum, D. A.; Silverman, S. K., Deoxyribozymes: Useful DNA Catalysts *in vitro* and *in vivo*. *Cell. Mol. Life Sci.* **2008**, *65*, 2156-2174.

(14) Schubert, S.; Gul, D. C.; Grunert, H. P.; Zeichhardt, H.; Erdmann, V. A.; Kurreck, J., RNA Cleaving '10-23' DNAzymes with Enhanced Stability and Activity. *Nucleic Acids Res.* **2003**, *31*, 5982-5992.

(15) Abdelgany, A.; Wood, M.; Beeson, D., Hairpin DNAzymes: A New Tool for Efficient Cellular Gene Silencing. *J. Gene Med.* **2007**, *9*, 727-738.

(16) Manea, F.; Houillon, F. B.; Pasquato, L.; Scrimin, P., Nanozymes: Gold-Nanoparticle-Based Transphosphorylation Catalysts. *Angew Chem., Int. Edit.* **2004**, *43*, 6165-6169.

(17) Miles, E. W.; Rhee, S.; Davies, D. R., The Molecular Basis of Substrate Channeling. *J. Biol. Chem.* **1999**, *274*, 12193-12196.

(18) Park, S.-J.; Lazarides, A. A.; Storhoff, J. J.; Pesce, L.; Mirkin, C. A., The Structural Characterization of Oligonucleotide-Modified Gold Nanoparticle Networks

Formed by DNA Hybridization. *The Journal of Physical Chemistry B.* **2004**, *108*, 12375-12380.

(19) Pellegrino, T.; Sperling, R. A.; Alivisatos, A. P.; Parak, W. J., Gel Electrophoresis of Gold-DNA Nanoconjugates. *J. Biomed. Biotechnol.* **2007**, 26796-26804.

(20) Macfarlane, R. J.; Lee, B.; Jones, M. R.; Harris, N.; Schatz, G. C.; Mirkin, C. A., Nanoparticle Superlattice Engineering with DNA. *Science* **2011**, *334*, 204-208.

(21) Rosi, N. L.; Giljohann, D. A.; Thaxton, C. S.; Lytton-Jean, A. K. R.; Han, M. S.; Mirkin, C. A., Oligonucleotide-Modified Gold Nanoparticles for Intracellular Gene Regulation. *Science* **2006**, *312*, 1027-1030.

(22) Giljohann, D. A.; Seferos, D. S.; Prigodich, A. E.; Patel, P. C.; Mirkin, C. A., Gene Regulation with Polyvalent siRNA-Nanoparticle Conjugates. *J. Am. Chem. Soc.* **2009**, *131*, 2072-2073.

(23) Lytton-Jean, A. K. R.; Mirkin, C. A., A Thermodynamic Investigation into the Binding Properties of DNA Functionalized Gold Nanoparticle Probes and Molecular Fluorophore Probes. *J. Am. Chem. Soc.* **2005**, *127*, 12754-12755.

(24) Wang, H. B.; Xu.; Zhang, H.; Li, D. W.; Yang, Z. Q.; Xie, X. J.; Li, T. H.; Liu, X. G., EcoRI-Modified Gold Nanoparticles for Dual-Mode Colorimetric Detection of Magnesium and Pyrophosphate Ions. *Small* **2011**, 7, 1987-1992.

(25) Xiaoji Xie, W. X., and Xiaogang Liu, Improving Colorimetric Assays through Protein Enzyme-Assisted Gold Nanoparticle Amplification. *Acc. Chem. Res.* **2012**, Article ASAP.

(26) Seferos, D. S.; Prigodich, A. E.; Giljohann, D. A.; Patel, P. C.; Mirkin, C. A., Polyvalent DNA Nanoparticle Conjugates Stabilize Nucleic Acids. *Nano Lett.* **2009**, *9*, 308-311.

(27) Giljohann, D. A.; Seferos, D. S.; Patel, P. C.; Millstone, J. E.; Rosi, N. L.; Mirkin, C. A., Oligonucleotide Loading Determines Cellular Uptake of DNA-modified Gold Nanoparticles. *Nano Lett.* **2007**, *7*, 3818-3821.

(28) Massich, M. D.; Giljohann, D. A.; Seferos, D. S.; Ludlow, L. E.; Horvath, C. M.; Mirkin, C. A., Regulating Immune Response Using Polyvalent Nucleic Acid-Gold Nanoparticle Conjugates. *Mol Pharmaceut* **2009**, *6*, 1934-1940.

(29) Taton, T. A.; Mirkin, C. A.; Letsinger, R. L., Scanometric DNA Array Detection with Nanoparticle Probes. *Science* **2000**, *289*, 1757-1760.

(30) Nowakowski, J.; Shim, P. J.; Prasad, G. S.; Stout, C. D.; Joyce, G. F., Crystal Structure of an 82-Nucleotide RNA-DNA Complex Formed by the 10-23 DNA Enzyme. *Nat. Struct. Biol.* **1999**, *6*, 151-156.

(31) Liu, J. W.; Lu, Y., A Colorimetric Lead Biosensor Using DNAzyme-directed Assembly of Gold Nanoparticles. *J. Am. Chem. Soc.* **2003**, *125*, 6642-6643.

(32) Wang, Z. D.; Lee, J. H.; Lu, Y., Label-Free Colorimetric Detection of Lead Ions with a Nanomolar Detection Limit and Tunable Dynamic Range by Using Gold Nanoparticles and DNAzyme. *Adv. Mater.* **2008**, *20*, 3263-3267.

(33) Ryoo, S. R.; Jang, H.; Kim, K. S.; Lee, B.; Kim, K. B.; Kim, Y. K.; Yeo, W. S.; Lee, Y.; Kim, D. E.; Min, D. H., Functional Delivery of DNAzyme with Iron Oxide

Nanoparticles for Hepatitis C Virus Gene Knockdown. *Biomaterials* **2012**, *33*, 2754-2761.

(34) Hurst, S. J.; Lytton-Jean, A. K. R.; Mirkin, C. A., Maximizing DNA Loading on a Range of Gold Nanoparticle Sizes. *Anal. Chem.* **2006**, *78*, 8313-8318.

(35) Demers, L. M.; Mirkin, C. A.; Mucic, R. C.; Reynolds, R. A.; Letsinger, R. L.; Elghanian, R.; Viswanadham, G., A Fluorescence-based Method for Determining the Surface Ccoverage and Hybridization Efficiency of Thiol-Capped Oligonucleotides Bound to Gold Thin Films and Nanoparticles. *Anal. Chem.* **2000**, *72*, 5535-5541.

(36) Palegrosdemange, C.; Simon, E. S.; Prime, K. L.; Whitesides, G. M., Formation of Self-Assembled Monolayers by Chemisorption of Derivatives of Oligo(Ethylene Glycol) of Structure $HS(Ch_2)_{11}(OCH_2CH_2)_m$-OH on Gold. *J. Am. Chem. Soc.* **1991**, *113*, 12-20.

(37) Liu, J. W.; Lu, Y., Optimization of a Pb^{2+}-directed Gold Nanoparticle/DNAzyme Assembly and Its Application as a Colorimetric Biosensor for Pb^{2+}. *Chem. Mater.* **2004**, *16*, 3231-3238.

(38) Zaborowska, Z.; Furste, J. P.; Erdmann, V. A.; Kurreck, J., Sequence Requirements in the Catalytic Core of the "10-23" DNA Enzyme. *J. Biol. Chem.* **2002**, *277*, 40617-40622.

(39) Richards, J. L.; Seward, G. K.; Wang, Y. H.; Dmochowski, I. J., Turning the 10-23 DNAzyme On and Off with Light. *ChemBioChem* **2010**, *11*, 320-324.

(40) Jain, P. K.; Shah, S.; Friedman, S. H., Patterning of Gene Expression Using New Photolabile Groups Applied to Light Activated RNAi. *J. Am. Chem. Soc.* **2010**, *133*, 440-446.

(41) Prokup, A.; Hemphill, J.; Deiters, A., DNA Computation: A Photochemically Controlled AND Gate. *J. Am. Chem. Soc.* **2012**, *134*, 3810-3815.

(42) Poon, L.; Zandberg, W.; Hsiao, D.; Erno, Z.; Sen, D.; Gates, B. D.; Branda, N. R., Photothermal Release of Single-Stranded DNA from the Surface of Gold Nanoparticles Through Controlled Denaturating and Au−S Bond Breaking. *ACS Nano* **2010**, *4*, 6395-6403.

(43) Young, D. D.; Lively, M. O.; Deiters, A., Activation and Deactivation of DNAzyme and Antisense Function with Light for the Photochemical Regulation of Gene Expression in Mammalian Cells. *J. Am. Chem. Soc.* **2010**, *132*, 6183-6193.

(44) Zhou, M. G.; Liang, X. G.; Mochizuki, T.; Asanuma, H., A Light-Driven DNA Nanomachine for the Efficient Photoswitching of RNA Digestion. *Ange.w Chem., Int. Edit.* **2010**, *49*, 2167-2170.

(45) Bootcov, M. R.; Bauskin, A. R.; Valenzuela, S. M.; Moore, A. G.; Bansal, M.; He, X. Y.; Zhang, H. P.; Donnellan, M.; Mahler, S.; Pryor, K.; *et al.* , MIC-1, A Novel Macrophage Inhibitory Cytokine, is a Divergent Member of the TGF-Beta Superfamily. *Proc. Natl. Acad. Sci. U. S. A.* **1997**, *94*, 11514-11519.

(46) Welsh, J. B.; Sapinoso, L. M.; Kern, S. G.; Brown, D. A.; Liu, T.; Bauskin, A. R.; Ward, R. L.; Hawkins, N. J.; Quinn, D. I.; Russell, P. J.; *et al.* , Large-Scale Delineation

of Secreted Protein Biomarkers Overexpressed in Cancer Tissue and Serum. *Proc. Natl. Acad. Sci. U. S. A.* **2003**, *100*, 3410-3415.

(47) Staff, A. C.; Bock, A. J.; Becker, C.; Kempf, T.; Wollert, K. C.; Davidson, B., Growth Differentiation Factor-15 as a Prognostic Biomarker in Ovarian Cancer. *Gynecol. Oncol.* **2010**, *118*, 237-243.

(48) Chang, J. T.-C.; Chan, S.-H.; Lin, C.-Y.; Lin, T.-Y.; Wang, H.-M.; Liao, C.-T.; Wang, T.-H.; Lee, L.-Y.; Cheng, A.-J., Differentially Expressed Genes in Radioresistant Nasopharyngeal Cancer Cells: gp96 and GDF15. *Mol. Cancer Ther.* **2007**, *6*, 2271-2279.

(49) Joshi, J. P.; Brown, N. E.; Griner, S. E.; Nahta, R., Growth Differentiation Factor 15 (GDF15)-mediated HER2 Phosphorylation Reduces Trastuzumab Sensitivity of HER2-Overexpressing Breast Cancer Cells. *Biochem. Pharmacol.* **2011**, *82*, 1090-1099.

(50) Nahta, R.; Esteva, F. J., Herceptin: Mechanisms of Action and Resistance. *Cancer Lett.* **2006**, *232*, 123-138.

(51) Hill, H. D.; Mirkin, C. A., The Bio-Barcode Assay for the Detection of Protein and Nucleic Acid Targets Using DTT-induced Ligand Exchange. *Nat Protoc.* **2006**, *1*, 324-336.

(52) Sato, K.; Hosokawa, K.; Maeda, M., Rapid Aggregation of Gold Nanoparticles Induced by Non-Cross-Linking DNA Hybridization. *J. Am. Chem. Soc.* **2003**, *125*, 8102-8103.

Chapter 3: *In vivo* efficacy of DNAzyme nanoparticles as an anti-inflammatory therapy following myocardial infarction

3.1 Introduction

In the previous chapter, we demonstrated that DNAzyme functionalized particles (DzNPs) are highly stable and can efficiently regulate gene expression *in vitro*. However, an immortalized cell line was used as a model system for these proof-of-principle studies and does not best represent the physiology of a therapeutic scenario. Therefore, this chapter will discuss an expansion upon these findings where a detailed study investigating the efficacy of DzNPs in a primary cell model and in an *in vivo* rat model was undertaken, which better represents the therapeutic physiology. As a model system, we chose to target an inflammatory pathology in context to heart failure due to its broad societal impact and to highlight the limited cytotoxicity DzNPs possess because the root cause of heart failure is inflammation where treatment of cancers and other pathologies has a higher threshold for toxicity.

Heart failure (HF) is the leading cause of death in the developed world today and ischemic heart disease is considered to be the dominant cause.[1] Myocardial infarction (MI), most commonly known as a "heart attack" is the initial occurrence, which involves a thrombotic occlusion of a coronary artery and subsequent depletion of oxygen to a segment of the left ventricular wall. Over the last few decades, mortality due to MI has decreased due to the optimized reperfusion strategies employing sophisticated designs of stents, thrombolytic therapies and neurohormonal inhibitors that reduce the heart's workload.[2,3] Despite these advancements, the incidence of HF as a direct consequence of MI remains high suggesting that the current therapeutic regimen fails to target key aspects of the pathophysiological mechanisms leading to HF.[3,4] An early and crucial step in the process of cardiac repair is the inflammatory reaction that begins with the influx of neutrophils and

macrophages that absorb the necrotic tissue.[5-8] However, unbridled inflammation fueled by continuous up-regulation of pro-inflammatory cytokines can exacerbate tissue damage, thus contributing to adverse cardiac remodeling and non-contractile scar formation that ultimately culminates in HF.[9-12] Much interest has been devoted to studying the role of inflammation in the progression of HF, and interestingly, many pharmacological therapies with demonstrated efficacy for the management of the disease exhibit anti-inflammatory properties distinct from their perceived primary mechanism of action, suggesting modulation of inflammation as a contributing factor to the clinical benefit ascribed to these medications.[4,9]

The pro-inflammatory cytokine TNFα is an extensively studied potential therapeutic target implicated in many of the processes involved in the development of HF. The pathological mechanism for TNFα mediated myocardial dysfunction is thought to occur through a combination of factors that includes induction of reactive oxygen and nitrogen species, initiation of pro-inflammatory cytokine cascades and down-regulation of contractile proteins.[13-18] Infusion of TNFα to rats and dogs with normal cardiac function at levels comparable to that reported in patients with chronic heart failure (CHF) has been shown to depress ventricular function and cause adverse remodeling, recapitulating CHF conditions.[13,15] However, several reports have also indicated that TNFα involvement in the early repair process is important in that physiological levels of TNFα can be cardioprotective.[19-21] Therefore, selection of an optimal therapeutic window as well as duration of action are critical in targeting TNFα as an anti-inflammatory therapy in order to suppress the elevated inflammatory response immediately following MI.

Despite the volumes of encouraging pre-clinical data for TNFα antagonism, human trials employing a soluble TNFα receptor (etanercept) or a monocolonal antibody (infliximab) designed to neutralize TNFα have failed to demonstrate long-term clinical benefit in patients with chronic HF post-MI.[22] Failure analyses of these studies showed that these protein based therapeutics can act as agonists and stabilizers of TNFα (etanercept) and even induce cytotoxicity in cells (infliximab), which renders them highly unsuitable as therapeutic candidates in the context of HF.[22,23] Results from these trials demonstrate a clear need for careful selection of the mechanism of TNFα antagonism, as the nature of inhibition is a crucial factor for an anti-inflammatory therapy in the setting of heart failure. Furthermore, while the past clinical trials have targeted patients with advanced chronic heart failure, mounting evidence suggests the importance of early intervention to contain the initial inflammatory phase post-MI in order to halt the progression of the disease as opposed to treating the symptoms of chronic inflammation at later stages.[24] Therefore designing and evaluating approaches to deliver transient, but potent suppression of TNFα during the critical acute inflammatory stage is an important step towards successfully translating TNFα antagonism as a treatment strategy for acute MI.

Gene silencing therapeutics derived from nucleic acid oligomers are excellent candidates that can circumvent many of the above mentioned limitations of the protein based strategies since they are potent, yet transient in regulating target gene expression. We investigated catalytic DNA, a novel modality of gene silencing molecules, to inhibit TNFα mRNA. These DNA enzymes (DNAzymes) are composed of a 15 base catalytic core and flanked by two recognition arms that can selectively degrade target mRNA independent of RNAi, thus avoiding the need to hijack the host cell's machinery for

catalysis. Compared to siRNA mediated gene silencing, they offer the added advantages of enhanced stability (DNA versus RNA), cost-effecive synthesis and lack of immune response caused by double stranded RNA. DNAzyme therapies have shown great potential in pre-clinical trials in treating a wide variety of ailments ranging from cancer to spinal cord injury including myocardial infarction, notably targeting transcription factors c-Jun and Egr-1 for knockdown.[25-29] DNAzymes are also currently in human trials for treating nasopharyngeal carcinoma.[30] However, delivery of therapeutic nucleic acids is an immense challenge due to the difficulties in getting highly negatively charged oligomers across a cell membrane and protecting them from nuclease-mediated degradation.[31,32] Current delivery methods include complexing of nucleic acids to cationic lipids, although inherent toxicity and the positively charged surface characteristics that elicit immune responses deem such vehicles unsuitable for treating inflammatory pathologies.[33] A powerful, yet emerging approach for transfection entails spatially organizing therapeutic oligonucleotides into a compact spherical nanostructure.[34,35] Such structures enable very efficient transfection through a scavenger receptor mediated mechanism.[36] In fact, transfection is so efficient that spherical nucleic acids have been shown to readily enter a mouse's epithelial layer to regulate EGFR expression and even cross the blood brain barrier to treat glioblastoma.[37,38] In previous work, we have demonstrated enhanced catalytic gene silencing activity demonstrated by DNAzymes when functionalized in similar spherical nucleic acid structures[39]. Herein, we tested whether DNAzyme functionalized gold nanoparticles could be effective anti-inflammatory agents in the heart by regulating TNFα expression in a rodent model of MI with the ultimate goal of minimizing damage to the heart and preventing HF.

3.2 Results and Discussion

3.2.1 Synthesis and characterization of DzNPs

Citrate stabilized gold nanoparticles were synthesized by reducing chloroauric acid ($HAuCl_4$) with sodium citrate. The gold particles were functionalized with thiolated DNA via self-assembly with salt titration incorporated to achieve high density DNA loading (**Figure 3.1a**). Particles were functionalized with catalytically active (Dz), inactive (i-Dz) or active but nonspecific DNAzyme (NS-Dz) with a loading of 99±3, 109±7, and 65±2 oligonucleotides per nanoparticle, respectively. This equates to a high surface density ranging from 6 – 9 nm^2/DNA, sufficient to ensure optimal activity. It should be noted that NS-Dz has a lower DNA density on the particle due to possessing a stable secondary hairpin structure. For *in vitro* and *in vivo* imaging studies, Cy5-labeled nonspecific DNAzyme modified particles (Cy5-NS-Dz) were synthesized in a similar manner. The resulting particles were very homogeneous and monodisperse with a mean particle diameter of 14±3 nm as determined by TEM analysis. The extinction spectra showed a peak at 525 nm corresponding to the nanoparticle's surface plasmon resonance (**Figure 3.1b-d**).

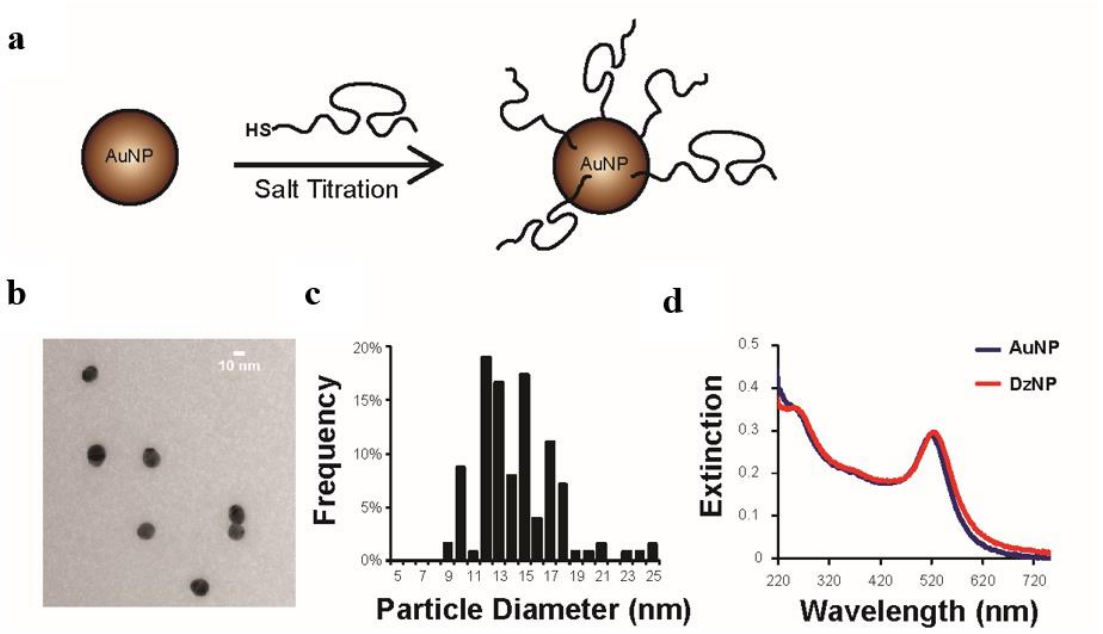

Figure 3.1. (**a**) Schematic showing the approach used to synthesize DNAzyme modified gold nanoparticles. Thiolated DNA was mixed with gold nanoparticles, and the salt concentration was gradually increased. (**b**) Representative TEM image of the 14 nm citrate stabilized gold nanoparticles. (**c**) Particle polydispercity was determined by histogram analysis of TEM images. (**d**) Extinction spectra of citrate stabilized (AuNP) and DNAzyme functionalized gold nanoparticles (DzNP) showing the surface plasmon resonance at 525 nm.

3.2.2 Internalization of DzNPs by macrophages and myocytes in vitro

Intracellular uptake is a key requirement for the successful delivery of nucleic acids. [40] We tested the cellular uptake of these particles in macrophages by measuring fluorescence of RAW 264.1 macrophages treated with 5 nM Cy5-NS-Dz particles (300 nM DNA) *in vitro*. We observed non-punctate, diffuse fluorescence intracellularly (**Figure 3.2a**) in macrophages treated with the Dz-NPs at the 1 hour time point. This indicates that the DNA is diffusely localized to the cytoplasm, in agreement with literature precedent for other cell types.[34] We qualitatively compared the particle uptake with the most commonly used commercial transfection reagent Lipofectamine® RNAiMAX complexed with equivalent DNA concentration (300 nM) through a time course of 24 hours. While the DzNPs were taken up by macrophages as early as 1 hour (**Figure 3.2b, left**) and are continually taken

up through 24 hours, Lipofectamine®-mediated transfection was only detected inside cells at the 24 hour time point, and in punctate signals indicating possible entrapment within the endosomal compartments (**Figure 3.2b, right**). Phagocytic cells such as macrophages are a particulalry challenging target for transfection and gene silencing, as they are programmed to take up and degrade foreign particles. However, the mechanism of particle internalization is dependent on particle size. Particles below 500 nm in size are usually taken up via endocytosis in phagocytic and non-phagocytic cells,[41] which is preferable in the context of therapeutic delivery. Accordingly, we further show that these particles are taken up by non-phagocytic adult rat cardiomyocytes at 18 hours following transfection. Notably, there was no observable fluorescence in cardiomyocytes transfected with Cy5-DNA utilizing Lipofectamine® RNAiMAX (**Figure 3.2c,d**).

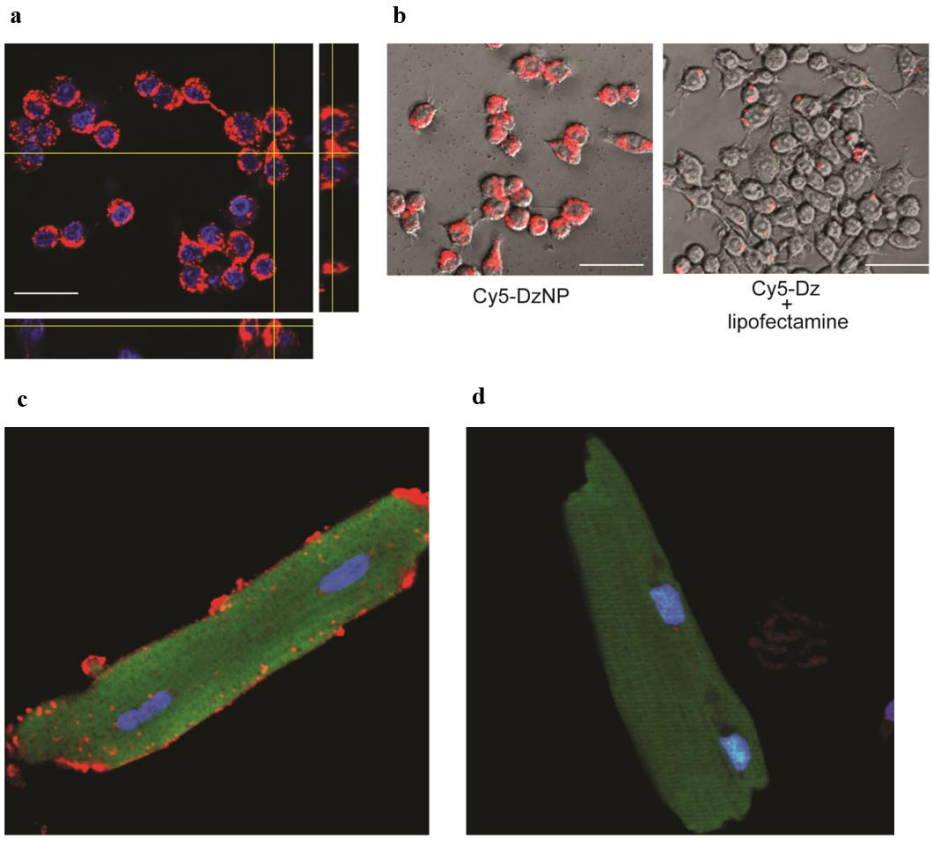

Figure 3.2. (**a**) RAW 264.7 macrophages were treated with 5 nM Cy5 labeled NS-DNA modified AuNPs. Following 1 hour of treatment, cells were imaged using confocal microscopy to visualize cytoplasmic localization of Cy-5-DNA. Representative Z-stack image confirms internalized nanoparticles within macrophages (scale bar, 30 μm). (**b**) Uptake efficiency was compared in macrophages treated with equivlant cocnentraions of DNA containing Dz-particles at 1 hour (left) or lipofectamine® transfection reagent for 24 hours (right). DNA (red, Cy5), Nucleus (blue, DAPI). (Scale bar, 30 μm). Adult rat cardiomyocytes were fixed and imaged 18 hours post-transfection with 5 nM Cy5 labeled DNA by Cy5-dzNPs (**c**) or Lipofectamine® mediated transfection (**d**). DNA (red, Cy5), Nucleus (blue, DAPI), cellular morphology stain (green, FITC-Maleimide).

3.2.3 DzNPs in vitro cytotoxicity

We investigated whether DNAzyme functionalized AuNPs are a biocompatible delivery vehicle and whether we could deliver catalytically active Dz into macrophages and inhibit TNFα expression *in vitro.* In order to establish an *in vitro* model to demonstrate knockdown of TNFα we stimulated primary peritoneal cavity isolated macrophages with bacterial endotoxin LPS to upregulate the production of TNFα following particle treatment. LPS stimulates TNFα expression via activation of the Toll Like Receptor (TLR), orchestrating a potent inflammatory response, and therefore TNFα expression additionally serves as a surrogate assay to evaluate the cytotoxicity profile of particle uptake compared to the commonly used transfection reagent Lipofectamine® RNAiMAX. Upon treatment with Lipofectamine®, macrophages exhibited ~4 fold higher TNFα levels compared to the basal LPS stimulation, illustrating the cytotoxic response elicited by cationic lipids, which are widely used for nucleic acid delivery. The nonspecific DNAzyme particle (NS-Dz) treatment caused no significant additional cytotoxicity over the control group (**Figure 3.3**), thus indicating that DNAzyme functionalized particles do not elicit cytotoxicity and are suitable for applications in an inflammatory disease context such as the post-MI myocardium.

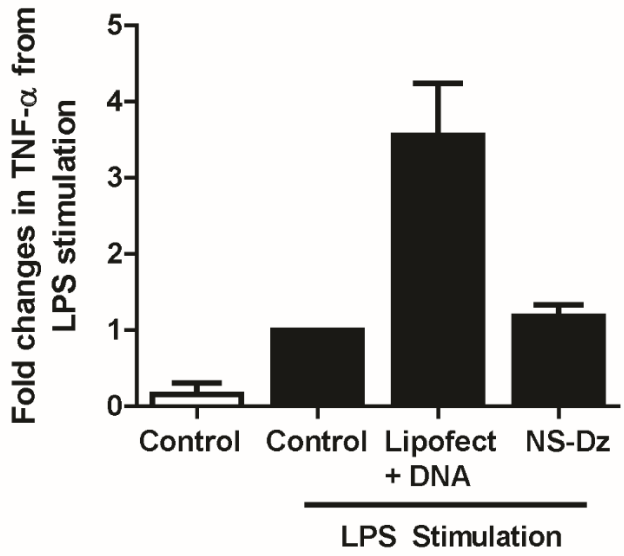

Figure 3.3. Plot showing the fold change in TNFα levels in untreated and LPS-stimulated macrophages that were also treated with lipofectamine® as well as NS-Dz AuNPs. TNFα levels were measured using an ELISA kit at the 24 hour time point and were normalized to untreated LPS stimulated cells and reported as fold changes in TNFα. Grouped data (mean ± SEM, *n*=3).

3.2.4 In vitro TNFα knockdown

To determine the intracellular catalytic activity of DNAzyme AuNP conjugates within the *in vitro* macrophage model, active and inactive DNAzymes modified particles were synthesized targeting the start codon (AUG) of the TNFα mRNA displaying minimal secondary structure. The recognition arms were 7 and 10 bases in length, which was designed based on literature precedent defining DNAzyme design rules as shown in **Figure 3.4a**.[26] A single base mutation was introduced in the 15 base catalytic core to inhibit DNazyme activity of the i-Dz sequence, thus allowing one to distinguish antisense knockdown from DNAzyme mediated knockdown (**Figure 3.4a**). To minimize DNAzyme degradation, four 2'-methyl ether modifications were added to the termini of the recognition arms. Surprisingly, initial tests using DNAzymes with 10 mer long arms showed limited activity, and Dz and i-Dz treated macrophages showed only 14% and 2%

knockdown, respectively (**Figure 3.4**). We hypothesized that this was caused by product inhibition due to high stability of the 10 base recognition arms.

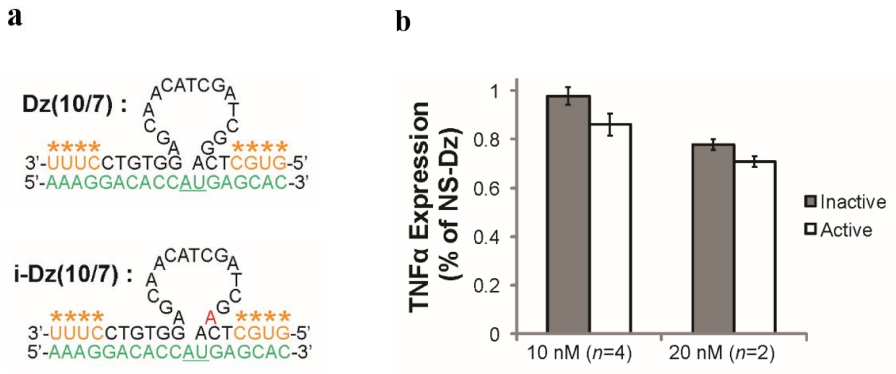

Figure 3.4. (a) Schematic showing the original DNAzyme design targeting TNFα mRNA (green) with recognition arm lengths 10 and 7 base pairs and eight 2' methyl ether modifications (*, yellow) to enhance stability. The inactive DNAzyme has a single base mutation shown in red to inhibit RNA hydrolysis. (**b**) *In vitro* TNFα knockdown in primary macrophages where cells were treated with either active (Dz), inactive (i-Dz), or non-specific (NS-Dz) DNAzyme modified gold nanoaprticles at 10 nM or 20 nM concentrations. TNFα expression was measured by ELISA and the results were normalized to NS-Dz treated cells and reported as percent TNFα expression. Little knockdown (2% and 14% for Dz and i-Dz, respectively) was observed for cells treated with particles at 10 nM concentrations where higher knockdown (23% and 30% for Dz and i-Dz, respectively) was observed for cells treated with 20 nM concentration. At both concentrations, little difference was observed between Dz and i-Dz modified particles due to product inhibition. In the optimized design, the 10 base pair recognition sequence was decreased to 7 base pairs, which significantly increased knockdown.

To address this concern, the recognition sequence for one of the arms was shortened from 10 to 7, in addition to changing the two terminal thymidine bases in the T10 spacer region to two cytosines, to reduce the affinity to the mRNA target. In the optimized design (**Figure 3.5a**), compared to control LPS stimulated cells, only Dz particles showed significant (~50%) reduction in TNFα levels while NS-Dz and i-Dz particles showed no effect (**Figure 3.5b**). Together, these results show that spherical nucleic acids can efficiently deliver catalytically active DNAzymes to macrophages and decrease the expression of TNFα in activated macrophages.

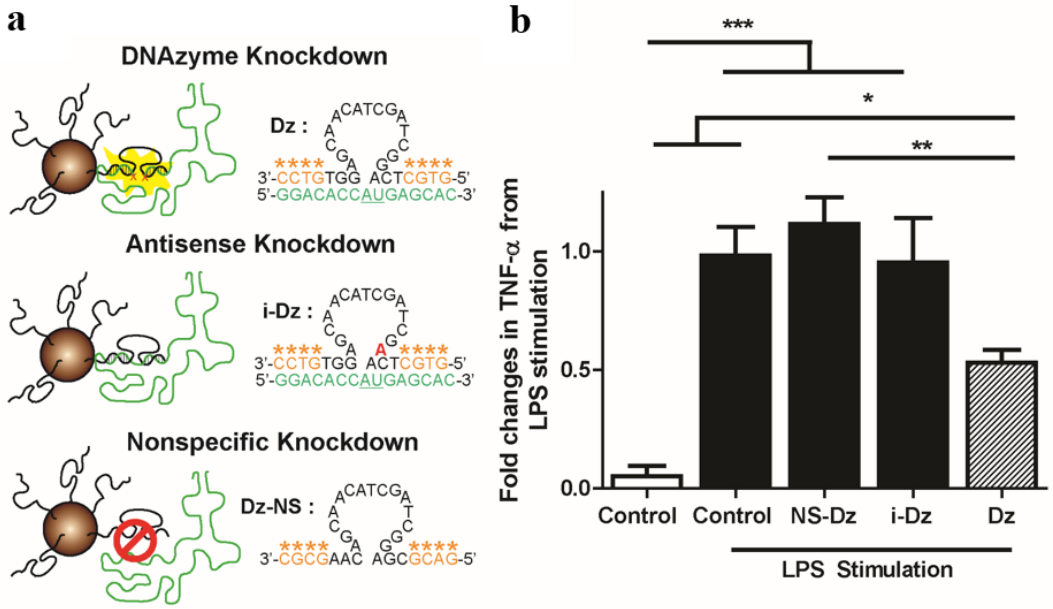

Figure 3.5. (**a**) Schematic showing the sequences used for the Dz, iDz, and Dz-NS AuNP conjugates. Green indicates the mRNA sequence, underlined bases denotes the location of phosphodiester hydrolysis. The red base shows the location of the mutation that leads to inhibition of Dz catalytic function. **b**) Plot of TNF-α expression levels when macrophages are treated with NS-Dz, i-Dz, and Dz AuNP conjugates at the 24 hour time point. Grouped data (mean +/- SEM; n=6). (*p<0.05, **p<0.01, ***p<0.001; One way ANOVA followed by Tukey's Multiple Comparison post-test.

3.2.5 Ex vivo biodistribution of DzNPs determined by fluorescence imaging

We next investigated the ability of these particles to deliver DNAzymes to the myocardium in a rat model of MI. Cy5-NS-Dz modified gold particles were injected intramyocardially to 3 different regions of the infarct following MI surgery. This route of delivery is clinically relevant in the context of MI since routine interventional procedures such as primary percutaneous interventions (PCI) post-MI require catheterization and can be leveraged for site-specific therapeutic administration.[42] The time-course *ex-vivo* bioimaging revealed strong Cy5 fluorescence emitting from the heart for all 3 days tested indicating efficient particle uptake and retention in the myocardium following injection for at least 3 days (**Figure 3.6**). Due to the pulsatile nature of the heart, as anticipated, particles

are introduced to the blood circulation to a certain extent, and secondary to the heart, they predominantly biodistribute to the kidney and liver, suggesting renal and/or hepatobilary clearance.

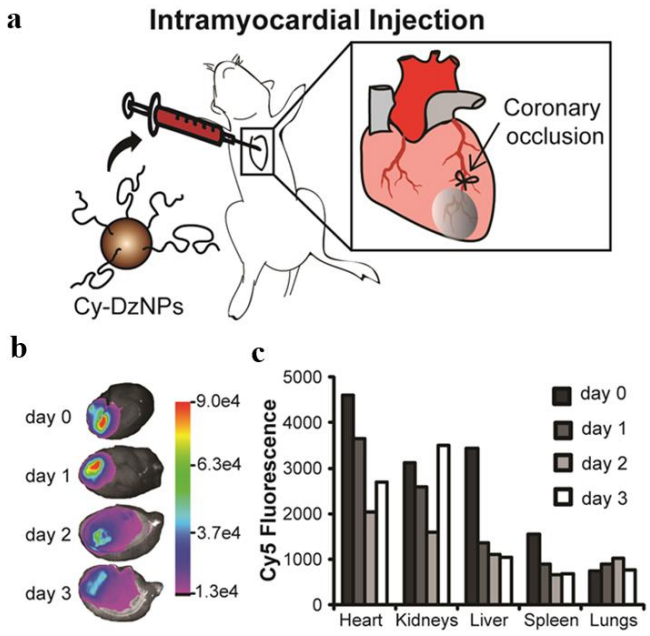

Figure 3.6. (**a**) Schematic of ligation of the coronary artery to cause permanent ligation MI in rats followed by particle injection. (**b**) Fluorescence images of hearts from each day following injection. The heat map indicates the Cy5 emission intensity in arbitrary units. (**c**) Fluorescence intensity of all organs imaged from days 0, 1, 2 and 3 (n=1). The Cy5 fluorescence intensity is expressed in arbitrary units.

3.2.6 In vivo activity of DzNPs towards down regulation of TNFα

To test the potential of DNAzyme functionalized AuNPs as an anti-inflammatory agent for the treatment of acute MI, we investigated the effect of injecting these particles to the myocardium of rats immediately following experimental MI. We used cardiac echocardiography, invasive hemodynamics measurements at a 3-day acute time point, and also measured the inflammatory gene expression profile in the left ventricular infarct tissue. As shown in **Figure 3.7a**, all groups receiving MI demonstrated significantly reduced cardiac function ($p < 0.001$) as measured in absolute change in fractional shortening

compared to sham animals. While there was no effect for NS-Dz or i-Dz particle treated groups, Dz particle treatment significantly restored function by ~40% compared to the untreated MI group ($p < 0.01$). The invasive hemodynamics measurements also indicated a trend towards improvement in both the ejection fraction (%EF) and in the parameters that measure the rate of change of pressure in the left ventricle chamber (dp/dt) in the Dz particle treated group (**Figure 3.7b,c**). Corresponding to the functional improvement, delivery of Dz significantly reduced the TNFα mRNA levels in LV tissue compared to all controls and further, exhibited no statistical significance from sham controls (**Figure 3.7d**).

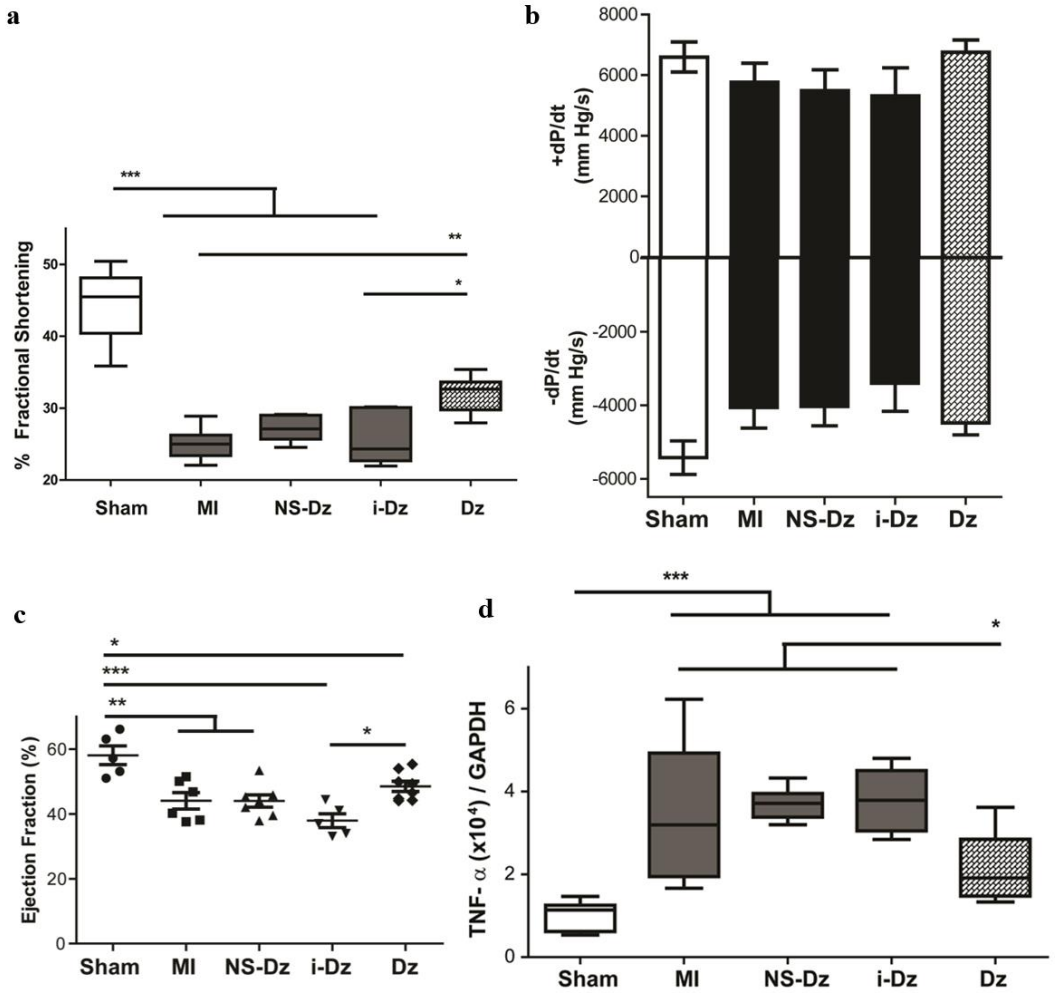

Figure 3.7. (**a**) There was a significant decrease in cardiac function in animals that received an MI compared to sham as demonstrated by % FS. Among treatment groups, there was a significant

restoration in function only in the Dz treated rats compared with untreated MI and i-Dz groups. (**b**) There was a trend towards depression of function using the dp/dt parameter in all animals that underwent MI except for the Dz treated group. However, there was no statistical significance in these parameters in any of these groups. (**c**) A significant reduction in % Ejection Fraction (%EF) was observed in all animals that underwent MI compared to sham animals. Although not statistically significant compared to MI group, Dz treated group showed a trend of improved %EF (**d**) A significant upregulation of TNFα expression was observed in animals that received an MI compared to sham. There was a significant decrease in mRNA expression in the LV infarct issue only in the Dz treated rats compared with all controls. Gene expression was evaluated by qRT-PCR using the quantitative standard curve method, and the results were normalized to GAPDH levels and reported as fold changes in copy number of mRNA levels compared to sham animals. Grouped data (mean ± SEM; *n*=5-9 for each group, *n*=41 total) from 3 days. (*p<0.05; (**p<0.01 ***p<0.001; one-way ANOVA followed by Tukey's Multiple Comparison post-test). Plots represent grouped data (mean ± SEM; n=5-9) from 3 days.

Several studies have illustrated the central role that TNFα plays in myocardial dysfunction by propagating pro-inflammatory cytokines such as IL-6 and IL-1β that acutely regulate myocyte survival/apoptosis and trigger further cellular inflammation including oxidative stress and recruitment of inflammatory cells to the infarct.[12,43-45] Therefore, to determine the downstream effect by down regulating TNFα by DNAzymes, we measured the gene expression profile of commonly upregulated pro-inflammatory mediators IL-12β, IL-1β, IL-6 as well as iNOS, an inducible form of Nitric oxide (NO) synthase stimulated by cytokines such as TNFα and IL-1β (**Figure 3.8**).[46] Silencing TNFα gene expression resulted in a strong anti-inflammatory effect that disrupted the gene expression of these pro-inflammatory markers.

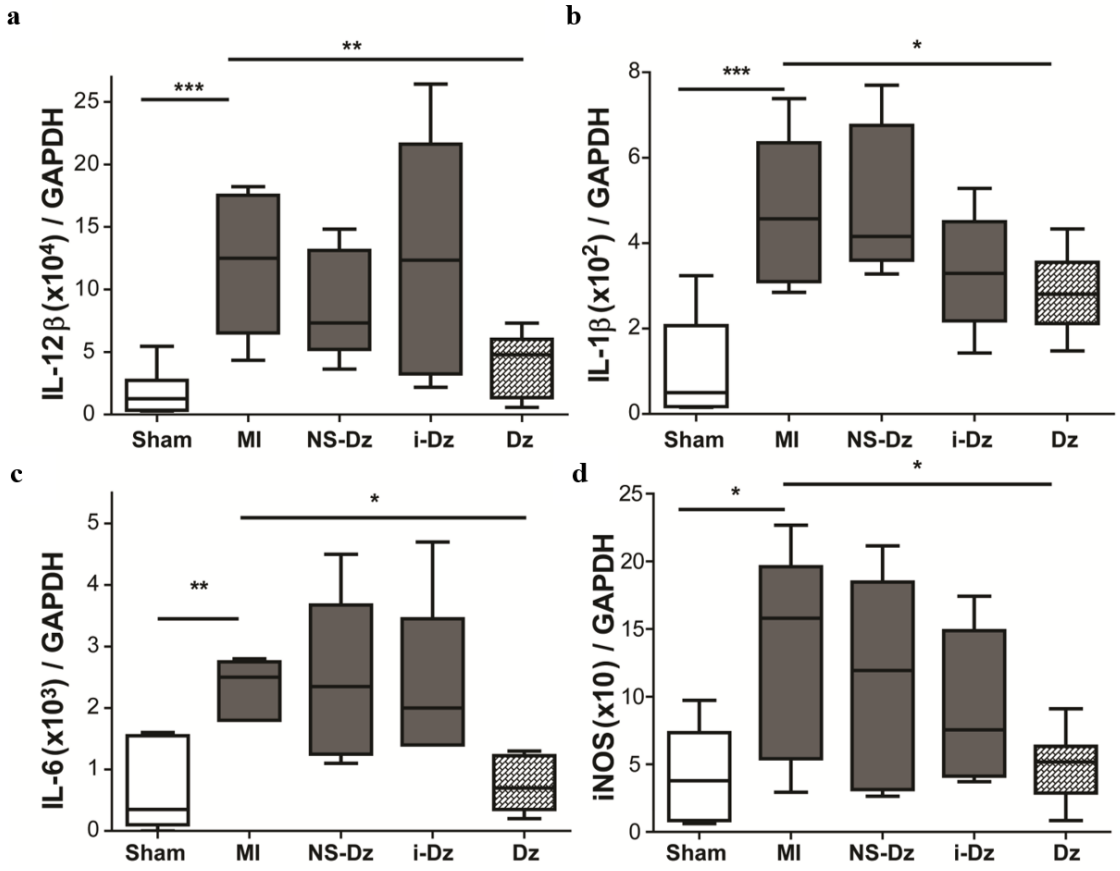

Figure 3.8. Grouped data (mean ± SEM; n=5-9) from LV infarct tissue at 3 days following MI and injection. There was a significant upregulation in gene expression of pro-inflammatory cytokines (**a**) IL-12β, (**b**) IL-1 β, (**c**) IL-6 as well as (**d**) iNOS enzyme in infarct LV tissue compared to sham animals, and was significantly reduced in Dz treated animals. Gene expression was evaluated by qRT-PCR using the quantitative standard curve method, and the results were normalized to GAPDH levels and reported as fold changes in copy number of mRNA levels compared to sham animals (*p<0.05;**p<0.01;*** p<0.001 vs. MI; one-way ANOVA followed by Dunnett's Multiple Comparison post-test).

Systemic levels of these cytokines measured from plasma reflected the local gene expression patterns and exhibit a strong trend for Dz treatment mediating an anti-inflammatory effect (**Figure 3.9 a-c**). Moreover, the endogenous anti-inflammatory cytokine IL-10 did not show any statistically significant changes in local gene expression (**Figure 3.10**). In fact, it exhibited a trend of upregulation in plasma levels with Dz treatment (**Figure 3.9d**). Together, these effects result in a lower ratio of IL-12/IL-10 in

systemic circulation, which is a surrogate measure of anti-inflammatory response due to the apparent opposing relationship of these cytokines and positive implications in resolution of inflammation.[47]

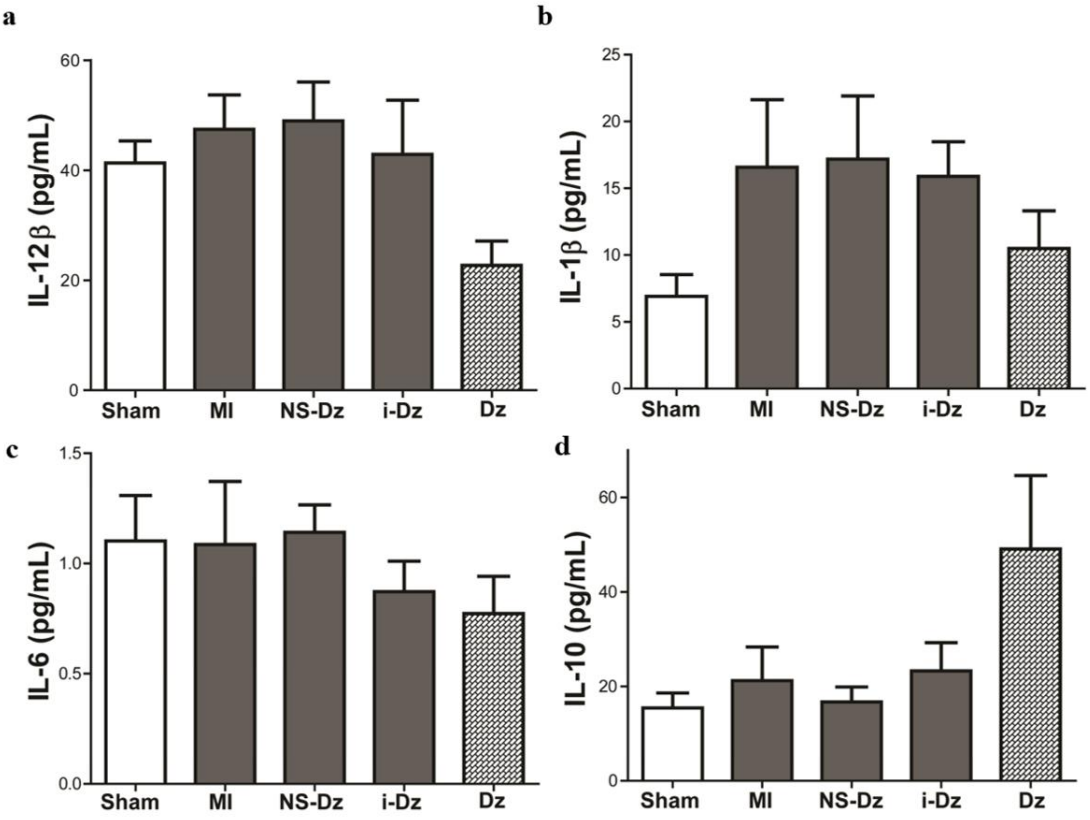

Figure 3.9. Grouped data (mean ± SEM; n=3-9 per group) from plasma at 3 days. Although there was no statistically significant differences in any of the groups, there were consistent trends towards downregulation of pro-inflammatory cytokines (**a**) IL-12β, (**b**) IL-1β, (**c**) IL-6 and potential trend towards an increase in anti-inflammatory cytokine (**d**) IL-10 in the plasma of Dz treatment groups. Data was analyzed using the Luminex Multiplex system and reported as plasma cytokine concentrations, quantitatively derived from standard curves of each cytokine.

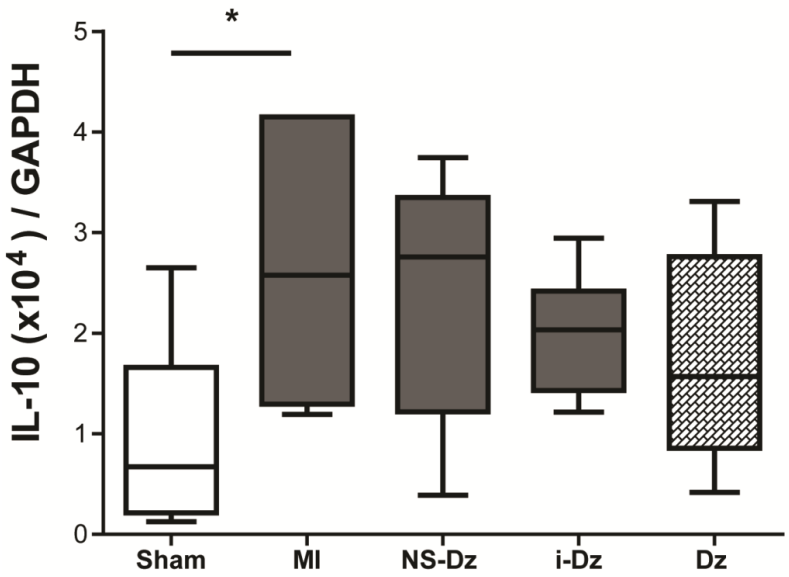

Figure 3.10. Grouped data (mean +/- SEM; n=5-9 per group) from LV infarct tissue at 3 days. A significant up-regulation of IL-10 expression was observed in animals that received an MI compared to sham, and no significant changes in IL-10 mRNA expression in any of the treatment groups. Gene expression was evaluated by qRT-PCR using the quantitative standard curve method and the results were normalized to GAPDH levels and reported as fold changes in copy number of mRNA levels compared to sham animals (*$p<0.05$;**$p<0.01$;*** $p<0.001$ vs. MI; one-way ANOVA followed by Dunnett's Multiple Comparison post-test).

3.3 *Conclusion*

Taken together, we demonstrate the first example of using catalytic Dz-AuNPs as an *in vivo* therapeutic. This likely represents the tip of iceberg, and given the broad range of therapeutic targets that have been proposed and tested for soluble DNAzymes, we expect that DNAzyme-AuNP conjugates to present an important and viable route for re-examining their efficacy in clinical settings. Specifically, this work shows potent gene silencing *in vivo* via catalytic DNA particles, and identifies significant anti-inflammatory effects brought about as a direct consequence of suppressing the pro-inflammatory cytokine TNFα in an acute MI setting. While this study shows promising acute functional improvement likely brought about by the anti-inflammatory effect of TNFα mRNA specific Dz treatment

at the initial inflammatory stage post-MI, follow up studies evaluating the chronic effects of this treatment on cardiac remodeling and chronic function are needed to determine whether repeated administrations are necessary to sustain the benefits of transient knockdown of TNFα. High concentrations of TNFα has been shown to contribute to structural alterations in the failing heart and often used as an indicator of CHF as described earlier. Therefore, TNFα gene regulation by DNAzyme-AuNPs merits further investigation beyond acute modulation. [12,14,16] Despite these limitations, this study presents a strong case for early anti-inflammatory intervention and the potential to revive TNFα blockade as a viable therapeutic avenue for the prevention of chronic heart failure.

3.4 Material and Methods

3.4.1 Oligonucleotide sequences

ID	**Sequence (5'-3')**
IL-6β	F: CAGAGTCATTCAGAGCAATAC R: CTTTCAAGATGAGTTGGATGG
IL-1β	F: TAAGCCAACAAGTGGTATTC R: AGGTATAGATTCTTCCCCTTG
IL-10	F: CCTGGTAGAAGTGATGCCCC R: TGCTCCACTGCCTTGCTTTT
IL-12β	F: AGACCCTGCCCATTGAACTG R: CAGGAGTCAGGGTACTCCCA
TNFα	F: TCTTCTGTCTACTGAACTTCG R: AAGATGATCTGAGTGTGAGG
GAPDH	F: CCAGCCCAGCAAGGATACTG R: GGCCCCTCCTGTTGTTATGG
Dz	mGmUmGmCTCAGGCTAGCTACAACGAGGTmGmUmCmCCCT$_8$-SH
i-Dz	mGmUmGmCTCAAGCTAGCTACAACGAGGTmGmUmCmCCCT$_8$-SH

NS-Dz	mGmAmCmGCGAGGCTAGCTACAACGACAAmGmCmGmCCCT$_8$-SH
Cy5-NS-Dz	Cy5- mGmAmCmGCGAGGCTAGCTACAACGACAAmGmCmGmCCCT$_8$-SH
Dz(10/7)	mGmUmGmCTCAGGCTAGCTACAACGAGGTGTCmCmUmUmUT$_8$mUmU-SH
i-Dz(10/7)	mGmUmGmCTCAAGCTAGCTACAACGAGGTGTCmCmUmUmUT$_8$mUmU-SH

Table 3.1. List of all the oligonucleotide sequences.

3.4.2 Gold nanoparticle synthesis

Citrate-stabilized gold nanoparticles (AuNP; 14±3 nm) were prepared using published procedures.[54] A 500 mL solution of 1 mM hydrogen tetrachloroaurate(III) trihydrate solution was brought to a vigorous boil, and once boiling, 50 mL of a 38.8 mM sodium citrate tribasic dihydrate solution was added and allowed to reflux for 15 min. The reaction mixture was filtered using a 0.45 μm acetate filter, producing monodisperse AuNPs. The surface plasmon resonance wavelength of the gold nanoparticles was determined using UV-vis absorbance spectrometry, and particle size was determined using transmission electron microscopy (TEM).

3.4.3 DzNP synthesis

Disulfide-modified oligonucleotides at the 3’ terminus were purchased from Integrated DNA Technologies (IDT). The disulfide was reduced to a free thiol by incubating 50 nmols of lyophilized oligonucleotide with 1.0 mL of disulfide cleavage buffer (0.1 M dithiothreitol (DTT), 170 mM phosphate buffer at pH 8.0) for 3 hours at room temperature. The reduced oligonucleotides were purified using a NAP-25 column (GE Healthcare, Piscataway, NJ) with Nanopure water as the eluent. Subsequently, 40 nmol of DNA was

added to 10 mL of 14 nm gold nanoparticles (10 nM), bringing the final concentration of oligonucleotide and gold nanoparticles to ~3.0 μM and ~7.0 nM, respectively. The pH of the solution was adjusted to pH 7.4 by adding 1/10th the total volume (~133 μL) of 100 mM phosphate buffer, thus bringing the phosphate buffer concentration to 9 mM. The particles were stabilized by adding sodium dodecyl sulfate (SDS) to the solution and bringing the SDS concentration to 0.1% (g/mL) by using a stock solution of 10% SDS. The particles were successively salted with eight NaCl additions that were spaced 20 min apart using a stock solution of 2.0 M NaCl and 10 mM phosphate buffer. The final NaCl concentration of the DNA AuNP solution was increased to 0.7 M. The first two NaCl additions increased the concentration by 0.05 M increments, while the remaining six NaCl additions increased the NaCl concentration by 0.1 M increments. The particles were immediately sonicated for 10 s after each salt addition to maximize DNA packing, as indicated in literature.[55] Fully salted particles were then incubated overnight, in the dark at room temperature. We found that the 10-23 active catalytic core of the DNAzyme had a tendency to drive the formation of nanoparticle aggregates at 0.7 M NaCl due to partial self-complementarity of sequences. The formation of these aggregates did not result in any observable reduction in the quality of the particles (as measured by UV-vis absorbance, TEM, DNA density, and ultimately TNF□□ knockdown). The particles were stored as a stock solution (under high salt and excess DNA) at 4℃ until needed, for a maximum duration of 1 month. Note that Dz-conjugated particles that were washed and stored in Nanopure water for more than one week displayed a decrease in their gene-regulation activity, **Figure 3.11** (no salt or excess DNA). Therefore, particles only washed prior to

knockdown studies, where particles were centrifuged down four times at 13,500 rpm, filtered using a 0.2 µm filter, and reconstituted in PBS.

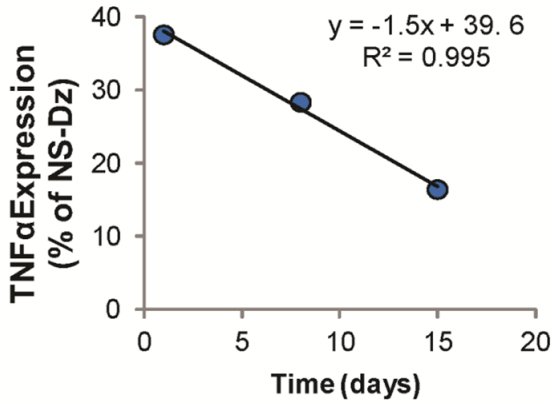

Figure 3.11. A plot showing Dz (7/7 b.p. recogntion arms) mediated *in vitro* TNFα knockdown in primary macrophages for cells treated with particles that were stored in Nanopure water for varied amounts of time (*t*= 1d, 8d, and 15d). Cells were treated with 10 nM particle concentration for 20 h. TNFα expression was measured by ELISA and the results were normalized to NS-Dz treated cells and reported as percent TNFα expression. Approximately 1.5% decrease in particle activity per day was observed due to instability of the particles stored in Nanopure water. For *in vitro* and *in vivo* studies, freshly modified particles were used and were stored in the reaction solution (*excess DNA and high salt concentration*) rather than Nanopure water.

3.4.4 Quantification of DNAzyme loading density on gold nanoparticles

The commercial Quant-iT^{TM} OliGreen® ssDNA kit was used to determine the total DNAzyme density per particle. The Quant-iT^{TM} OliGreen® ssDNA kit required preparation of a calibration curve by diluting a DNA stock solution (4 µg/mL) composed of the same thiolated oligonucleotide used during particle functionalization to 0.1, 0.2, 0.5, 0.75, 1.0, and 2.0 µg/mL at a final volume of 100 µL in 1x TE buffer. DNAzyme particle solutions were prepared by diluting a ~10 nM stock solution to 0.4, 0.6, and 0.8 nM with TE buffer. The oligonucleotides were then released from the particle by oxidizing/dissolving the gold with potassium cyanide (KCN). This was performed by adding 1 µL of a 5 M stock solution of KCN to each well, including the calibration wells

to ensure an accurate calibration curve and blank subtraction. The samples were incubated with KCN for 30 min to ensure complete dissolution. After complete dissolution of the gold nanoparticles, 100 μL of the freshly prepared 1x Quant-iT^{TM} OliGreen® solution was added to each well and fluorescence intensities (485/528 nm excitation/emission) of each well were then measured using a Bio-Tek Synergy HT plate reader to determine the total DNA density.

3.4.5 Cell culture

RAW 264.7 macrophages obtained from American Type Culture Collection (ATCC number: TIB-71) were maintained at 37°C under a humidified atmosphere of 5% CO_2 in Dulbecco's Modified Eagle's Medium (DMEM) containing 10% (v/v) fetal bovine serum (FBS), supplemented with penicillin (100 U/mL) and streptomycin (100 mg/mL) and 2 mM L-Glutamine. For primary macrophage culture, peritoneal macrophages were isolated from Sprague Dawley rats as described previously [56]. Briefly, cold PBS was infused into the peritoneal cavity of rats and cellular lavage was collected, spun down at 1000 x g at 4°C for 10 minutes, following which cell solution was resuspended in media described above. The cell solution was plated in 24-well plates ($3x10^6$ cells/well) and left to adhere overnight for treatment the following day. Primary single ventricular myocytes culture from Sprague Dawley rat hearts is described in supporting information.

3.4.6 DzNP uptake in macrophages and myocytes

To confirm the intracellular distribution of DNA delivered by DNA modified gold nanoparticles, RAW264.7 macrophages or adult rat cardiomyocytes were treated with Cy5 labeled DNAzyme functionalized gold particles for 1 hour (5 nM particle concentration

equivalent to 666.7 nM DNA concentration) and then washed in PBS three times, fixed in 4% PFA and stained with DAPI for nuclei and calcein for macrophages or FITC Maleimide for cardiomycocytes to delineate the cell surface, and imaged using laser scanning confocal microscopy (Zeiss LSM 510 META) to identify Cy5 fluorescence within the cells to indicate internalization of Cy5-DNA modified gold particles. Further, particle uptake was compared with commercially available Lipofectamine® RNAiMAX reagent (Life Technologies) mediated transfection at 1, 4, 18 and 24 hours using fluorescence microscopy in live cells for macrophages, and in fixed cells at 18 hours for cardiomyocytes.

3.4.7 In vitro silencing of TNFα with DzNPs

For TNFα knockdown studies, peritoneal macrophages were treated with three types of particles, active (Dz), inactive (i-Dz) or active but nonspecific (NS-Dz) at a particle concentration of 10 nM/well (1.3 □M DNA). After 20 hours of treatment, the media was removed and the cells were re-treated with the same concentration of particles while at the same time receiving stimulation with LPS (5 ng/ml) to induce TNFα production. After 4 hours of stimulation, 100 uL of media was collected from each sample and analyzed for secreted TNFα via ELISA according to the manufacture's protocol (eBioscience).

3.4.8 DzNP in vitro cytotoxicity

Cytotoxicity of DNAzyme particles was compared with a commercially available, commonly used transfection reagent, using pro-inflammatory cytokine TNFα itself as a surrogate cytotoxicity indicator. Primary peritoneal macrophages were transfected with either Lipofectamine® RNAiMAX containing scrambled DNA or NS-Dz for 20 hours, and stimulated with LPS (5 ng/mL) for 4 hours to induce TNFα production. Extracellular medium was collected and TNFα production quantified by ELISA.

3.4.9 Myocardial infarction and particle injection

A randomized and blinded study was conducted using adult Sprague Dawley rats. The animals were assigned to treatment groups (n=6-9) using a random number generator and the animal surgeon was only given letter codes to identify groups. While one group was subjected to a sham surgery, the other four groups received myocardial infarction via permanent ligation of the left descending artery. Briefly, the animals were anesthetized (1-3% isoflurane) and following tracheal intubation, the heart was exposed by separating the ribs. Myocardial infarction was performed by ligation of the left anterior descending coronary artery. For groups receiving particle injections, immediately after coronary artery ligation, 100 µL of one of the following DNAzyme modified particles were injected into the cyanotic ischemic zone (3 locations) through a 25-gauge needle while the heart was beating: Dz, i-Dz or NS-Dz. The dose of DNAzyme injected was 0.07 mg/kg (100 nM particle concentration). Following injection, the chests were closed and animals were allowed to recover on a heating pad until functional assessments were made 3 days following MI surgery using echocardiography (Acuson Sequoia 512 with a 14 MHz transducer) and invasive pressure-volume hemodynamics (Millar Instruments). These studies conformed to the *Guide for the Care and Use of Laboratory Animals* published by the US National Institutes of Health (NIH Publication No. 85-23, revised 1996) and all animal studies were approved by Emory University Institutional Animal Care and Use Committee.

3.4.10 In vivo imaging

Rats were subjected to MI as described above and Cy5 labeled NS-Dz gold particle conjugates were injected in 3 areas in the border zone surrounding the infarct. Rats were

sacrificed and the hearts, liver, spleen and kidneys were harvested and imaged on days 0, 1, 2, and 3 post-injection (n=1 per time point) using Bruker In-Vivo Xtreme. The Cy5 fluorescent intensity in these organs was plotted as arbitrary fluorescence over time to demonstrate retention of the particles up to 3 days in the heart.

3.4.11 Echocardiography and invasive pressure-volume hemodynamics analysis

In a separate study, rats were subjected to MI surgery and injections as described above, and 3 days post-surgeries and treatment anesthetized rats were subjected to echocardiography (Acuson sequoia 512) and invasive pressure-volume hemodynamics (Millar MPVS instruments) analyses to assess the functional effects of treatment. From echocardiography, short axis values of left ventricular end systolic (ES) and end diastolic (ED) dimensions were obtained. An average of 3 consecutive cardiac cycles was used for each measurement and was performed three times in by a blinded investigator. Fractional shortening was calculated as [(end-diastolic diameter – end-systolic diameter)/(end-diastolic diameter)] and expressed as a percentage. For invasive hemodynamics, the pressure-volume probe was inserted into the left ventricle. After stabilization, baseline left ventricular pressure-volume loops were recorded for at least 10 cardiac cycles and data averaged to get mean values for each animal. Data extracted include +dP/dT, -dP/dT and left-ventricular Ejection Fraction (%EF).

3.4.12 In vivo gene expression and plasma cytokine analysis

Following functional measurements at 3 days, animals were sacrificed and the left ventricle infarct tissue was harvested and homogenized, which the total RNA contents were isolated using Trizol (Invitrogen) according to the manufacturer's protocol. Complementary DNA (cDNA) was synthesized using SuperScript III kit (Invitrogen) and

the quantitative real-time PCR (qRT-PCR) was performed using Power SYBR Green (Invitrogen) master mix with Applied Biosystems StepOnePlus^{TM} real time PCR system. Absolute quantification method was employed to analyze gene expression levels of each of the target genes. Standard curves for each of the primer sets (**Table 3.1**) were constructed with serial dilutions of input DNA templates and validated comparable amplification efficiencies (curve slopes: −3.32 to −3.64). Relative mRNA levels were obtained by extrapolation of Ct values from the slopes of the standard curve for each primer set. Gene expression levels were then normalized to the endogenous housekeeping gene GAPDH and further, expressed as fold changes compared to expression levels in sham animals in order to minimize batch-to-batch variability in tissue processing. Prior to sacrificing the animals, blood was collected via cardiac puncture, plasma separated from blood cells and stored in -70^{0}C until cytokine analysis using the Luminex multiplex analyzer system (Luminex LX100). A custom cytokine bead panel from ebioscience was used to analyze cytokines IL-12β, IL-1β, IL-6 and IL-10 in the plasma.

3.4.13 Statistics

All statistical analyses were performed using Graphpad Prism 5 software. Quantitative results were presented as means ± SEM. Statistical comparisons were performed by one way analysis of variance (ANOVA) followed by the appropriate post-test as described in the figure legends. P values of less than 0.05 were considered significant.

3.5 References

(1) Go, A. S.; Mozaffarian, D.; Roger, V. L.; Benjamin, E. J.; Berry, J. D.; Blaha, M. J.; Dai, S.; Ford, E. S.; Fox, C. S.; Franco, S.; Fullerton, H. J.; Gillespie, C.; Hailpern, S.

M.; Heit, J. A.; Howard, V. J.; Huffman, M. D.; Judd, S. E.; Kissela, B. M.; Kittner, S. J.; Lackland, D. T.; Lichtman, J. H.; Lisabeth, L. D.; Mackey, R. H.; Magid, D. J.; Marcus, G. M.; Marelli, A.; Matchar, D. B.; McGuire, D. K.; Mohler, E. R., 3rd; Moy, C. S.; Mussolino, M. E.; Neumar, R. W.; Nichol, G.; Pandey, D. K.; Paynter, N. P.; Reeves, M. J.; Sorlie, P. D.; Stein, J.; Towfighi, A.; Turan, T. N.; Virani, S. S.; Wong, N. D.; Woo, D.; Turner, M. B.; American Heart Association Statistics, C.; Stroke Statistics, S. Heart disease and stroke statistics--2014 update: a report from the American Heart Association. *Circulation* **2014**, *129*, e28.

(2) Wang, F.; Stouffer, G. A.; Waxman, S.; Uretsky, B. F. Late coronary stent thrombosis: early vs. late stent thrombosis in the stent era. *Catheterization and cardiovascular interventions : official journal of the Society for Cardiac Angiography & Interventions* **2002**, *55*, 142.

(3) Yellon, D. M.; Hausenloy, D. J. Myocardial reperfusion injury. *N Engl J Med* **2007**, *357*, 1121.

(4) Kereiakes, D. J. Adjunctive pharmacotherapy before percutaneous coronary intervention in non-ST-elevation acute coronary syndromes: the role of modulating inflammation. *Circulation* **2003**, *108*, III22.

(5) Nahrendorf, M.; Swirski, F. K.; Aikawa, E.; Stangenberg, L.; Wurdinger, T.; Figueiredo, J. L.; Libby, P.; Weissleder, R.; Pittet, M. J. The healing myocardium sequentially mobilizes two monocyte subsets with divergent and complementary functions. *J Exp Med* **2007**, *204*, 3037.

(6) Swirski, F. K.; Nahrendorf, M.; Etzrodt, M.; Wildgruber, M.; Cortez-Retamozo, V.; Panizzi, P.; Figueiredo, J. L.; Kohler, R. H.; Chudnovskiy, A.; Waterman, P.; Aikawa,

E.; Mempel, T. R.; Libby, P.; Weissleder, R.; Pittet, M. J. Identification of splenic reservoir monocytes and their deployment to inflammatory sites. *Science* **2009**, *325*, 612.

(7) Frangogiannis, N. G.; Smith, C. W.; Entman, M. L. The inflammatory response in myocardial infarction. *Cardiovasc Res* **2002**, *53*, 31.

(8) Troidl, C.; Mollmann, H.; Nef, H.; Masseli, F.; Voss, S.; Szardien, S.; Willmer, M.; Rolf, A.; Rixe, J.; Troidl, K.; Kostin, S.; Hamm, C.; Elsasser, A. Classically and alternatively activated macrophages contribute to tissue remodelling after myocardial infarction. *Journal of cellular and molecular medicine* **2009**, *13*, 3485.

(9) Bonvini, R. F. Inflammatory response post-myocardial infarction and reperfusion: a new therapeutic target? *Eur Heart J Suppl* **2005**, *7*, I27.

(10) Frangogiannis, N. G. Targeting the inflammatory response in healing myocardial infarcts. *Current medicinal chemistry* **2006**, *13*, 1877.

(11) Kempf, T.; Zarbock, A.; Vestweber, D.; Wollert, K. C. Anti-inflammatory mechanisms and therapeutic opportunities in myocardial infarct healing. *J Mol Med (Berl)* **2012**, *90*, 361.

(12) Nian, M.; Lee, P.; Khaper, N.; Liu, P. Inflammatory cytokines and postmyocardial infarction remodeling. *Circ Res* **2004**, *94*, 1543.

(13) Bozkurt, B.; Kribbs, S. B.; Clubb, F. J., Jr.; Michael, L. H.; Didenko, V. V.; Hornsby, P. J.; Seta, Y.; Oral, H.; Spinale, F. G.; Mann, D. L. Pathophysiologically relevant concentrations of tumor necrosis factor-alpha promote progressive left ventricular dysfunction and remodeling in rats. *Circulation* **1998**, *97*, 1382.

(14) Kleinbongard, P.; Schulz, R.; Heusch, G. TNFalpha in myocardial ischemia/reperfusion, remodeling and heart failure. *Heart Fail Rev* **2011**, *16*, 49.

(15) Pagani, F. D.; Baker, L. S.; Hsi, C.; Knox, M.; Fink, M. P.; Visner, M. S. Left ventricular systolic and diastolic dysfunction after infusion of tumor necrosis factor-alpha in conscious dogs. *The Journal of clinical investigation* **1992**, *90*, 389.

(16) Sack, M. Tumor necrosis factor-alpha in cardiovascular biology and the potential role for anti-tumor necrosis factor-alpha therapy in heart disease. *Pharmacol Ther* **2002**, *94*, 123.

(17) Sivasubramanian, N.; Coker, M. L.; Kurrelmeyer, K. M.; MacLellan, W. R.; DeMayo, F. J.; Spinale, F. G.; Mann, D. L. Left ventricular remodeling in transgenic mice with cardiac restricted overexpression of tumor necrosis factor. *Circulation* **2001**, *104*, 826.

(18) Levine, B.; Kalman, J.; Mayer, L.; Fillit, H. M.; Packer, M. Elevated circulating levels of tumor necrosis factor in severe chronic heart failure. *N Engl J Med* **1990**, *323*, 236.

(19) Irwin, M. W.; Mak, S.; Mann, D. L.; Qu, R.; Penninger, J. M.; Yan, a.; Dawood, F.; Wen, W. H.; Shou, Z.; Liu, P. Tissue expression and immunolocalization of tumor necrosis factor-alpha in postinfarction dysfunctional myocardium. *Circulation* **1999**, *99*, 1492.

(20) Jacobs, M.; Staufenberger, S.; Gergs, U.; Meuter, K.; Brandstatter, K.; Hafner, M.; Ertl, G.; Schorb, W. Tumor necrosis factor-alpha at acute myocardial infarction in rats and effects on cardiac fibroblasts. *J Mol Cell Cardiol* **1999**, *31*, 1949.

(21) Kurrelmeyer, K. M.; Michael, L. H.; Baumgarten, G.; Taffet, G. E.; Peschon, J. J.; Sivasubramanian, N.; Entman, M. L.; Mann, D. L. Endogenous tumor necrosis factor protects the adult cardiac myocyte against ischemic-induced apoptosis in a murine model of acute myocardial infarction. *Proc Natl Acad Sci U S A* **2000**, *97*, 5456.

(22) Anker, S. D.; Coats, A. J. How to RECOVER from RENAISSANCE? The significance of the results of RECOVER, RENAISSANCE, RENEWAL and ATTACH. *Int J Cardiol* **2002**, *86*, 123.

(23) Bozkurt, B.; Torre-Amione, G.; Warren, M. S.; Whitmore, J.; Soran, O. Z.; Feldman, A. M.; Mann, D. L. Results of targeted anti-tumor necrosis factor therapy with etanercept (ENBREL) in patients with advanced heart failure. *Circulation* **2001**, *103*, 1044.

(24) Nahrendorf, M.; Pittet, M. J.; Swirski, F. K. Monocytes: protagonists of infarct inflammation and repair after myocardial infarction. *Circulation* **2010**, *121*, 2437.

(25) Bhindi, R.; Khachigian, L. M.; Lowe, H. C. DNAzymes targeting the transcription factor Egr-1 reduce myocardial infarct size following ischemia-reperfusion in rats. *J Thromb Haemost* **2006**, *4*, 1479.

(26) Iversen, P. O.; Nicolaysen, G.; Sioud, M. DNA enzyme targeting TNF-alpha mRNA improves hemodynamic performance in rats with postinfarction heart failure. *Am J Physiol Heart Circ Physiol* **2001**, *281*, H2211.

(27) Luo, X.; Cai, H.; Ni, J.; Bhindi, R.; Lowe, H. C.; Chesterman, C. N.; Khachigian, L. M. c-Jun DNAzymes inhibit myocardial inflammation, ROS generation, infarct size, and improve cardiac function after ischemia-reperfusion injury. *Arterioscler Thromb Vasc Biol* **2009**, *29*, 1836.

(28) Xiang, G.; Schuster, M. D.; Seki, T.; Witkowski, P.; Eshghi, S.; Itescu, S. Downregulated expression of plasminogen activator inhibitor-1 augments myocardial neovascularization and reduces cardiomyocyte apoptosis after acute myocardial infarction. *J Am Coll Cardiol* **2005**, *46*, 536.

(29) Zhang, L.; Gasper, W. J.; Stass, S. A.; Ioffe, O. B.; Davis, M. A.; Mixson, A. J. Angiogenic inhibition mediated by a DNAzyme that targets vascular endothelial growth factor receptor 2. *Cancer Res* **2002**, *62*, 5463.

(30) Yang, L.; Xu, Z.; Liu, L.; Luo, X.; Lu, J.; Sun, L.; Cao, Y. Targeting EBV-LMP1 DNAzyme enhances radiosensitivity of nasopharyngeal carcinoma cells by inhibiting telomerase activity. *Cancer biology & therapy* **2014**, *15*, 61.

(31) Gilleron, J.; Querbes, W.; Zeigerer, A.; Borodovsky, A.; Marsico, G.; Schubert, U.; Manygoats, K.; Seifert, S.; Andree, C.; Stoter, M.; Epstein-Barash, H.; Zhang, L.; Koteliansky, V.; Fitzgerald, K.; Fava, E.; Bickle, M.; Kalaidzidis, Y.; Akinc, A.; Maier, M.; Zerial, M. Image-based analysis of lipid nanoparticle-mediated siRNA delivery, intracellular trafficking and endosomal escape. *Nat Biotechnol* **2013**, *31*, 638.

(32) Czech, B.; Hannon, G. J. Small RNA sorting: matchmaking for Argonautes. *Nature reviews. Genetics* **2011**, *12*, 19.

(33) Lv, H.; Zhang, S.; Wang, B.; Cui, S.; Yan, J. Toxicity of cationic lipids and cationic polymers in gene delivery. *J Control Release* **2006**, *114*, 100.

(34) Rosi, N. L.; Giljohann, D. A.; Thaxton, C. S.; Lytton-Jean, A. K.; Han, M. S.; Mirkin, C. A. Oligonucleotide-modified gold nanoparticles for intracellular gene regulation. *Science* **2006**, *312*, 1027.

(35) Cutler, J. I.; Auyeung, E.; Mirkin, C. A. Spherical nucleic acids. *J Am Chem Soc* **2012**, *134*, 1376.

(36) Choi, C. H.; Hao, L.; Narayan, S. P.; Auyeung, E.; Mirkin, C. A. Mechanism for the endocytosis of spherical nucleic acid nanoparticle conjugates. *Proc Natl Acad Sci U S A* **2013**, *110*, 7625.

(37) Zheng, D.; Giljohann, D. A.; Chen, D. L.; Massich, M. D.; Wang, X. Q.; Iordanov, H.; Mirkin, C. A.; Paller, A. S. Topical delivery of siRNA-based spherical nucleic acid nanoparticle conjugates for gene regulation. *Proc Natl Acad Sci U S A* **2012**, *109*, 11975.

(38) Jensen, S. A.; Day, E. S.; Ko, C. H.; Hurley, L. A.; Luciano, J. P.; Kouri, F. M.; Merkel, T. J.; Luthi, A. J.; Patel, P. C.; Cutler, J. I.; Daniel, W. L.; Scott, A. W.; Rotz, M. W.; Meade, T. J.; Giljohann, D. A.; Mirkin, C. A.; Stegh, A. H. Spherical nucleic acid nanoparticle conjugates as an RNAi-based therapy for glioblastoma. *Sci Transl Med* **2013**, *5*, 209ra152.

(39) Yehl, K.; Joshi, J. P.; Greene, B. L.; Dyer, R. B.; Nahta, R.; Salaita, K. Catalytic deoxyribozyme-modified nanoparticles for RNAi-independent gene regulation. *ACS Nano* **2012**, *6*, 9150.

(40) de Fougerolles, A.; Vornlocher, H. P.; Maraganore, J.; Lieberman, J. Interfering with disease: a progress report on siRNA-based therapeutics. *Nat Rev Drug Discov* **2007**, *6*, 443.

(41) Champion, J. A.; Walker, A.; Mitragotri, S. Role of particle size in phagocytosis of polymeric microspheres. *Pharm Res* **2008**, *25*, 1815.

(42) Hastings, C. L.; Roche, E. T.; Ruiz-Hernandez, E.; Schenke-Layland, K.; Walsh, C. J.; Duffy, G. P. Drug and cell delivery for cardiac regeneration. *Adv Drug Deliv Rev* **2014**.

(43) Kumar, A.; Thota, V.; Dee, L.; Olson, J.; Uretz, E.; Parrillo, J. E. Tumor necrosis factor alpha and interleukin 1beta are responsible for in vitro myocardial cell depression induced by human septic shock serum. *J Exp Med* **1996**, *183*, 949.

(44) Ono, K.; Matsumori, A.; Shioi, T.; Furukawa, Y.; Sasayama, S. Cytokine gene expression after myocardial infarction in rat hearts: possible implication in left ventricular remodeling. *Circulation* **1998**, *98*, 149.

(45) Moe, G. W.; Marin-Garcia, J.; Konig, A.; Goldenthal, M.; Lu, X.; Feng, Q. In vivo TNF-alpha inhibition ameliorates cardiac mitochondrial dysfunction, oxidative stress, and apoptosis in experimental heart failure. *Am J Physiol Heart Circ Physiol* **2004**, *287*, H1813.

(46) Habib, F. M.; Springall, D. R.; Davies, G. J.; Oakley, C. M.; Yacoub, M. H.; Polak, J. M. Tumour necrosis factor and inducible nitric oxide synthase in dilated cardiomyopathy. *Lancet* **1996**, *347*, 1151.

(47) Watson, D. C.; Sargianou, M.; Panos, G. Interleukin-12 (IL-12)/IL-10 ratio as a marker of disease severity in Crimean-Congo hemorrhagic fever. *Clinical and vaccine immunology : CVI* **2012**, *19*, 823.

(48) Yokoyama, T.; Vaca, L.; Rossen, R. D.; Durante, W.; Hazarika, P.; Mann, D. L. Cellular basis for the negative inotropic effects of tumor necrosis factor-alpha in the adult mammalian heart. *The Journal of clinical investigation* **1993**, *92*, 2303.

(49) Gulick, T.; Chung, M. K.; Pieper, S. J.; Lange, L. G.; Schreiner, G. F. Interleukin 1 and tumor necrosis factor inhibit cardiac myocyte beta-adrenergic responsiveness. *Proc Natl Acad Sci U S A* **1989**, *86*, 6753.

(50) Mazurek, S. R.; Bovo, E.; Zima, A. V. Regulation of sarcoplasmic reticulum Ca(2+) release by cytosolic glutathione in rabbit ventricular myocytes. *Free Radic Biol Med* **2014**, *68*, 159.

(51) Zima, A. V.; Blatter, L. A. Redox regulation of cardiac calcium channels and transporters. *Cardiovasc Res* **2006**, *71*, 310.

(52) Finkel, M. S.; Oddis, C. V.; Jacob, T. D.; Watkins, S. C.; Hattler, B. G.; Simmons, R. L. Negative inotropic effects of cytokines on the heart mediated by nitric oxide. *Science* **1992**, *257*, 387.

(53) Song, W.; Lu, X.; Feng, Q. Tumor necrosis factor-alpha induces apoptosis via inducible nitric oxide synthase in neonatal mouse cardiomyocytes. *Cardiovasc Res* **2000**, *45*, 595.

(54) Hill, H. D.; Mirkin, C. A. The bio-barcode assay for the detection of protein and nucleic acid targets using DTT-induced ligand exchange. *Nat Protoc* **2006**, *1*, 324.

(55) Hurst, S. J.; Lytton-Jean, A. K.; Mirkin, C. A. Maximizing DNA loading on a range of gold nanoparticle sizes. *Analytical chemistry* **2006**, *78*, 8313.

(56) Wang, G. W.; Guo, Y.; Vondriska, T. M.; Zhang, J.; Zhang, S.; Tsai, L. L.; Zong, N. C.; Bolli, R.; Bhatnagar, A.; Prabhu, S. D. Acrolein consumption exacerbates myocardial ischemic injury and blocks nitric oxide-induced PKCepsilon signaling and cardioprotection. *J Mol Cell Cardiol* **2008**, *44*, 1016.

Chapter 4: Rolling DNA-based motors with superdiffusive transport powered by RNase H

4.1 Introduction

Inspired by biological motors, a number of synthetic motors have been developed as model systems employing a wide range of chemical reactions.[1-6] DNA-based machines that walk along a track have shown the greatest promise in recapitulating the properties of biological motor proteins.[1,7-14] However, the maximum distance traveled by the most processive DNA-based motors is ~1 μm.[8,9,12] The velocity of these walkers is also limited to rates of ~1 nm/min due to a fundamental trade-off between motor endurance and speed. The problem is that DNA-walkers tend to spontaneously dissociate off their tracks, and while increasing motor multivalency improves track affinity and motor endurance (the mean distance travelled), this leads to a significant decrease in motor velocity. For example, increasing the multivalency of a DNAzyme-based motor from two anchors to six led to complete abrogation of motor transport.[15]

Yet, in order for DNA based machines to transition beyond being an elegant model system for motor proteins and truly achieve their potential, both motor efficiency and velocity need to be enhanced by orders of magnitude. In addition, the sophisticated instrumentation currently required to observe DNA walkers needs to be greatly simplified to render DNA machines as useful. To overcome these challenges, we designed a highly multivalent motor that moves through a cog-and-wheel mechanism, allowing μm or nm sized particles to roll rather than walk. Rolling represents a fundamentally distinct type of movement that overcomes the documented tradeoffs inherent to multivalent molecular motors.[15,16] In principle, this is because rolling reduces the DNA motor footprint, reducing unproductive sampling interactions, and thus increasing velocity.

The motor described herein consists of a DNA-coated spherical particle (5 μm or 0.5 μm diameter particles) that hybridizes to a surface modified with complementary RNA. The particle moves upon addition of RNase H, which selectively hydrolyzes hybridized RNA but not single stranded RNA (**Figure 4.1**). Since the driving force for movement is derived from the free energy of binding new single stranded RNA that biases Brownian motion away from consumed substrate (**Figure 4.1a**), this type of motion is often described as a "burnt-bridge Brownian ratchet". Note that the molecular walkers also employ a burnt bridge mechanism, where oligonucleotide hybridization is followed by DNAzyme/endonuclease hydrolysis of the fuel strand. The main difference between the molecular walkers and the system studied here is the massive multivalency of the DNA coated particles – molecular walkers typically employ 2-6 anchor points while our particle-based motor employs thousands of anchoring strands. This equates to 100-1,000 fold greater contact area or 10-100 fold greater contact diameter with the surface when compared to molecular spiders. Hence, the micron sized length scale of the particle significantly increases the number of contacts with the surface, which should lead to collective and emergent properties not expected for DNA-based walkers. Importantly, we expected that our particles would overcome the diminished velocities due to high multivalency, as is predicted by theory, because the RNase H hydrolysis rate is approximately two orders of magnitude greater than that of DNAzymes and endonucleases.[14,17,18] Moreover, highly multivalent motors are expected to display greater processivity, thus potentially addressing a major limitation of DNA walkers. Finally, the spherical particle template allows for the potential to roll, which is a fundamentally different mode for translocation for DNA based machines.

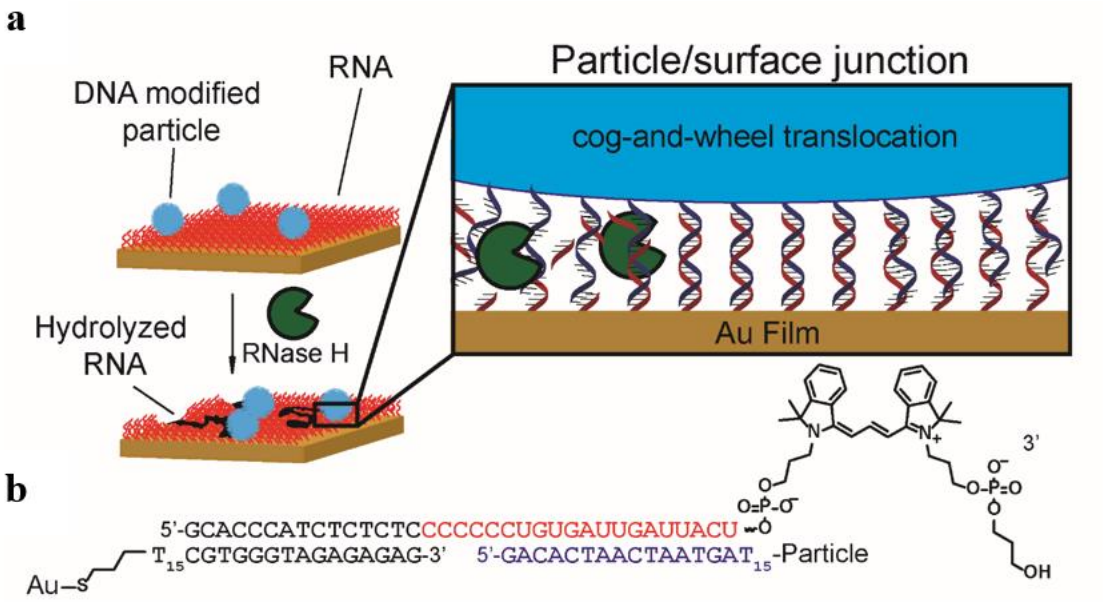

Figure 4.1. (**a**) DNA-modified particles were hybridized to an RNA monolayer presenting a complementary strand. Particles were immobile until RNase H was added, which selectively hydrolyzes RNA duplexed to DNA. (**b**) Schematic representation showing the hybridized oligonucleotide sequences at the particle-substrate junction. Note that there are hundreds of duplexes within this junction. RNA bases are shown in red, while the particle DNA bases are shown in blue.

4.2 Results and Discussion

4.2.1 Synthesis and stability of the RNA monolayer

To test whether a massively multivalent motor can move along a surface, we first generated an RNA-monolayer on a substrate by immobilizing a DNA anchor strand to a thin gold film and then hybridizing a fluorescently labeled RNA-DNA chimera strand to the surface. The Cy3 fluorescence label at the 3' RNA terminus was used to determine the optimal conditions to reach maximum RNA density and to detect RNA hydrolysis using fluorescence microscopy (**Figure 4.1b**). The optimal anchor strand concentration was determined by varying its concentration until a saturation in Cy3 labeled RNA fluorescence was observed upon surface hybridization (**Figure 4.2b**), which indirectly relates to RNA

density. A saturation in fluorescence was observed at concentrations equal to or greater than 1 μM (**Figure 4.2a**). In order to quantify the RNA density on the surface, RNA was released from the surface through RNase A addition and the resulting fluorescence measured using the fluorescence microscope. The resulting average fluorescence intensity was fitted to a calibration curve constructed by measuring the fluorescence of known amounts of Cy3 labeled RNA (**Figure 4.2c**). Under optimal conditions, we achieved a maximum RNA density of 60,000 molecules/μm^2, equivalent to an average molecular footprint of 20 ± 6 nm^2 per RNA strand (**Figure 4.2d)**. This RNA density was maintained for at least 4 hr in 1xPBS and 10 μM DTT, a thiol reducing agent necessary for maintaining RNase H activity (**Figure 4.2e**). In the absence of DTT, surfaces were stable for weeks in 1xPBS.

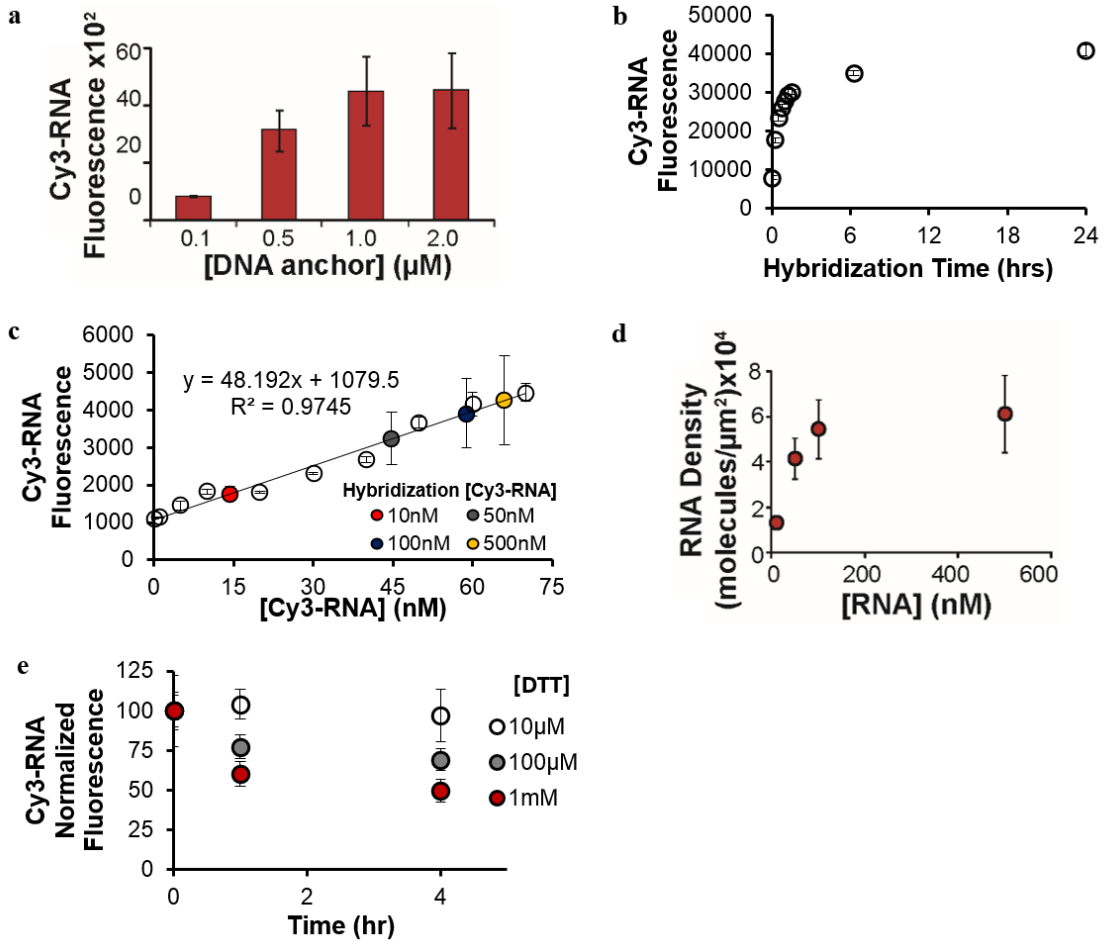

Figure 4.2. (**a**) Bar graph showing how the DNA anchor strand incubation concentration alters the Cy3-RNA fluorescence intensity which is directly proportional to the RNA surface density. Error bars represent the standard deviation in the average fluorescence intensity from at least 5 regions across each channel. (**b**) A representative kinetic plot of hybridization between 3'Cy3-RNA (100 nM) and surface immobilized DNA anchor strand in 1x PBS. Error bars represent the standard deviation in the average fluorescence intensity from at least 5 regions across each channel. (**c**) Fluorescence calibration curve for 3'Cy3-RNA measured using a fluorescence microscope (white circles). This calibration curve was fit using least squares regression analysis. The calibration curve was then used to quantify the concentration of released RNA through RNase A treatment from surfaces hybridized with varied concentrations of RNA 10 (red circle), 50 (green circle), 100 (blue circle), and 500 (yellow circle) nM RNA. (**d**) Plot showing the RNA surface density as a function of RNA concentration during Cy3-RNA hybridization with surface immobilized DNA anchor strand. The RNA density was maximized when RNA was hybridized at a concentration of at least 100 nM. Error bars represent the standard deviation in the average fluorescence intensity from at least 5 regions across each channel. (**e**) A kinetic plot showing the 3' Cy3-RNA fluorescence intensity as a function of DTT incubation time at concentrations of 10 μM (white), 100 μM (gray), and 1 mM (red) in 1xPBS. Error bars represent the standard deviation across at least 5 different regions from each micro-channel. Based on this analysis, we found that a 1 mM DTT solution led to ~50% loss of RNA after 4 hrs. Surfaces were stable for weeks in the absence of DTT in PBS.

4.2.2 Kinetic analysis of RNase H hydrolysis of surface immobilized RNA and the role of passivation

Given that particle motion is intimately connected with RNase H efficiency and enzyme rates vary when substrates are immobilized, we initially measured hydrolysis kinetics for a DNA-RNA duplex monolayer. We found that PEG passivation was critical, since RNase H was inhibited when the surface was incompletely passivated (**Figure 4.3**). Initially, when measuring the hydrolysis of surface immobilized RNA, we found that RNase H was completely inhibited. Since RNase H contains multiple cysteine residues, we first suspected that enzyme inhibition was due to irreversible binding of the enzyme to the Au surface. To prevent nonspecific binding, the Au surface was passivated with $SH(CH_2)_{11}(OCH_2CH_2)_6OCH_3$ (SH-PEG) because PEG is known to greatly reduce nonspecific interactions with surfaces. To test the assumption that RNase H inhibition was due to Au film binding, the DNA monolayer surface was backfilled with SH-PEG under a range of conditions, where the SH-PEG concentration and the passivation time was varied. It was determined that complete surface passivation occurred after 4 hrs of incubation with a 100 μM SH-PEG solution. This was inferred by observing a saturation in the loss of fluorescence of FAM labeled DNA anchor strand (**Figure 4.3b**). Next, RNase H hydrolysis of surface immobilized RNA duplexed with DNA was investigated under the various passivation conditions by measuring the loss in fluorescence of Cy3 labeled RNA throughout the channel over time (**Figure 4.3c-f**). When the channel was SH-PEG passivated for shorter durations (2 hrs), we observed that the fluorescence intensity varied significantly across the length of the well; regions near the port where RNase H was added had the lowest intensities, while regions furthest away from this site showed minimal

substrate hydrolysis (**Figure 4.3e top**). In contrast, channels that were blocked for 6 hrs showed homogeneous fluorescence intensities indicating uniform RNase H activity levels (**Figure 4.3e bottom**). The variation in substrate hydrolysis as a function of passivation time is shown in **figure 4.3f**.

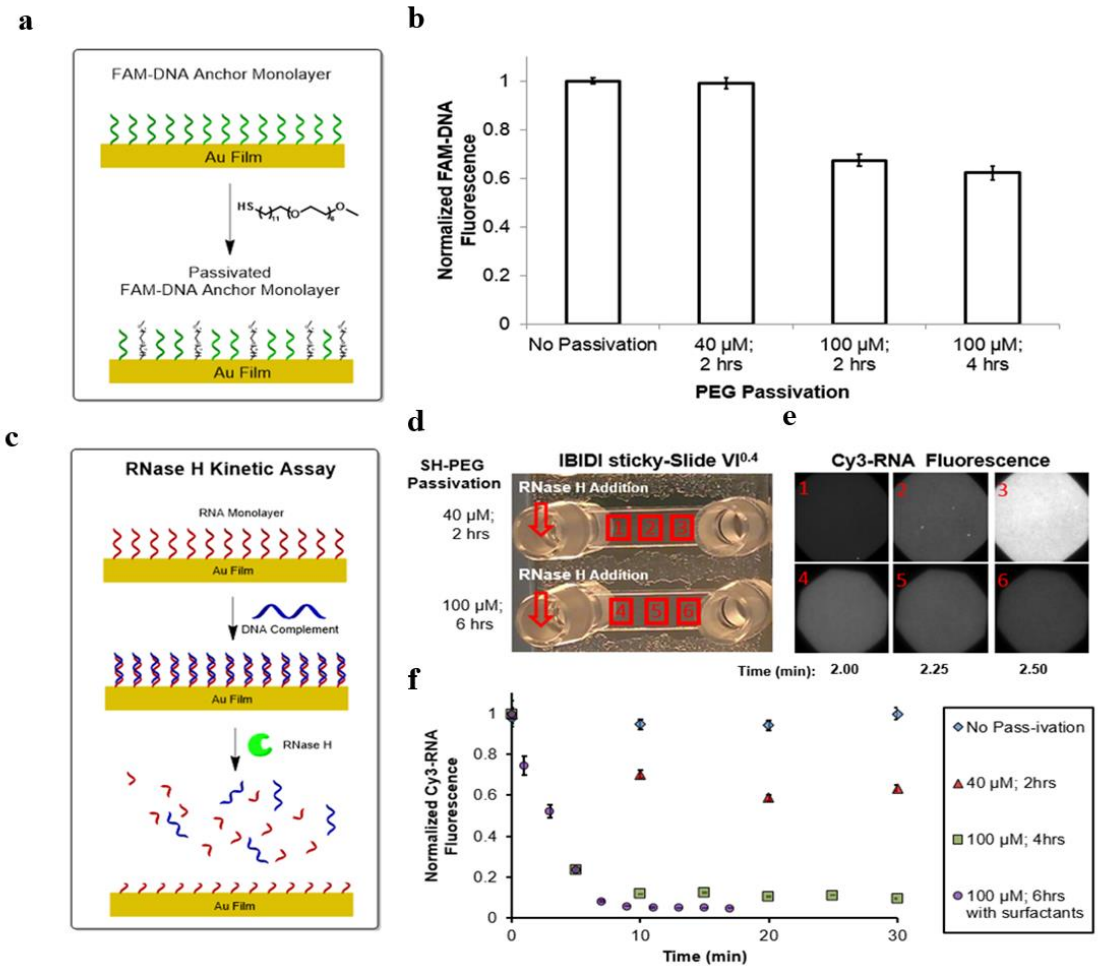

Figure 4.3. (**a**) Schematic showing surface passivation with a thiolated PEG. (**b**) Bar graph summarizing the loss in fluorescence of the FAM labeled DNA anchor strand upon incubating the gold surface with SH-PEG under various concentrations and incubation times. Error bars represent the standard deviation of five fluorescence measurements across the length of the micro-channel. (**c**) Schematic displaying the fluorescence assay used to measure RNase H activity. (**d**) A photograph of the micro-channel array substrate used throughout the current work. Arrows indicated the location of where Cy3 fluorescence was obtained in relation to the channel port where RNase H was introduced. (**e**) Representative Cy3 fluorescence images collected at different positions along the micro channel after ~2 min of RNase H addition for samples that were passivated for 2 hrs (top row) and 6 hours (bottom row). (**f**) Kinetic plot showing the rate of RNA substrate hydrolysis as a function of passivation conditions. Note that 10% formamide and 0.75% Triton-X surfactants were included in the reaction buffer for the surface that was passivated under

100 µM SH-PEG for 6 hrs. Error bars represent the standard deviation of fluorescence intensity in a single image acquired at a specific position along the well.

For optimally passivated surfaces, we measured a k_{cat} = 25 min^{-1} for RNase H catalyzed RNA hydrolysis. This rate is 6,000 fold greater than the turn-over number for nanoparticle-immobilized DNAzymes, thus supporting our expectation that RNase H powered rolling motors may achieve rapid velocities (**Figure 4.4**).[17,18]

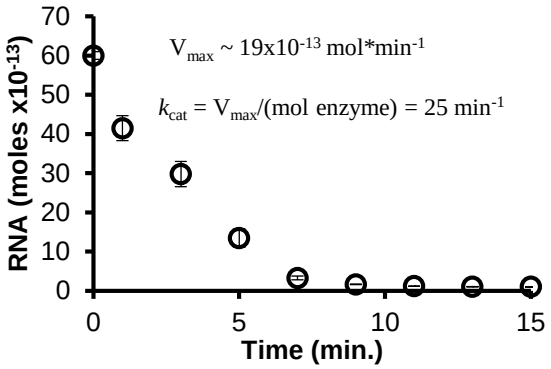

Figure 4.4. A representative kinetic plot showing RNase H hydrolysis of surface immobilized RNA hybridized to a complementary DNA strand. The error bars represent the standard deviation in the average fluorescence intensity from at least 5 different regions across the micro-channel. The absolute number of RNA molecules (y-axis) was inferred by multiplying the area of the micro-channel by the density of RNA per µm^2 that was obtained from the calibration and RNA release measurements. V_{max} was determined by measuring the initial rate of reaction between 0 and 2 min, and k_{cat} was subsequently calculated by using this value of V_{max} and dividing it by the concentration of the enzyme.

4.2.3 Synthesis and characterization of DNA functionalized 5 µm diameter silica particles

High density DNA-functionalized particles were synthesized by functionalization of 5 µm aminated silica beads with NHS functionalized azide, The subsequent azide surface modified particles were then coupled with alkyne modified DNA through Huisgen cycloaddition (**Figure 4.5a**). The DNA density was measured to be ~91,000 molecules/µm^2 (footprint of 11 ± 3 nm^2 per molecule) determined by releasing the DNA

from the particle via HF etching (**Figure 4.5b**) and quantifying the released DNA using the commercial OliGreen assay (**Figure 4.5c**). The DNA functionalized particles were then hybridized to a substrate presenting the complementary RNA strand. Importantly, the DNA density matched that of the RNA density on the planar substrate to ensure a high degree of polyvalency (~10^4 contacts/μm^2), therefore minimizing motor detachment from the substrate and maximizing run processivity.

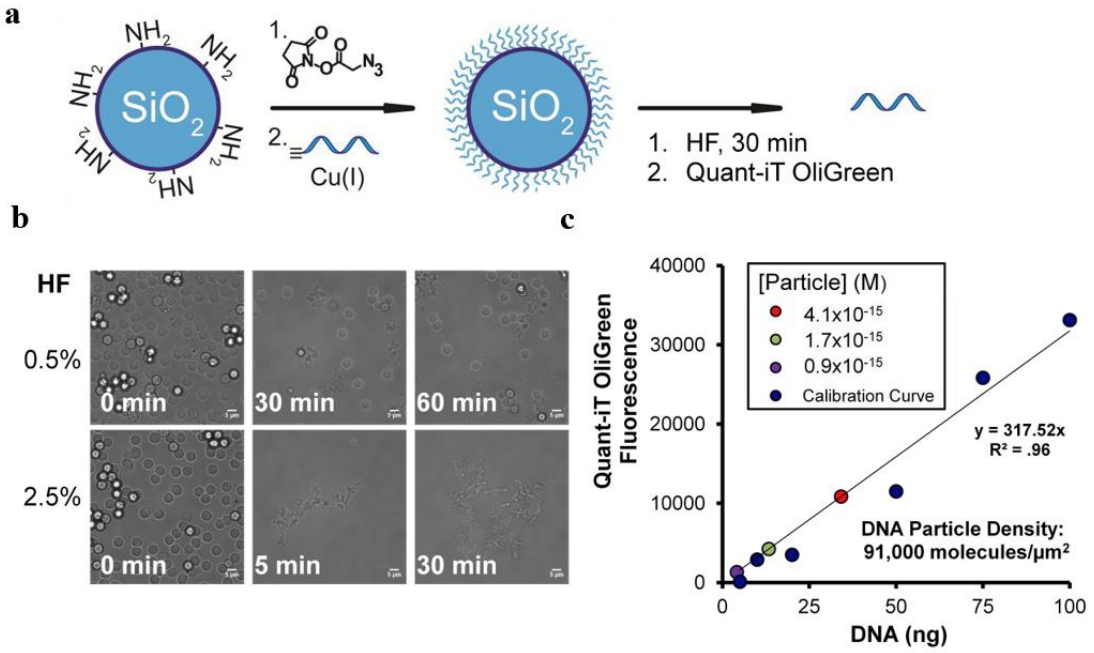

Figure 4.5. (**a**) Schematic showing the approach used to modify the particle with DNA and then to determine the DNA loading number. (**b**) Brightfield images showing particle dissolution over time during incubations with 0.5% and 2.5% HF in 1x PBS. Based on brightfield imaging, spherical particles appeared to be completely etched after 30 min of incubation in 2.5% HF. (**c**) Calibration curve for the 5'alkyne particle DNA using the Quant-iT OliGreen fluorescence assay. Note that the DNA used in this calibration was incubated in 2.5% HF under identical conditions to those used to etch the particles. The DNA released from etched microparticles of three different concentrations (red, 4.1x10^{-15} M; green, 1.7x10^{-15} M; and purple, 0.9x10^{-15} M) from two independent synthesis was then quantified by using the Quant-iT assay. Based on these three, the average DNA density was ~91,000 molecules/μm^2 (footprint of 11 ±3 nm^2 per molecule). Thus, the DNA density matched that of the RNA density on the planar substrate and was sufficiently high to ensure a high degree of polyvalency (~10^4 contacts/μm^2), minimizing motor detachment from the substrate which limits run processivity.

4.2.4 Characterization of particle translocation

Particles remained immobile until RNase H was added, which led to rapid translocation of particles across the substrate. This was quantitatively tracked by finding the centroid of the particles in time-lapse brightfield (BF) microscopy at 5 sec intervals (**Figure 4.6a and Figure 4.28**).[19] Importantly, the BF-generated tracks matched the widefield fluorescence depletion tracks (FWHM of 720 ± 110 nm), confirming that the particle motion was associated with continuous RNA hydrolysis (**Figure 4.6b-c, Figure 4.26, and Figure 4.27**). The line scan analysis of the fluorescence depletion indicates ~50% of the RNA underneath the particle is hydrolyzed (**Figure 4.6c**).

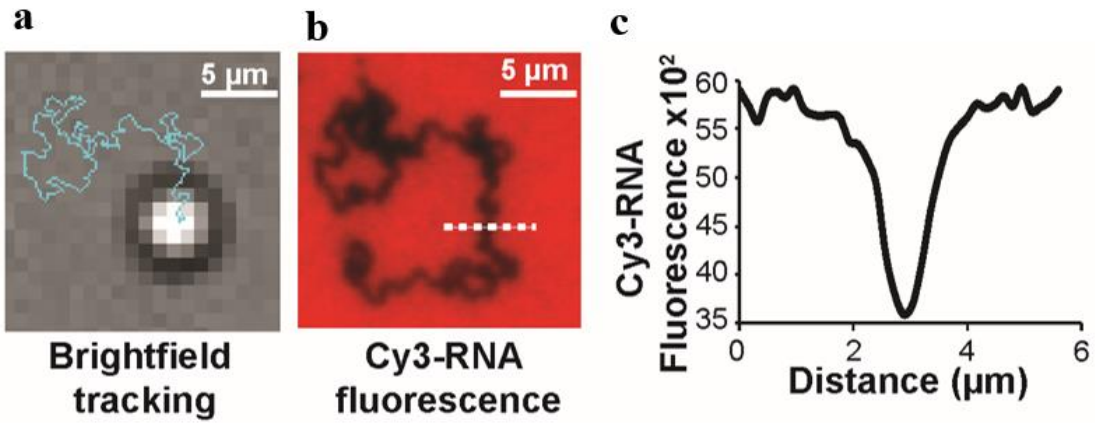

Figure 4.6. (**a**) Representative BF image and trajectory (blue line) from a time-lapse video tracking a single microparticle 30 min following RNase H addition. (**b**) The same region was then imaged in the Cy3 fluorescence channel, revealing the location of depleted Cy3 signal. (**c**) Line scan plot of dashed white line from **c** showing the depletion track from the widefield fluorescence image.

Structured illumination microscopy (SIM), a super resolution fluorescence microscopy technique with ~110 nm resolution revealed a more accurate footprint of the particle substrate junction corresponding to an average track width of 380 ± 50 nm (n = 55 tracks). Based on a simple geometric model, this footprint indicates a maximum of ~5,500 DNA-

RNA surface contacts at the motor-substrate junction (**Figure 4.7**). Importantly, substrates comprised of DNA did not lead to any translocation upon addition of RNase, confirming that particle motion is specific to RNA hydrolysis at the particle-substrate junction.

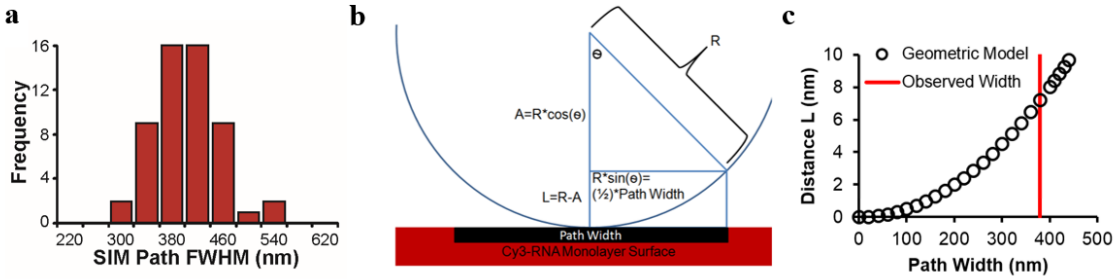

Figure 4.7. (**a**) Histogram analysis of FWHM of the depletion path width acquired using structured illumination microscopy. (**b**) Schematic of the geometric model used to determine the compression/stretching of the DNA/RNA duplex and single stranded segments as a function of pathwidth. (**c**) Plot showing representative distances L as a function of pathwidth for a 5 µm particle. Highlighted in red is the experimentally observed pathwidth determined by SIM microscopy. Note that the expected pathwidth for particles of different diameters can be estimated using this same approach.

4.2.5 Experimental realization and computation models of superdiffusive transport

In principle, the particle should be biased away from consumed RNA substrate and toward new regions that had not been previously sampled. To investigate this model, particle motion was analyzed by plotting the mean squared displacement (MSD) against time *t*, since MSD is known to be proportional to t^{α}.[20] However, we found that the MSD versus time did not have a linear dependence, as is the case for random diffusion ($\alpha = 1$), but rather a power dependence where $\alpha = 1.45 \pm 0.20$, indicating that particle motion is not well described by random diffusion (**Figure 4.8a**). A histogram summarizing the distribution of diffusional exponents for these particles and particles nonspecifically bound to the surface that do not have biased diffusion are shown in **Figure 4.11f**. Moreover,

random diffusion is known to have displacement distributions in the form of $P(x) \sim \exp(-A|x|^{\nu})$ where $\nu = 2$, yet we measured $\nu = 4.3 \pm 1$ (**Figure 4.8b**) (See *additional discussion in section 4.4.2*). Again, further supporting that motion is biased away from hydrolyzed substrate.

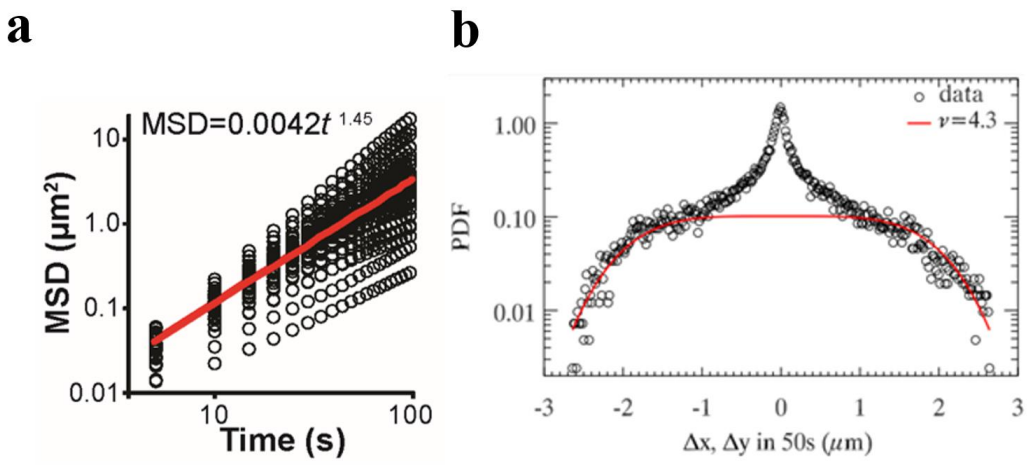

Figure 4.8. (**a**) MSD versus log (time) analysis from individual particle trajectories ($n = 43$), which is shown with black circles. The red line indicates the average slope derived from all the individual particle trajectories. (**b**) A plot showing the probability distribution of displacements for particles powered by RNase H.

We then asked whether particle motion can be described by a self-avoiding random walk, where a particle cannot cross its own path but otherwise moves randomly. These types of self-avoiding random walks have only been theorized, and never experimentally realized. Because self-avoiding diffusion is typically studied using polymer chains,[21] we conducted a multivalent stochastic simulation of hundreds of particles to predict the values for α and ν associated with self-avoiding random diffusion (**Figure 4.9a**). This modeling revealed that over short distances (short timescales) particles exhibit tethered diffusion (MSD ~ t^{α}, with α= 1), and over long distances particles exhibit the scaling MSD ~ $t \log(t)$ which is theoretically expected for self-avoiding behavior (**Figure 4.9b and Figure**

4.24b).[22,23] The rate of data acquisition falls in the transition region between these two time scales, where simulations predict a power-law MSD scaling with α= 1.49 ± 0.05 and a displacement distribution with *v*= 3.8 ± 0.1, both in agreement with the measured values (**Figure 4.8**). These findings demonstrate that DNA-powered particle motors execute motion that is statistically consistent with self-avoiding behavior. To the best of our knowledge, rolling DNA-based motors provide the first experimental realization of the "true" self-avoiding walker (TSAW) statistical process (see *additional discussion in section 4.4.1).*[22,24]

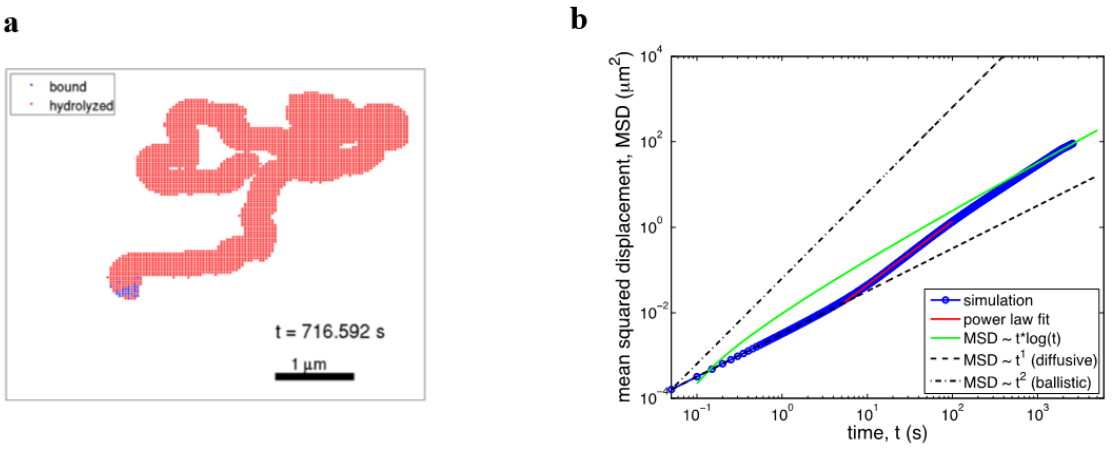

Figure 4.9. (**a**) Snapshot of a multivalent stochastic self-avoiding walk. (**b**) MSD vs time *t* for 733 particles, using time differences at any point along the path. We see two regimes: diffusive behavior at short times (MSD ~ t^1) and self-avoiding behavior at long times (MSD ~ $t \log(t)$). Data from 5 s to 100 s fits well to a power law MSD ~ t^{α} with α = 1.49 ± 0.05, where the mean and standard deviation are computed across 569 individual particle runs that each last longer than 500 s.

4.2.6 Mechanism of particle translocation

Particle motion could occur through three plausible mechanisms: a) walking/sliding, b) hopping, and c) rolling (**Figure 4.10**). The hopping mechanism was immediately ruled out upon examination of the continuous fluorescence depletion tracks (**Figure 4.6b**).

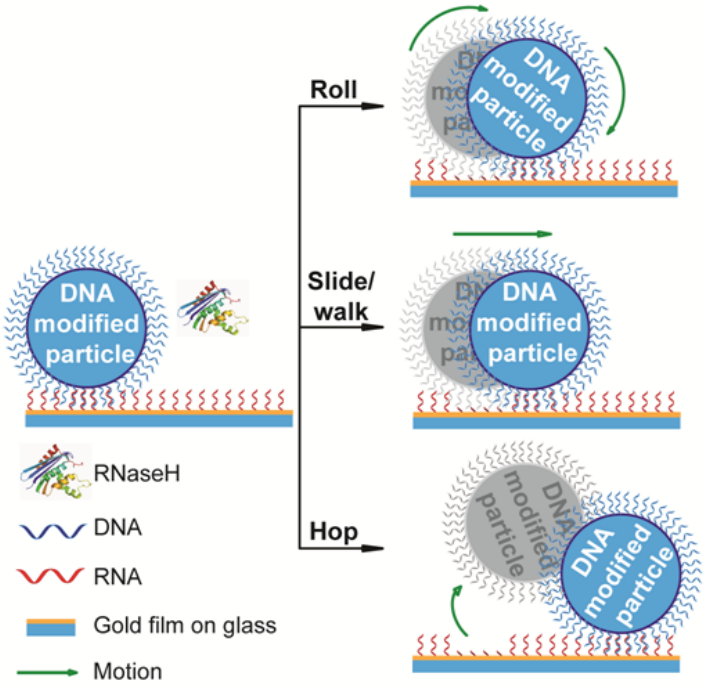

Figure 4.10. A schematic illustrating the potential mechanisms of particle motion (green arrow). If k_{cat} and k_{off} are faster than k_{on}, then particles should hop (scenario shown at bottom) and if k_{cat} and k_{off} are slower than k_{on}, then particles should roll or slide/walk (top two scenarios).

To differentiate between the two remaining mechanisms, particles were hybridized to an RNA substrate, and the unbound DNA on the particle was blocked by hybridization with a complementary DNA strand (**Figure 4.11a**). If motion primarily occurs through a walking/sliding mechanism, we expected that particles would move in a processive fashion leaving behind an RNA depletion track. However, upon RNase H addition, particles diffused randomly, producing an $\alpha = 0.99 \pm 0.22$ and a $v = 1.8 \pm 0.8$, and no corresponding RNA depletion tracks were observed (**Figure 4.11**). By ruling out the hopping and walking/sliding mechanisms of motion, we conclude that particles primarily translocate by rolling, in a monowheel or cog-and-wheel like fashion. The rolling mechanism of motion was further confirmed through two other sets of experiments (*vide infra*). This is the first

example of a DNA-based autonomous rolling motor, and we will subsequently refer to these machines as monowheels.

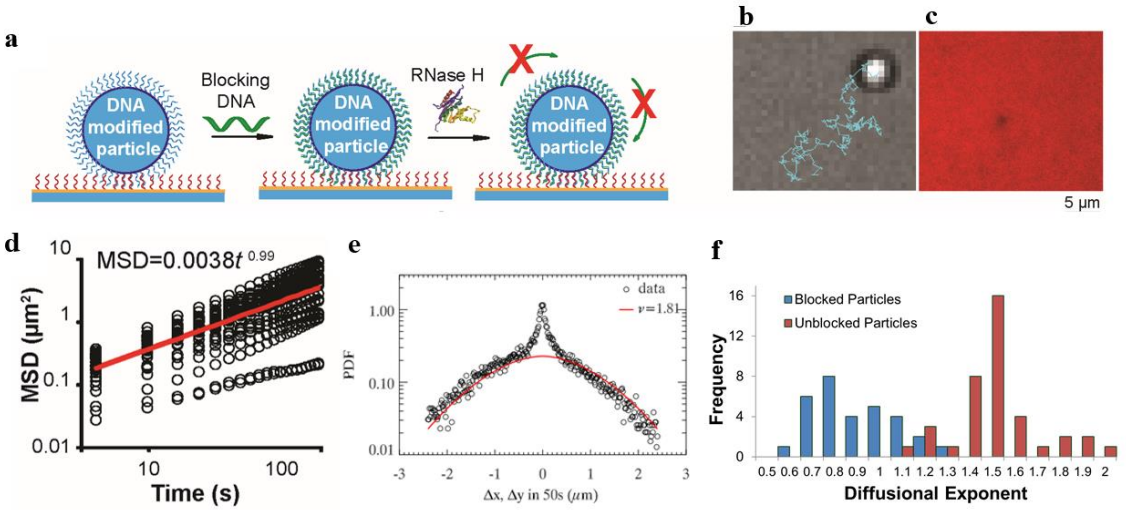

Figure 4.11. (**a**) Schematic showing the strategy used to test whether particles roll during translocation by blocking the free DNA of the particle by hybridizing with a blocking DNA strand (green). (**b**) Representative BF image and trajectory (blue) taken from a time-lapse video tracking a single particle that had been blocked with DNA and treated with RNase H. (**c**) The same region was imaged using the Cy3 fluorescence channel, indicating the lack of a RNA hydrolysis track. Note that a small transient spot with lower fluorescence intensity (see center of fluorescence image) is typically observed under particles and is not due to RNA hydrolysis. (**d**) MSD versus log(time) plot of particle diffusion for the blocked particles. The black circles represent individual data points from n = 32 particles, while the red line indicates the average of these plots. (**e**) A plot showing the probability distribution of displacements for blocked particles. (**f**) Histogram analysis showing the distribution of diffusional exponents for blocked (blue) and unblocked (red) particles. The distribution reflects the degree of self-avoidance.

For particles to move in a cog-and-wheel mechanism, the following sequence of reactions must occur: 1) RNA hydrolysis, 2) DNA unbinding (k_{off}) from the hydrolyzed substrate, 3) tethered particle diffusion (rolling), and 4) DNA hybridization to new RNA substrate (k_{on}). To help determine what parameters affect particle velocity, we measured particle translocation as a function of monovalent and divalent salt concentration, pH, and RNase H concentration. Under high salt concentration we expected that the rate of hybridization (k_{on}) would increase, while the rate of dehybridization (k_{off}) would decrease

and under decreasing pH, k_{cat} would decrease. We found that particle velocity is highly dependent on salt concentration and decreases under higher ionic strengths (**Figure 4.12a,b**). In contrast, particle speed is only sensitive to k_{cat} when k_{cat} is reduced below 0.4 per min (**Figure 4.12c**).

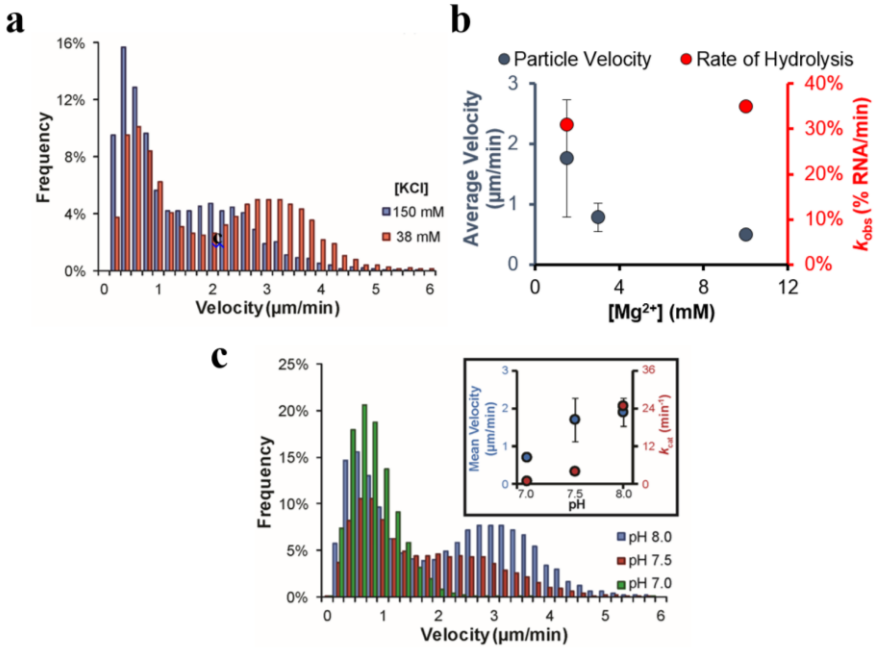

Figure 4.12. (**a**) Histogram analysis of particle velocity for each 5 s interval as a function of [KCl]; 38 mM (red, n = 43 particles (25,800 occurrences)) and 150 mM (blue, n = 52 particles (31,200 occurrences)). (**b**) A plot summarizing the average particle velocity and observed rate of RNA hydrolysis as a function of [Mg^{2+}] concentration. The error bars represent the standard deviation for the particle velocities for all the particles (typically n >15) at each 5 s interval for the 30 min time-lapse video. (**c**) Histogram analysis of particle velocity for each 5 s interval as a function of pH; 8.0 (blue, n = 43 particles (25,800 occurrences)), 7.5 (red, n = 50 particles (30,000 occurrences)), and 7.0 (green, n = 26 particles (15,600 occurrences)). Inset compares RNase H k_{cat} (red) and average particle velocity (blue) as a function of pH.

Importantly, taken together, these results suggest that k_{off} acts as the kinetic bottleneck for particle motion at pH 7.5 or greater (**Figure 4.13**).

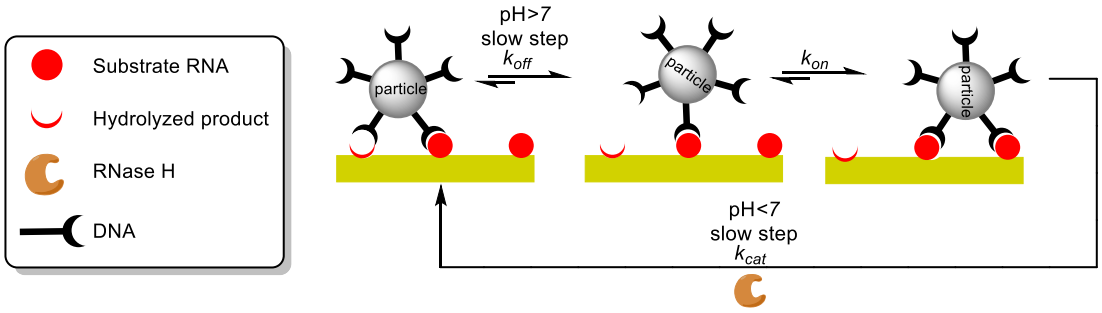

Figure 4.13. Schematic of the proposed mechanism for particle translocation. For simplicity, the multivalent interaction with the surface has been reduced down to a divalent interaction.

Interestingly, the particle speed histogram contains two populations of monowheels (**Figure 4.12a,c**). Upon further analysis of individual particle velocities and accounting for stage drift, the two populations correspond to two states for each particle, a slow/stalled state and a fast state, as opposed to two types of particles or contributions due to stage drift (**Figure 4.14**).

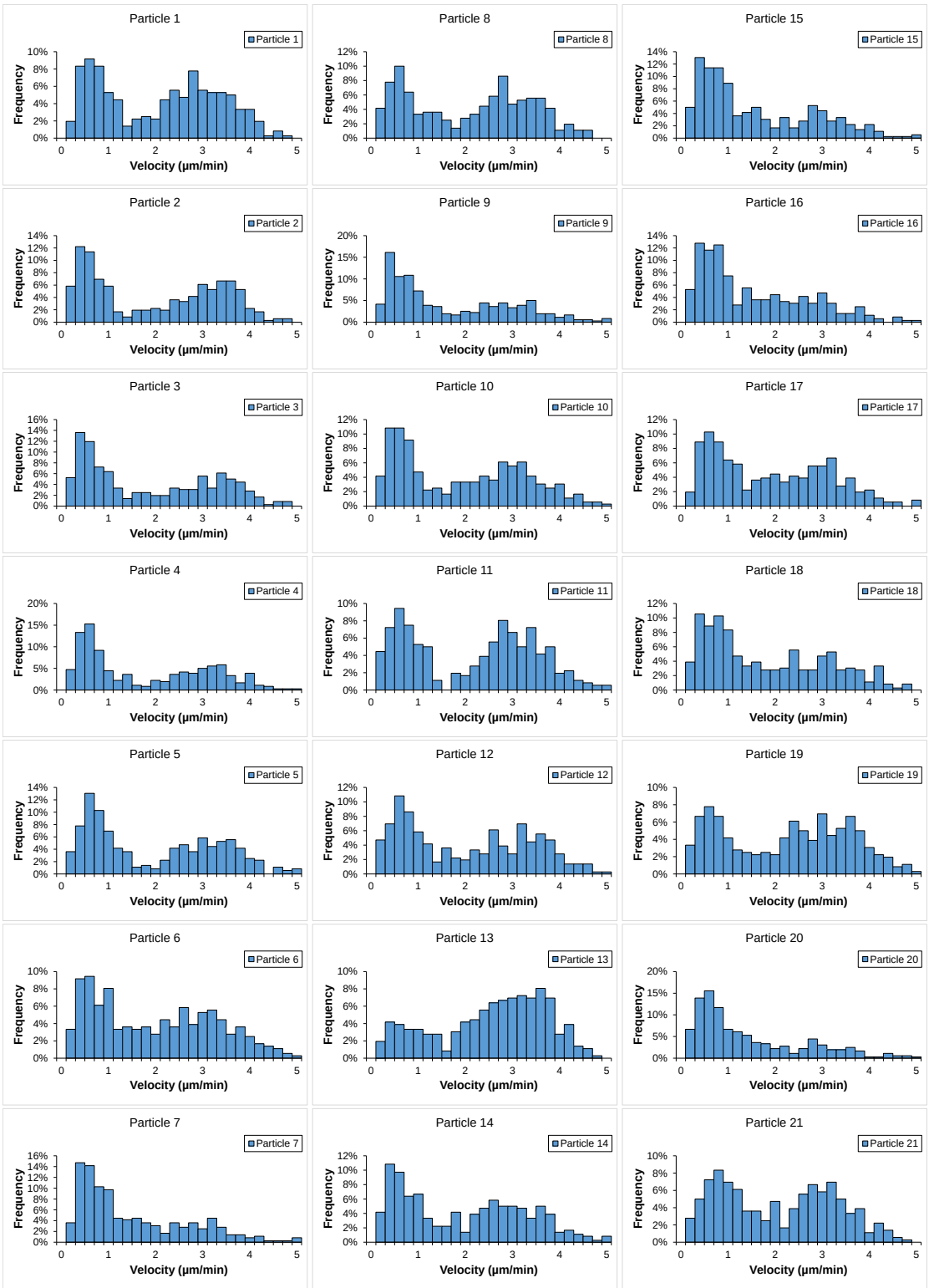

Figure 4.14. Histogram analysis of individual particle velocities (25 mM Tris pH 8.0, 8 mM NaCl, 37.5 mM KCl, 1.5 mM $MgCl_2$, 10 vol % formamide, and 0.75% (g/mL) Triton X).

The slower state maybe due to transient stalling of the particle. This may be due to a combination of factors that include heterogeneity of the surface functionalization which can lead to increased non-specific binding of the particle with the surface, inactive enzyme bound to the particle-substrate junction, and particle self-entrapment, all of which, can limit particle speed. Upon detailed analysis of individual particle trajectories, we found that stalling mostly correlated to particle entrapment (**Figure 4.15**).

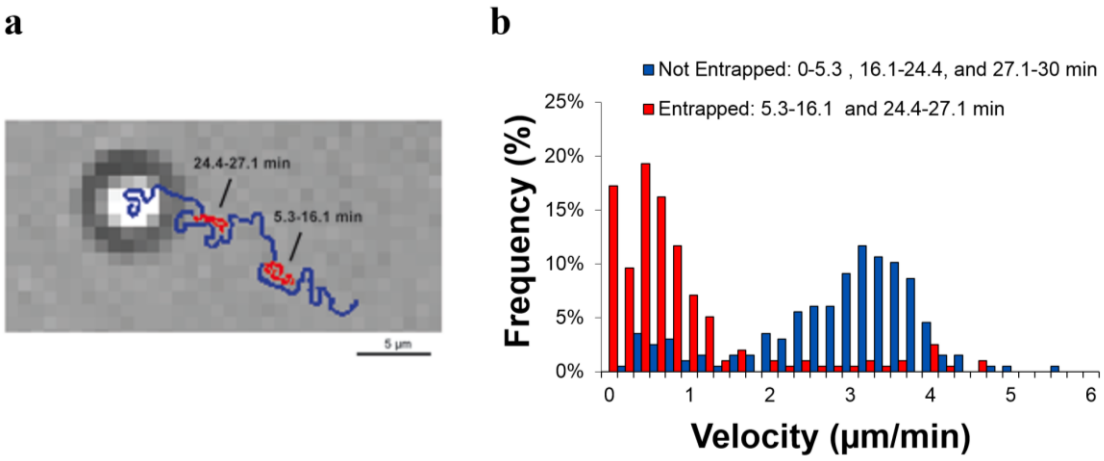

Figure 4.15. (**a**) Representative BF image and trajectory (blue and red) taken from a time-lapse video tracking a single particle for 30 min where the red section indicates when the particle becomes entrapped. (**b**) Representative velocity histogram of an individual particle when the particle is entrapped (red) or not entrapped (blue). Entrapment leads to significant decrease in particle velocity.

To determine whether the enzyme concentration used, [RNase H] = 140 nM, saturated the available substrate binding sites, monowheel velocity was monitored as a function of enzyme concentration (**Figure 4.16**). At 10 fold greater enzyme concentration, only a slight increase in average velocity was observed, whereas 10 fold and 100 fold dilution of RNase H led to near abolition of monowheel motion. The particle speed histograms for decreasing RNase H concentration (**Figure 4.16b,c**) show a gradual decrease in velocity as opposed to a shift to the low velocity population. This indicates that multiple RNase H enzymes are operating in parallel as opposed to a single enzyme.

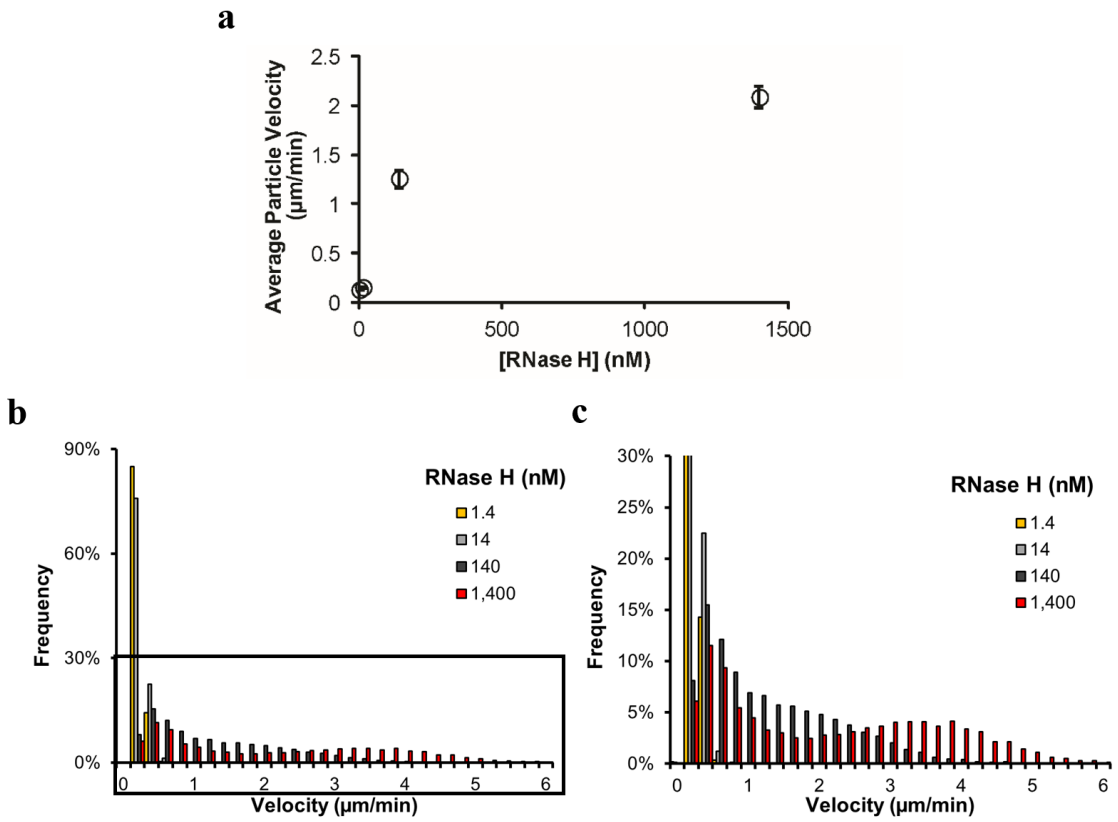

Figure 4.16. (**a**) Plot showing the particle velocity dependence on RNase H concentration. (**b**) Histogram analysis of particle velocity for each 5 s interval of particles with varying RNase H concentrations. (**c**) Expanded view of the inset region.

A general design rule for creating processive DNA machines necessitates that the rate of cleaving contacts and leg disassociation from the track is slower than the rate of forming new track contacts. The stochastic nature of association and disassociation rates implies that molecular DNA walkers will occasionally disassociate from the track. This is reflected in the relatively low fidelity of molecular walkers.[1,7-11] Higher multivalency of DNA-based machines buffers against spontaneous disassociation, thus increasing run processivity.[15,16,25] Our analysis suggests that the monowheels are highly multivalent with at least ~1000 DNA-RNA duplex contacts present at any given time. This estimate is based on the RNA depletion track analysis, which indicates that 50% of RNA is hydrolyzed within the ~400 nm wide track. Given the RNase H turnover rate of 25 min^{-1}, and the RNA

surface density ($1x10^4$ RNA/μm^2), the monowheels must have at least ~1000 contacts to maintain a velocity of 2 μm/min. Fewer contacts would result in lower particle speed. This is a lower bound estimate of the particle multivalency because this calculation assumes every duplex is bound by active enzyme, which is unlikely. Therefore, monowheels display 2-3 orders of magnitude greater multivalency than molecular walkers and this affords significant improvement in motor processivity.

Another important difference between molecular walkers and our monowheels is the effect of gravity on μm-sized particles. Albeit small, the force of gravity (~0.6 pN for a 5 μm silica particle in water) may bias the observed processivity by limiting particle-surface dissociation. To address this issue and determine the role of gravity on particle motion, we inverted the sample geometry such that monowheels were upside down, operating against the force gravity (**Figure 4.17**). Under identical conditions, 80% of the inverted monowheels displayed similar speeds and processivity (distance traveled before stalling) as that of the upright samples. Note that at [KCl] = 38 mM, 20% of particles detached upon flipping the sample, whereas at [KCl] = 75 mM, none of the observed particles detached from the surface and monowheels displayed slightly enhanced velocities to that observed at [KCl] = 38 mM (either when the sample was upright or flipped). Therefore, the primary contributor to monowheel processivity is the high multivalency of the system rather than the force of gravity.

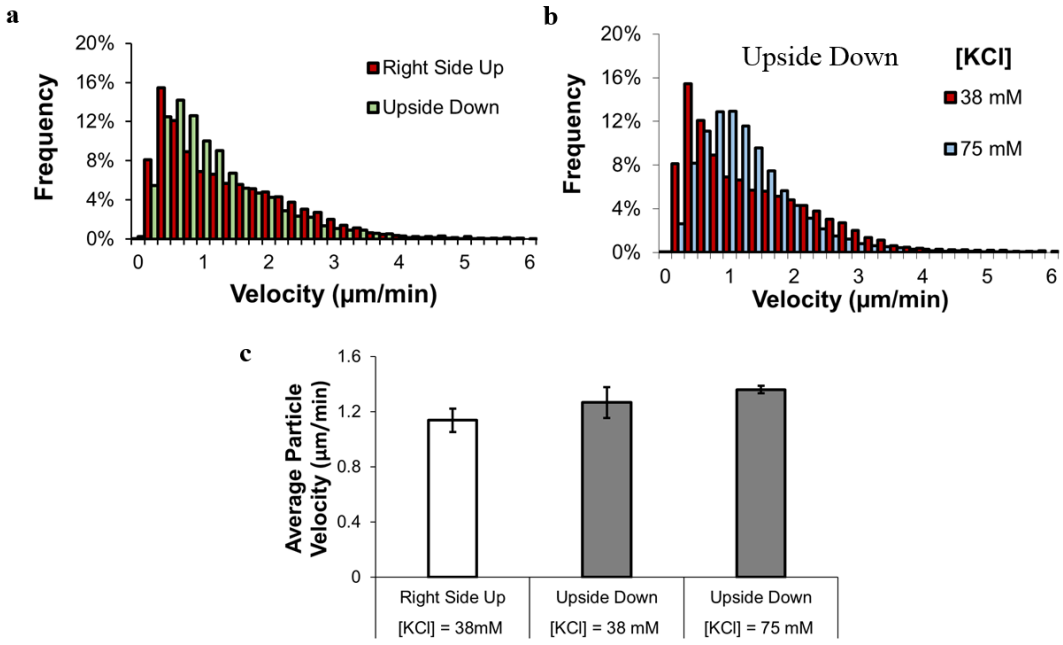

Figure 4.17. (**a**) Histogram analysis of particle velocity for each 5 s interval of particles rolling against the force of gravity (green, n = 16 (5,760 occurrences)) or with the force of gravity (red, n = 20 (7,200 occurrences)) at [KCl] = 38 mM. (**b**) Histogram analysis of particle velocity for each 5 s interval of particles rolling against gravity as a function of [KCl]; 38 mM (red, n = 16 (5,760 occurrences)) and 75 mM (blue, n = 50 (18,000 occurrences)). (**c**) A bar graph summarizing particle velocity.

To simplify analysis and quantification, we used 5 μm diameter particles for the majority of experiments. However, note that the rolling mechanism of translocation can be recapitulated with 0.5 μm diameter particles (**Figure 4.18a**). In principle, these smaller particles reduce the maximum number of DNA-RNA contacts by one of order of magnitude to the range of several hundred. Similar maximum velocities up to 5 μm/min and average velocities of 1.8 ± 0.4 and 1.9 ± 0.5 μm/min were observed for both 0.5 and 5 μm particles, respectively, indicating that the fundamental cog-and-wheel mechanism of rolling is independent of cargo size within the range tested (**Figure 4.18a**). This was initially surprising since the smaller particles have fewer contacts with the surface and reduced drag, resulting in a faster k_{off} thus smaller particles were expected to translocate more

quickly. Upon further analysis, we noted that smaller particles are less multivalent, and therefore fewer RNA-DNA duplexes are available for hydrolysis at any given time. In other words, there is reduced hydrolysis of RNA in parallel when using smaller particles, which is expected to slow down the absolute RNA hydrolysis rate and thus reduce particle velocity. These opposing effects create a complex relationship between motor speed and particle size, and when comparing the 5 μm beads with the 500 nm particles, the effect of particle size effectively cancels out, leading to similar observed velocities. However, the 500 nm particles roll for shorter average run lengths compared to 5 μm diameter particles (~3 μm *versus* ~60 μm), which continue processively moving throughout the 30 min video and even continue moving for over 5 hrs reaching average run lengths of ~200 ± 10 μm (**Figure 4.18b**). The decrease in run length for the 500 nm particles is due to the lower multivalency (fewer contacts) with the surface, thus increasing the probability of detachment. Nonetheless, increasing the KCl and Mg concentrations to 75 mM and 3 mM, respectively, enhances 500 nm particle endurance such that the majority of particles display processive motion for the entire 30 min video. This provides the 500 nm particles with an average run length of greater than 25 μm. Despite much work in the area of DNA-based machines, this class of multivalent rolling motor exceeds the velocity and processivity of previous DNA-motors by three-orders of magnitude, and approaches the efficiency of biological enzymes, with velocities on the order of tens of μm's per second and run lengths of hundreds of μm's.

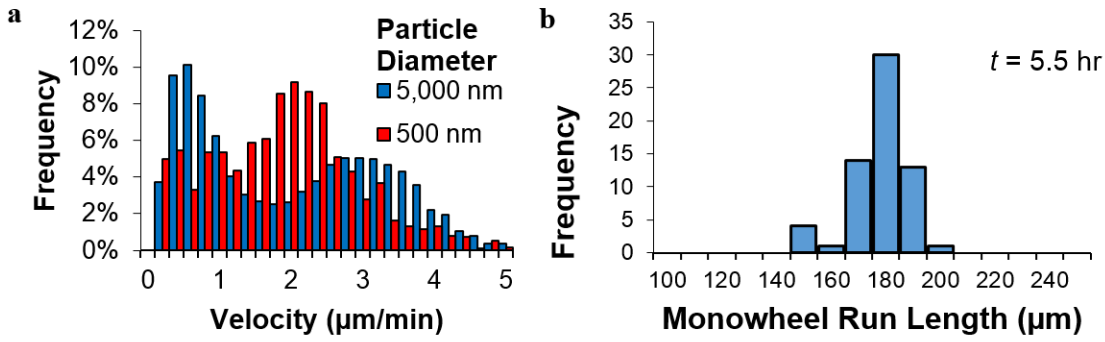

Figure 4.18. (**a**) Histogram analysis of particle velocity for each 5 s interval as a function of particle size (5,000 nm diameter; blue and 500 nm diameter; red). (**b**) Histogram analysis of average monowheel (5 μm) run length after 5.5 hrs. Only 10% of monowheels remained in motion after 12 hrs, which may be due to enzyme denaturation.

4.2.7 Linear transport of RNase H powered DNA monowheels

To achieve unidirectional transport resembling motor protein motion along a filament, RNA was spatially micro-patterned into 3 μm wide tracks (**Figure 4.19a)**. Particles were then hybridized to the patterned RNA, and RNase H was added to initiate motion (**Figure 4.19b)**. Using BF time-lapse tracking and RNA fluorescence depletion, we observed that a subset of particles moved along the 3 μm substrate corral unidirectionaly deflecting away from the PEG-printed regions. Note that many particles became entrapped, partially because of RNA cross contamination into the PEG-passivated regions (**Figure 4.19c**) and self-entrapment in consumed substrate corrals. It is likely that generating well-passivated nanoscale RNA tracks commensurate in size to the particle-substrate junction width (~400 nm) would lead to an increased yield of linear trajectories.[8] Nonetheless, this provides a proof-of-concept demonstration of autonomous translocation using self-assembled components without an external field, akin to the motion of motor proteins.

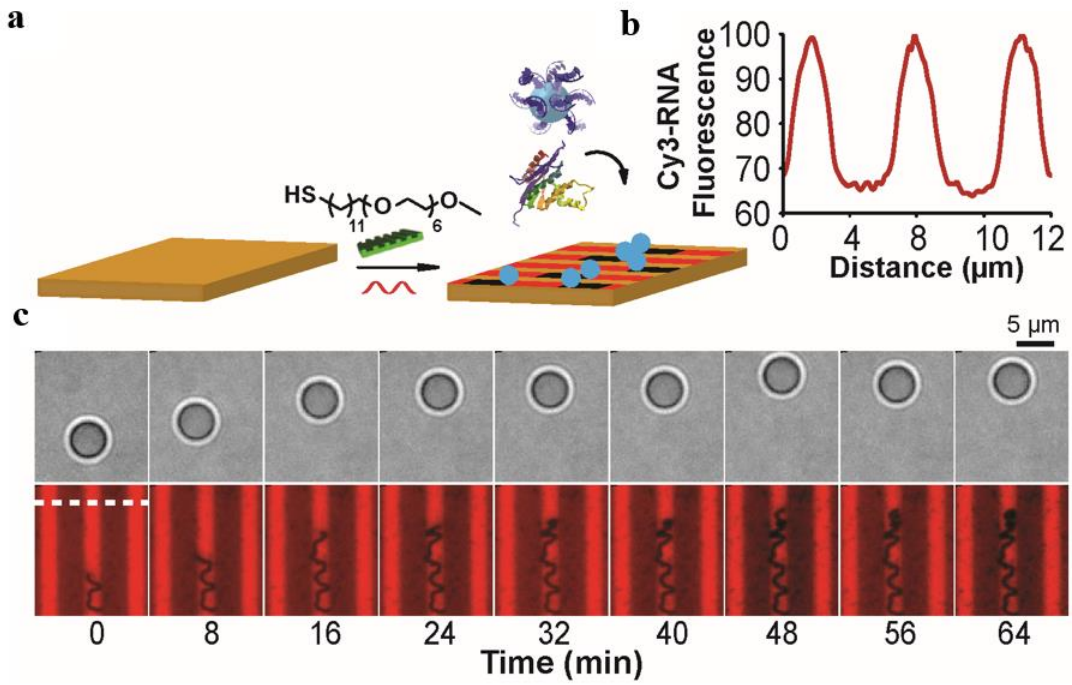

Figure 4.19. (**a**) Schematic showing the strategy used to generate RNA micro-tracks by using microcontact printing. SH-PEG barriers were directly printed onto the gold film, which was backfilled with RNA. (**b**) BF and fluorescence time-lapse images of a particle moving along a 3 μm wide track following the addition of RNase H. (**c**) Line scan analysis of the region highlighted in the fluorescence channel with a dotted white line showing the track dimensions and the effectiveness of the PEG barriers.

An alternate strategy to achieve linear motion would be to limit lateral particle motion by incorporating multiple monowheels on the body of a single chassis. This has been investigated previously by Diehl *et al.*, but given the unique rolling mechanism for our system, we speculated that multiple motors could only result in ballistic or linear motion.[25] By happenstance, we noticed that a 1-10% subset of our particles were fused forming dimers, a common byproduct in silica particle synthesis. We found that these particles traveled linearly for distances that spanned hundreds of μm's at a velocity of ~0.6 ±0.5 μm/min, n = 68 dimer particles (**Figure 4.20a)**. Not surprisingly, a plot of MSD versus t for particle dimers showed a power-law scaling of $\alpha = 1.82 \pm 0.13$, confirming that particle motion was nearly linear ($\alpha = 2$) (**Figure 4.20b)**. In addition, we also discovered that 50%

of single spherical particles displayed a transient component of their trajectory that is linear and associated with wider tracks; linear motion was correlated with wider ~1.0 ±0.1 µm tracks or multiple contact points (**Figure 4.20c, Figure 4.28, and Figure 4.29**). The ballistic (linear) motion observed for what appears to be wider tracks may be due to particles possessing multiple contact points that cannot be resolved or due to particles rolling along imperfections along the surface.

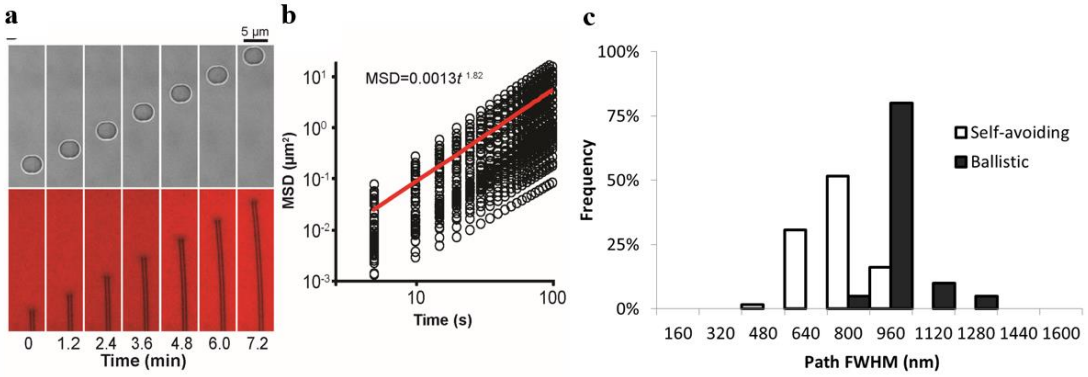

Figure 4.20. (**a**) Representative BF and fluorescence images taken from a time-lapse movie that tracked a dimerized particle following RNase H addition. The BF-analyzed trajectory as well as the two parallel fluorescence depletion tracks showed near linear particle motion. (**b**) MSD versus log(time) analysis of the dimerized particle motion. Slope of this plot shows an average power log dependence of 1.82± 0.13, confirming that the particle dimer traveled in a ballistic, linear fashion. (**c**) Histogram analysis showing the full width half maxima of labeled line scans. As described in the main text, some particles toggled between linear (ballistic) and self-avoiding paths. We classified the tracks as ballistic and self-avoiding and then reported the distribution of these two categories in the histogram. The mean FWHM of ballistic tracks was 1.0 +/-0.1 µm while the mean FWHM for self-avoiding tracks was 717 +/-110 nm.

Following these observations, we synthesized DNA-coated microrods and anticipated similar behavior. Microrods showed nearly linear motion, which demonstrates that the rolling mechanism is not limited to spherical particles (**Figure 4.21**). These are the first examples of directional motion without the need of a patterned track or external

electromagnetic field, which is only afforded due to the unique cog-and-wheel translocation mechanism.

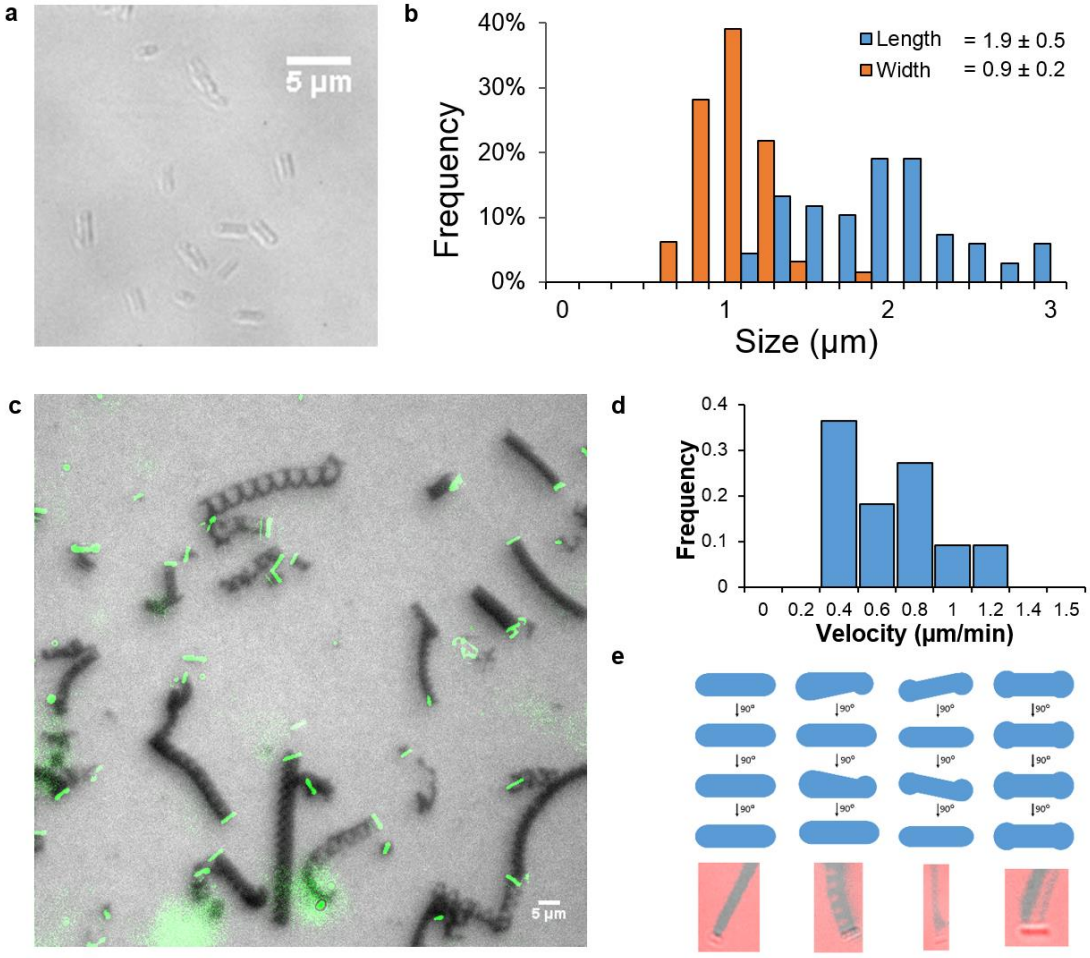

Figure 4.21. (**a**) Representative brightfield image of DNA functionalized sililca micro-rods. Rods were synthesized via emulsion based method[26] and were surface functionalized with APTES.[27] The resulting aminated rods were functionalized with DNA using the same method described previously (NHS-azide amine coupling followed by azide-akyne Huisgen cycloaddition). (**b**) Corresponding histogram analysis characterizing the DNA functionalized micro-rods' length and width. (**c**) Representative overlay of a brightfield (green) and fluorescence (gray) image showing microrod trajectories (fluorescence depletion) at t = 45 min. (**d**) Histogram analysis of average particle velocity. (**e**) Proposed model showing how particle imperfections can lead to spiral like structures.

4.2.8 SNP detection through measuring DNA monowheel displacements

Since monowheel motion is exquisitely sensitive to k_{on}, k_{off} and k_{cat} we anticipated that particle motion could provide a readout of molecular recognition. As a proof-of-concept, we aimed to detect a single nucleotide polymorphism (SNP) mutation, which is a biomedically relevant and challenging mutation to identify. Particles displaying the SNP (5'mAmGTAAT**T**AAmUmC3') traveled ~60% slower (0.3 μm/min) than identical particles with a perfect match (5'mAmGTAAT**C**AAmUmC3') (**Figure 4.22a**). This difference in velocities can be attributed to a slower rate of hydrolysis for RNase H to hydrolyze duplexes possessing a single base mismatch (**Figure 4.23d**).[28] Due to the μm-sized cargo and large distances traveled, even a smartphone camera equipped with an inexpensive plastic lens could detect motion associated with this SNP by recording particle displacement within a short time interval (t = 15 min) (**Figure 4.22b-f**).

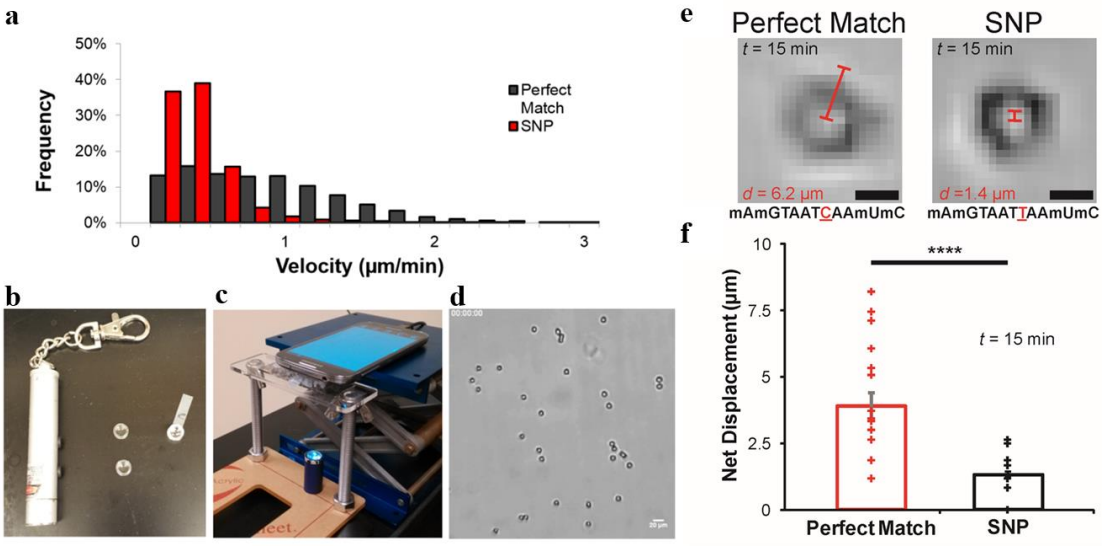

Figure 4.22. (**a**) Histogram analysis of particle velocities obtained for each 5 s interval for particles functionalized with DNA fully complementary to the RNA substrate (Perfect Match, red, n = 36 particles) and DNA that contains a single base mismatch (SNP, red, n = 23 particles). Velocities were obtained by tracking the particle through BF using the microscope. (**b**) A photograph of the plastic magnifying lenses obtained from a toy laser pointer ($2). These lens were used to image the

particles with a smartphone for SNP detection. (**c**) A photograph of the set up used to illuminate and focus onto the sample. (**d**) Representative Smartphone image of the 5 µm particles in the SNP assay. (**e**) Representative bright field images collected by using a smartphone microscope. The images show particles and their net displacement for perfect match and SNP sequences after RNase H addition (t = 15 min). The sequences are illustrated below each image in the 5' to 3' orientation where the single base difference between sequences is underlined and indicated in red and the non-natural 2' methyl ether RNA modification is indicated by the letter m before the base (scale bar = 5 µm). (**f**) A scatter plot displaying particle net displacements 15 minutes following RNase H addition. The mean particle displacement is shown as the height of the bar. Error bars represent standard deviation from n = 42 particles total (p < 0.0001, as determined by a t-Test with unequal variances).

SNP detection could also be achieved using unmodified DNA (**Figure 4.23a-c**); however, maximum discrimination required shortening the RNase H recognition sequence (**Figure 4.22 and 4.23d**). Most importantly, SNP sensing using a smartphone suggests utility in resource limited settings and represents the first realized application for DNA-based motors.

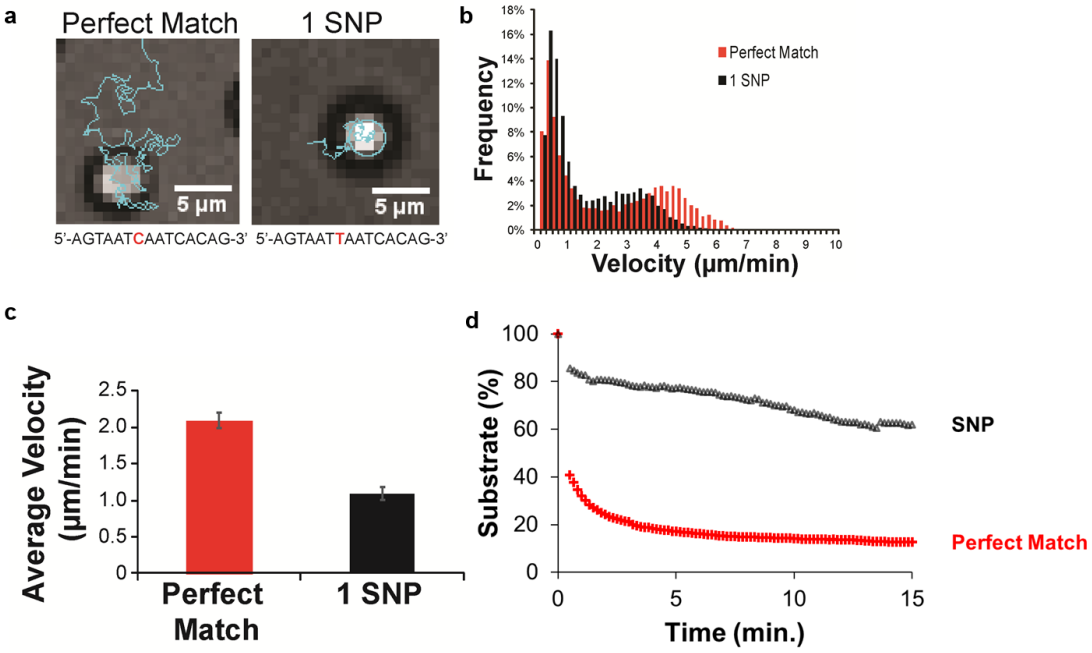

Figure 4.23. (**a**) Representative brightfield trajectories of RNase H driven particle motion for particles modified with fully complementary DNA (Perfect Match) to the RNA monolayer or DNA with a SNP mutation (1 SNP). (**b**) Histogram analysis of particle velocities for Perfect Match (red) and 1 SNP (black) modified particles. (**c**) A bar graph summarizing the average velocities for Perfect Match (red) and 1 SNP (black) modified particles. (**d**) A kinetic plot showing the rate of

RNA hydrolysis for a monolayer of RNA-DNA duplexes that are fully complementary (red) or containing a SNP mutation (black) upon addition of RNase H.

4.3 Conclusions

In conclusion, monowheels take advantage of multivalent substrate interactions to produce emergent collective properties that are difficult to predict *a priori* from the properties of the individual biomolecules.[29-31] The massive multivalency of the system ensures unprecedented motor processivity, allowing monowheels to move distances up to hundreds of μm's. Monowheels also achieve velocities up to ~5 μm/min, a speed which is ~5,000 fold greater than the fastest known synthetic DNA walker and approaching the velocities of biological motor proteins.[8] It is important to note that monowheels use the same chemistry as molecular walkers -specific DNA-RNA hybridization followed by RNA hydrolysis. Moreover, the leg to leg spacing (DNA-DNA spacing) for the walkers is similar to the spacing between DNA strands for monowheels (~5 nm). However, the monowheels differ from the DNA walkers because of their massive multivalency, which leads to collective behaviors such as track free linear motion and rolling. Although highly multivalent motors typically display diminished speeds, monowheels break this trend due to a combination of factors that include a reduction in unproductive DNA-surface contacts enabled by rolling and the parallel activity of RNase H in a highly dense DNA-RNA contact area (as suggested by modeling). Further experiments with anisotropic particles and different enzyme-substrate pairs will elucidate the role of these contributions. At best, the efficiency of converting chemical energy into mechanical work for monowheels is approximately 0.001%, which is on par with chemically powered synthetic motors[32] and may be further optimized in the future (*Calculations found in power conversion efficiency section 4.4.3*). Due to the multi-μm sized chassis, and rapid translocation rates, real-time

tracking of movement can be achieved with conventional optical microscopy and even a smartphone-based readout, thus circumventing the need for specialized AFM and electron microscopy-based analysis. Because of the highly sensitive cog-and-wheel rolling mechanism of motion, monowheels represent an important step in bringing together the field of DNA-based sensing with the emerging area of DNA machines and motors. For example, motor velocity can likely be modulated by aptamer-analyte interactions, suggesting that monowheels will become a new and powerful tool in label-free sensing assays.

4.4 Materials and Methods

4.4.1 Theory and simulation of self-avoiding particle rollers

4.4.1.1 True self-avoiding walk

To investigate whether our particles exhibit self-avoiding behavior, we first performed a simple simulation of a self-avoiding random walk. A particle starts at the origin of a two-dimensional square lattice. At each fixed time step, the particle moves with equal probability to any one of its neighboring sites that has not been occupied in the past. The particle eventually traps itself, which marks the end of the simulation (**Figure 4.24a**).

Self-avoiding walks have been well studied in polymer physics, since a polymer is a chain that cannot overlap with itself. However, there is an important difference between a self-avoiding chain and a self-avoiding walk. The first is a physical object; the second is a dynamic process. In general, when self-avoiding walks are discussed in the literature, this typically refers to self-avoiding (polymer) chains. The dynamic process is usually distinguished from self-avoiding polymer chains by being described as the “true” or

"myopic" self-avoiding walk. Here, we are studying the dynamic process, the "true" self-avoiding walk.

The difference arises at the level of statistics. Averaging over all possible configurations of a length *t* chain, the mean squared displacement (MSD) from end-to-end scales in two dimensions as MSD ~ $t^{3/2}$. However, this is not true for the walk. The reason is that when dynamically generating the walk by taking random steps, one does not sample all *t*-step configurations equally[33]. The result is that the MSD for the walk in two dimensions scales with time *t* as MSD ~ *t* log(*t*) for large values of *t* [22,23].

Figure 4.24b shows MSD versus time for the simulation, averaging over 1000 particles, using time differences at any point along the path. Note that at sufficiently long times, the simulation follows the expectation MSD ~ *t* log(*t*). For comparison, we also show the expectations for ballistic motion (MSD ~ t^2) and diffusive motion (MSD ~ t^1).

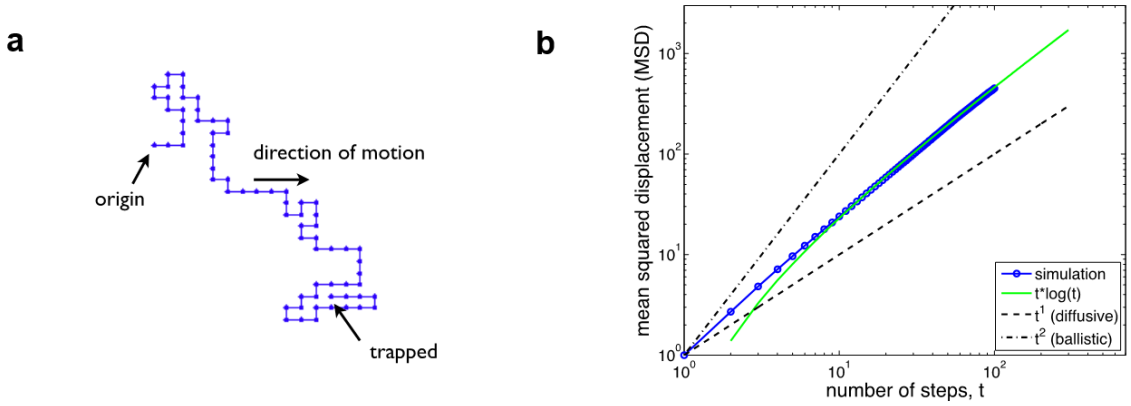

Figure 4.24. (**a**) Simple self-avoiding random walk. (**b**) MSD vs time *t* for 1000 particles, using time differences at any point along the path. We see that at sufficiently long times, the simulation follows the expectation for a self-avoiding walk, MSD ~ *t* log(*t*).

4.4.1.2 Multivalency and enzyme kinetics

The simple simulation in the previous section lacks two key features of the experimental particles. First, the particles are multivalent, meaning they bind the surface

at many points at any given point in time. Second, their motion is driven by enzymatic hydrolysis, such that the timing of unbinding events is not fixed but rather depends on stochastic chemical kinetics. Here we incorporate both features into the simulation.

Multivalency is incorporated by allowing the particle to bind at more than one site at a time (**Figure 4.9a**). Sites are distributed on a square lattice. No two concurrently bound sites may be separated by a distance larger than the path width, which is measured experimentally. Stochastic kinetics are incorporated by drawing unbinding times from a probability distribution. As suggested experimentally, we assume that a single slow step sets the unbinding rate k. Unbinding times are then drawn from an exponential distribution with mean $1/k$. Once a sufficient number of unbinding events occur, the particle may access new sites within the path width constraint. These sites are bound in a random order until the constraint is satisfied. Binding is modelled as instantaneous because the binding time (on the order of microseconds) is significantly shorter than the unbinding time (on the order of seconds). .

Figure 4.9b shows MSD versus time for the simulation with multivalency and stochastic kinetics, averaging over 733 particles, using time differences at any point along the path. We see that the simulation exhibits two regimes. At short times, the particles exhibit diffusive behavior (MSD ~ t^1). This is due to the small random movements that accompany individual unbinding events. Individual events do not appreciably change the particle's mean position at short times, but instead introduce short-range diffusive "noise". At long times, the particles exhibit self-avoiding behavior (MSD ~ $t \log(t)$). This is because on length scales larger than the path width (380 nm), the particle effectively executes a self-avoiding random walk. **Figure 4.9b** thus demonstrates that on sufficiently long length

and time scales, self-avoiding behavior persists even with multivalency and stochastic kinetics.

Particle tracking experiments allow for measurement of the MSD over time windows from 5 s to 100 s, revealing a power law scaling MSD ~ t^{α} with α = 1.45 ± 0.2 (**Figure 4.8a**). In this range of time windows, the simulation data also fit well to a power law, with α = 1.49 ± 0.05 (**Figure 4.9b**). The agreement demonstrates that experimental particle motion is statistically consistent with a multivalent self-avoiding walk.

The results in **Figure 4.9b** are obtained with a multivalency of s = 10 lattice sites per path width, which is the highest computationally tractable value. However, in experiments, the measured path width of 380 nm and the substrate footprint of 20 nm^2 imply that the multivalency could be as high as s = (380 nm)/√(20 nm^2) = 85. Therefore, we tested the dependence of the MSD statistics on the multivalency for the tractable values s = 4 to 10. **Figure 4.25** shows that the fitted power α is largely independent of multivalency, suggesting that our simulation provides a good model for the experiment, even if the experimental multivalency is higher than s = 10. The reason that the statistics are independent of multivalency is that at long length and time scales, the particle essentially moves via a rolling mechanism. This means that if the particle is rolling in a particular direction, time between when a contact binds at the front and when it unbinds at the back is independent of the number of other bound sites (see *velocity estimate* below for further discussion).

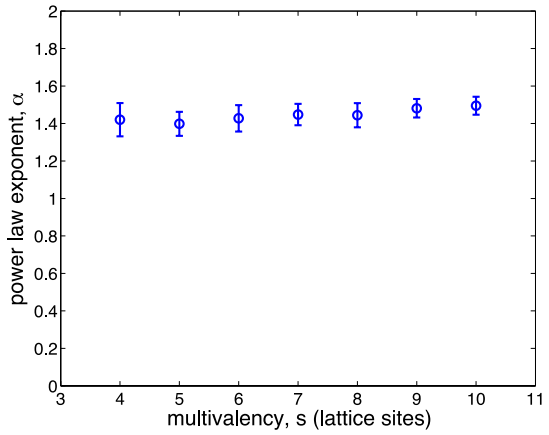

Figure 4.25. MSD power-law exponents α as a function of multivalency s, defined as the number of lattice sites per path width. Path width is kept constant at w = 380 nm while s is varied. For each value of s, exponents and standard deviation are computed from between 20 and 85 particle runs that last longer than 500 s, using time windows between 5 s and 100 s. We see that the exponent is largely independent of the multivalency.

4.4.1.3 Displacement distribution

Our multivalent stochastic simulation also permits a comparison with the experimentally measured distribution of particle displacements (**Figure 4.8a**). There we found that large displacements x are well described by the form $P(x) = P(0)\exp(-A|x|^{\nu})$ with $\nu = 4.3 \pm 1$. **Figure 4.26a** shows the distribution of displacements in 50 s from simulations of 733 particles, using time differences at any point along the path. To determine whether the above functional form provides a reasonable fit, we note that it can be rewritten as $\log[P(0)/P(x)] = A|x|^{\nu}$, which means that a plot of $\log[P(0)/P(x)]$ versus $|x|$ should be linear on a log-log scale, with slope ν. **Figure 4.26b** shows this plot, demonstrating that the dependence is indeed linear for sufficiently large $|x|$ (i.e. in the tails of the distribution). The slope is $\nu = 3.8 \pm 0.1$, which agrees with the experimental value of $\nu = 4.3 \pm 1$. The agreement further supports the statistical consistency of our particle motion with self-avoiding behavior.

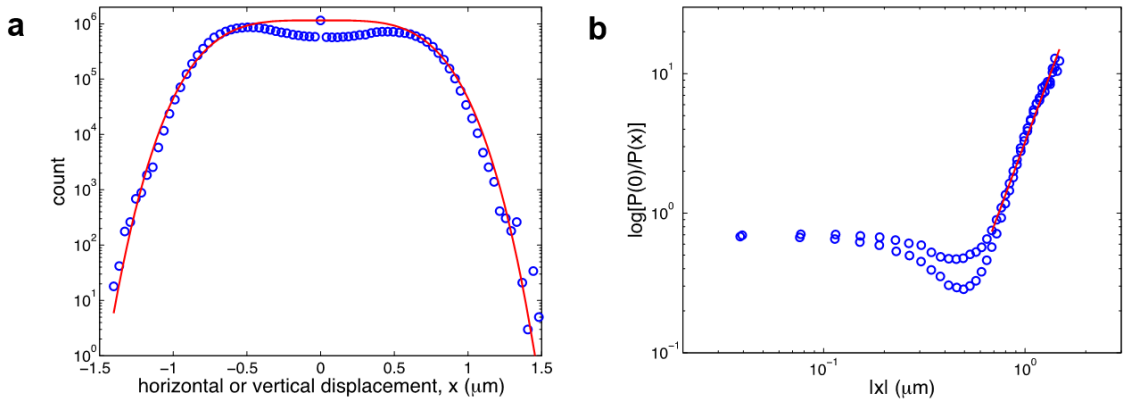

Figure 4.26. (**a**) Distribution of particle displacements x in 50 s. 733 particles are used, using time differences at any point along the path. Red curve shows fit to $P(x) = P(0)\exp(-A|x|^{\nu})$ with $\nu = 3.8 \pm 0.1$. (**b**) The parameter ν is obtained by fitting the linear region of the plot of $\log[P(0)/P(x)]$ versus $|x|$ on a log-log scale.

4.4.1.4 Velocity estimate

Here we present a rough estimate of the particle velocity based on the enzyme kinetics. Unbinding occurs at a rate on the order of $k \sim 10$/min. As mentioned above, the multivalency could be as high as $s = 90$ binding sites per path width. Thus, a naïve argument might suggest that moving one path width $w = 380$ nm requires $s = 85$ unbinding times, or $s/k = 8.5$ min, corresponding to a velocity of roughly 45 nm/min. This is much slower than the experimentally measured velocity of 2 μm/min.

However, the above argument neglects the processivity of the rolling process. To understand this point, we consider the limit of a fixed unbinding time and ballistic motion. In this limit, contacts bind and unbind sequentially in the direction of motion. This means that by the time a particular contact unbinds, all contacts behind it have already unbound, and all contacts in front of it have yet to unbind. In particular, this means that the time between when a contact binds in front, and when the same contact unbinds in back, is equal to one unbinding time $1/k$. In this time, the particle has moved one path width w, and thus

the velocity is wk = 3.8 μm/min. Because in reality unbinding is stochastic, and motion is not completely ballistic, this estimate is an upper bound. Nonetheless, it much more closely reflects the measured value of 2 μm/min.

The above argument implies that particle motion is largely independent of multivalency s, due to the processivity of the rolling process. That is, the particle rolls one path width per unbinding time, no matter how many contacts are bound within the path. Indeed, this provides an explanation for why the statistics of particle motion in the simulation, as captured by the MSD, are largely independent of multivalency (**Figure 4.25**).

4.4.2 Displacement distributions from particle tracking

To ensure that v = 4 is not an artifact of a particular time interval, we analyzed the time dependence of σ across all time intervals. If v = 4 and MSD is proportional to $t^{1.5}$ (based on theory and experimental results), then σ should be proportional to $t^{0.75}$ (based on the derivation below). We find that experiments agree well with this scaling in σ (**Figure 4.27**).

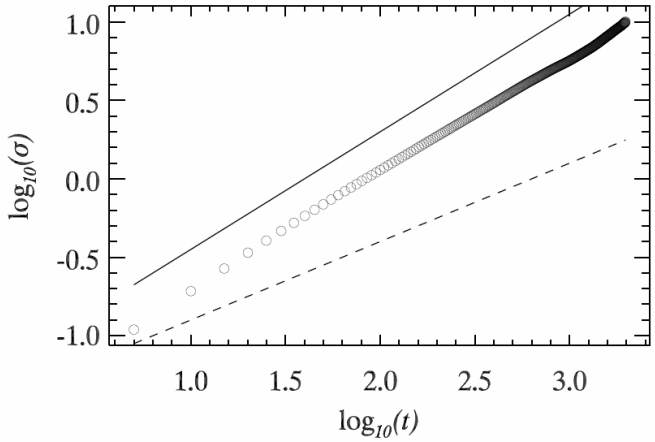

Figure 4.27. A plot showing the log(σ) vs log(t) dependence. The straight line is the expected slope for self-avoiding diffusion (0.75), the dashed line is the slope for random diffusion (0.5), and the circles are the data for unblocked particles. The slope for experimental data (circles) fits well with the slope for self-avoiding diffusion, thus validating our expectations.

Consider the general case where x has the exponent ν. Here, the probability density function is:

$$P_\nu(x,t) = \frac{\nu}{2\sigma\Gamma(1/\nu)} e^{-|x|^\nu/\sigma^\nu}$$

where σ has a time dependence, σ(t), and Γ is a gamma function.[21] If ν is equal to 4 for self-avoiding motion (**Figure 4.8b**), upon integrating we get:

$$< x^2 >= \int x^2 P(x,t) dx \propto \sigma^2$$

We also know from our experiments and simulations (**Figure 4.8a and 4.9b**) that $x^2(t) \propto t^{1.5}$. By substituting σ^2 for x^2, we get $\sigma \propto t^{0.75}$.

4.4.3 Power conversion efficiency

The power conversion efficiency (η) for the monowheel motor can be quantified as described by Wang *et al.*[32]

$$\eta = \frac{\text{mechanical power output}}{\text{total chemical power input}} = \frac{P_{\text{mechanical}}}{P_{\text{chemical}}}$$

where $P_{\text{mechanical}}$ is defined as,

$$P_{\text{mechanical}} = F_{\text{drag}} v = \int v^2$$

F_{drag} is the resistive force on the particle, v is the particle velocity, and ∫ is the friction coefficient.

The particle velocity can directly be measured and the friction coefficient between a DNA modified silica bead and an RNA monolayer can be derived from the experimentally measured diffusion coefficient (D) using the Einstein diffusion relationship:

$$D = \frac{k_b T}{\int}$$

where k_b is the Boltzmann constant and T is the temperature. The 2D diffusion coefficient was measured to be D = 0.096 μm^2/s for DNA modified particles diffusing across an RNA monolayer, which was derived from the slope of the MSD versus time for randomly diffusing blocked particles (**Figure 4.11c**).

$$P_{\text{chemical}} = n_{\text{RNA Hydrolysis}} \Delta_r{}^{o}\text{G}$$

Where $n_{\text{RNA Hydrolysis}}$ is the turnover number for hydrolysis and $\Delta_r{}^{o}\text{G}$ is the Gibbs free energy for the hydrolysis of an RNA phosphodiester bond (30 kcal/mol).[34] The turnover number for RNA hydrolysis can be quantified from the particle velocity (v), contact diameter (d), and RNA density on the surface as detailed below:

$$n_{\text{RNA Hydrolysis}} = \text{v} * \text{d} * \frac{1\text{RNA}}{18\ \text{nm}^2} * \frac{\text{hydrolyzed phosphodiesters}}{\text{RNA}} * \frac{1\ \text{mole}}{6.022 * 10^{23}}$$

Based on these calculations, the power efficiency was found to be approximately 7.8x10^{-6} to 5.6x10^{-7} depending whether 1 to 14 RNA phosphodiesters are cleaved per RNA/DNA duplex.

4.4.4 Materials

All chemicals were purchased from Sigma-Aldrich unless otherwise noted. Stock solutions were made using Nanopure water (Barnstead Nanopure system, resistivity = 18.2 MΩ), herein referred to as DI water. 5-μm aminated silica beads were purchased from Bangs Laboratory (Product #: SA06N). The DNA fluorescence assay kit (Quant-iT™ OliGreen® ssDNA kit) was acquired from Life Technologies (formerly Invitrogen,

Carlsbad, CA) and was used to quantify DNA density on the particle surface. All oligonucleotides were custom synthesized by Integrated DNA Technologies (IDT) and are summarized in **Table 4.1**. RNase H was obtained from Takara Clontech (Product #: 2150A). Thin Au films were generated by using a home-built thermal evaporator system. All Au surface functionalization was carried out using an IBIDI sticky-Slide VI$^{0.4}$ 17 x 3.8 x 0.4 mm channels.

4.4.5 Oligonucleotide sequences

ID	Sequence (5'-3')
DNA Anchor	/5AmMC6/GAGAGAGATGGGTGCTTTTTTTTTTTTTTT/3ThiolMC3-D/
RNA/DNA Chimera Substrate	GCACCCATCTCTCTCrCrCrCrCrCrCrUrGrUrGrArUrUrGrArUrUrArCrU /3Cy3Sp/
DNA Control Substrate	GCACCCATCTCTCTCCCCCCCTGTGATTGATTACT/3Cy3Sp/
Particle DNA	/5Hexynyl/TTTTTTTTTTTTTTTAGTAATCAATCACAG
RNA Complement	AGTAATCAATCACAG
Particle Blocking Strand	CTGTGATTGATTACT
Perfect Match	/5Hexynyl/TTTTTTTTTTTTTTTmAmGTAAT**C**AAmUmC
SNP	/5Hexynyl/TTTTTTTTTTTTTTTmAmGTAAT**T**AAmUmC

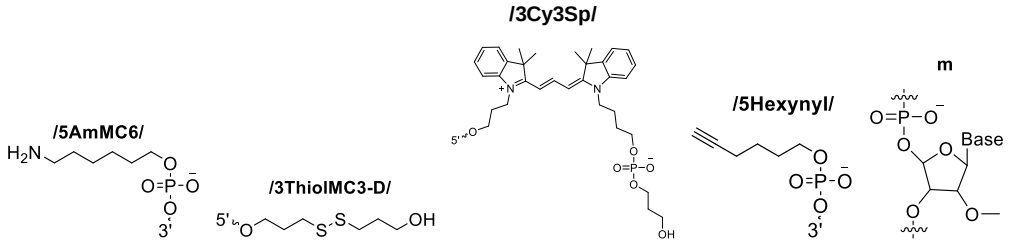

Table 4.1. List of all the oligonucleotide sequences.

4.4.6 Optical Microscopy

Brightfield and fluorescence images were acquired on a fully automated Nikon Eclipse Ti TIRF microscope controlled using the Elements software package (Nikon). Images were collected using the Evolve electron multiplying charge-coupled device (EMCCD; Photometrics) through a CFI Apo 100× 1.49 NA objective or a Plan Fluor 20× 0.50 NA objective. Fluorescence images of Cy3 were collected using an Intensilight Hg lamp epifluorescence source (Nikon), and TRITC filter cube set supplied by Chroma. An interferometric lock-in focus system (Perfect focus system (PFS)) was used during acquisition of time lapse movies to minimize focus drift.

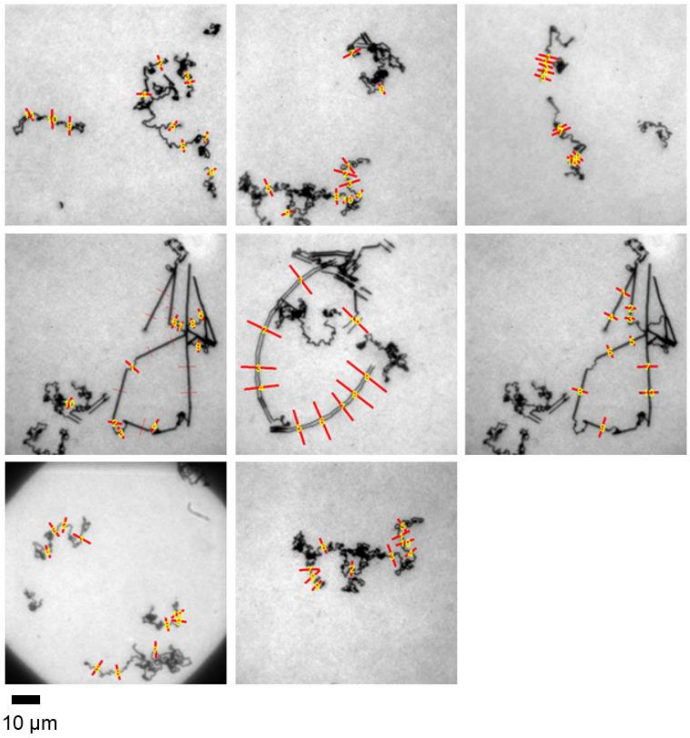

Figure 4.28. Epifluorescence images used to calculate the of the fluorescence depletion track widths (FWHM).

4.4.7 Super resolution imaging of the fluorescence depletion tracks

Structured illumination microscopy (SIM) images were acquired on a Nikon N-SIM system, which is equipped with a CFI Apo 100× 1.49 NA objective and Andor iXon

EMCCD (60nm/pixel). For each N-SIM image, 9 images of 3'Cy3-RNA sample were acquired in different phases using a 561 nm laser as an excitation source and was reconstructed using Nikon Element software package.

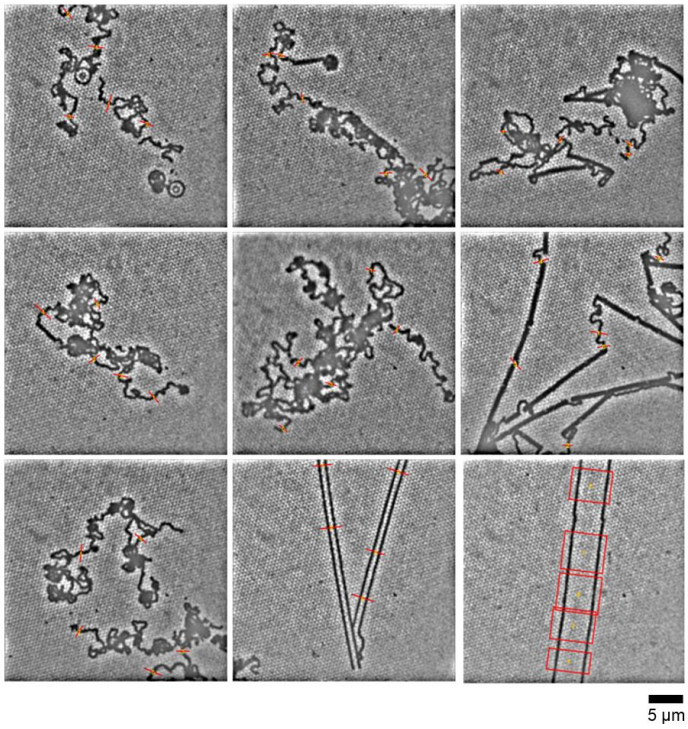

Figure 4.29. SIM fluorescence images used to calculate the of the fluorescence depletion track widths (FWHM).

4.4.8 Thermal evaporation of gold films

A number 1.5 glass slide (25 mm x 75 mm) was cleaned by sonication in DI water for 5 min. The sample was then subjected to a second sonication in fresh DI water for 5 min. Finally, the slide was sonicated in propanol for 5 min, which was subsequently dried under a stream of N_2. The cleaned slide was then introduced into a home built thermal evaporator chamber and the pressure was reduced to 50 x 10^{-3} Torr. The chamber was purged with N_2 three times and the pressure was reduced to 1-2 x 10^{-7} Torr by using a turbo pump and cooling the chamber using a liquid N_2 trap. Once the desired pressure was achieved, a 1.5 nm film of Cr was deposited onto the slide at a rate of 0.2 Å/sec, which was determined by

a quartz crystal microbalance. After the Cr adhesive layer was deposited, 4 nm of Au was deposited at a rate of 0.4 Å/sec. The Au-coated samples were used within one week of evaporation.

4.4.9 Fabrication of RNA monolayers

An IBIDI sticky-Slide $VI^{0.4}$ flow chamber was adhered to the Au-coated slide to produce six channels (17 x 3.8 x 0.4 mm dimensions). Prior to surface functionalization, each channel was washed with ~5 ml of DI water. Next, a densely packed DNA monolayer was assembled onto the Au surface by using published protocols where 40 µL of a 1 µM 3' disulfide modified DNA strand (anchoring strand) was incubated with the surface for 12 hrs under high ionic strength buffer (1 M $KHPO_4$).[35] The chamber was then sealed by Parafilm to prevent evaporation. After incubation, excess DNA was removed from the channel using a ~5 ml DI water rinse. To block any bare gold sites and to maximize hybridization of RNA to the DNA anchoring strand, the surface was backfilled with 100 µL of a 100 µM $SH(CH_2)_{11}(OCH_2CH_2)_6OCH_3$ (SH-PEG) solution in ethanol for 6 hrs. Excess SH-PEG was removed by ~5 ml rinses with ethanol and water each. Lastly, the RNA substrate was immobilized to the surface through hybridization of 100 µL of a complementary RNA/DNA chimera (100 nM) in 1x PBS (phosphate buffered saline) for 12 hrs. The wells were then sealed with Parafilm to prevent evaporation and the resulting RNA monolayer remained stable for ~1-2 weeks, as determined based on fluorescence imaging.

4.4.10 Determining RNA surface density

RNA surface density was determined by releasing the Cy3-tagged RNA from the surface by adding 100 µL of RNase A (100 µg/ml in 1 xPBS) and then quantifying the Cy3

fluorescence intensity in solution using a calibration curve obtained using the fluorescence microscope.

4.4.11 μ-contact printing of RNA tracks

To generate RNA tracks, SH-PEG barriers were initially patterned onto the thin gold film using established protocols.[36] Briefly, 30 μL of a 1 mM SH-PEG solution in ethanol was applied to a PDMS stamp with 3 μm wide parallel lines spaced at a 3 μm pitch. Next, the SH-PEG solution was dried under a stream of N_2 for 1 min and the remaining solution was wicked away. The coated stamp was then brought into contact with the gold film surface for 30 sec. After contact, the stamp was peeled away from the substrate and used to print repeatedly without re-applying additional SH-PEG ink. After patterning the SH-PEG barriers onto the surface, the IBIDI sticky-Slide $VI^{0.4}$ flow chamber was adhered to the gold slide, and the substrate was prepared as described above in the "Fabrication of RNA monolayers" section. Note that the RNA track preparation protocol used a 6 hr incubation with the DNA anchor solution rather than 12 hrs.

4.4.12 Synthesis of azide functionalized particles

First, azide-functionalized particles were synthesized by mixing 1 mg of 5-μm aminated silica beads (Bangs Laboratory) with 1 mg of N-hydroxysuccinimidyl azide heterobifunctional linker. This mixture was subsequently diluted in 100 μL of DMSO and 1 μL of a 10x diluted TEA (triethylamine) stock in DMSO. The reaction proceeded overnight for 24 hrs and the azide-modified particles were purified by adding 1 mL of DI water and centrifuging down the particles at 15,000 rpm for 5 min. The supernatant was discarded and the resulting particles were resuspended in 1 mL of DI water. This process was repeated 7 times, and during the last centrifugation step, the particles were resuspended

in 100 µL of DI water, yielding an azide-modified particle stock. The azide-modified particles were stored at 4 ºC in the dark and were used within one month of preparation.

4.4.13 Synthesis of high DNA density silica particles

High density DNA functionalized particles were synthesized by adding 5 nmoles (5 µl) of alkyne modified DNA stock solution to 5 µL of azide functionalized particles. The particles and DNA were diluted with 25 µL of DMSO and 5 µL of a 2 M triethyl ammonium acetate buffer (pH 7.0). Next, 4 µL from a 5 mM stock solution of ascorbic acid was added to the reaction as a reducing agent. Cycloaddition between the alkyne modified DNA and azide functionalized particles was initiated by adding 2 µL from a 10 mM Cu-TBTA (Tris[(1-benzyl-1*H*-1,2,3-triazol-4-yl)methyl]amine) stock solution in 55 vol % DMSO. The reaction was incubated for 24 hrs, where the resulting DNA functionalized particles were purified by centrifugation. Specifically, the particles were centrifuged at 15,000 rpm for five min; after which, the supernatant was discarded and the particles were resuspended in 1 mL of a 1x PBS and 10% Triton-X solution. This process was repeated 7 times, where the particles were resuspended in 1 mL 1x PBS only for the 4^{th}-6^{th} centrifugations. During the final centrifugation/wash, the particles were resuspended in 50 µL of 1x PBS. The high density DNA functionalized particles were stored at 4 ºC and protected from light.

4.4.14 Determining DNA particle surface density

DNA surface density on the silica particles was determined by releasing the DNA using HF etching followed by quantifying the DNA concentration with a fluorescence assay. Initially, 50 µL of DNA functionalized particles were diluted with 45 µL of PBS and 5 µL of concentrated (50% by vol) HF. After 30 min of etching, we assumed that the DNA was

fully released from the surface based on brightfield characterization of particle whittling (**Figure 4.5b**). Subsequently, the DNA concentration was quantified using a commercial fluorescence assay for detecting single stranded DNA (Quant-iT OliGreen ssDNA kit, Invitrogen) following the published product protocol. The final DNA density was calculated by determining the concentration of particle stock using a hemocytometer.

4.4.15 Determination of RNase H surface kinetics

A monolayer of RNA/DNA duplexes was constructed by hybridizing a soluble complementary DNA strand to the RNA monolayer. Briefly, 100 µL of a DNA stock solution (100 µM) in 1x PBS was added to the ssRNA surface. After 1 hour of hybridization, the excess DNA was washed away by rinsing the channel with 5 mL 1xPBS, which was exchanged for 100 µL of RNase H reaction buffer (25 mM Tris pH 8.0, 8 mM NaCl, 37.5 mM KCl, 1.5 mM $MgCl_2$, 10 vol % formamide, and 0.75% (g/mL) Triton X). The RNA hydrolysis reaction was initiated by the addition of 2 µL (5 units) of RNase H from an enzyme stock of 7.2 µM (2.5 units/µL) enzyme, 500 µM DTT, and 1x PBS. Reaction progress was monitored by measuring the loss in surface RNA fluorescence over time. Since kinetic conditions satisfy Michaelis-Menten requirements with substrate RNA concentration at a ~60 fold excess over enzyme (1.2 nM), we determined k_{cat} by dividing the initial rate of reaction (V_{max}) by enzyme concentration ($V_{max} = k_{cat}$ x [enzyme]).[37]

4.4.16 RNase H powered particle translocation

Initially, RNA substrate surfaces were washed with 5 mL of PBS to wash away excess unbound RNA. Next, DNA functionalized particles were hybridized to the RNA substrate. Briefly, 5 µL of DNA functionalized particles were diluted with 45 µL of PBS, which was added to the RNA substrate. Hybridization between the particles and the complementary

RNA monolayer occurred over a thirty minute incubation period. After hybridization, particle translocation was initiated by buffer exchange with 100 µL of RNase H reaction buffer (25 mM Tris pH 8.0, 8 mM NaCl, 37.5 mM KCl, 1.5 mM $MgCl_2$, 10% formamide, and 0.75% (g/mL) Triton X) and 2 µL (5 units) of RNase H from an enzyme stock of 7.2 µM enzyme, 500 µM DTT, and 1x PBS. The microchannel was sealed with Parafilm to prevent evaporation. Particle tracking was achieved through brightfield imaging acquired at 5 sec intervals using MOSAIC imageJ plugin.[19] High-resolution epifluorecence images (100x) of fluorescence depletion tracks were acquired to verify particle motion was due to processive RNA hydrolysis. For high-resolution movies (100x), both brightfield and epifluorescence images were recorded at 5 sec intervals. For control (blocked) particles, after DNA particle hybridization with the surface, the remaining ssDNA on the particle was hybridized with a blocking strand (100 µM) in 1x PBS for 30 minutes. Prior to buffer exchange, the particles were carefully washed with 2 mL PBS to remove excess DNA blocking strand. For particle motion along RNA patterned tracks, a higher salt concentration of 150 mM KCl was used.

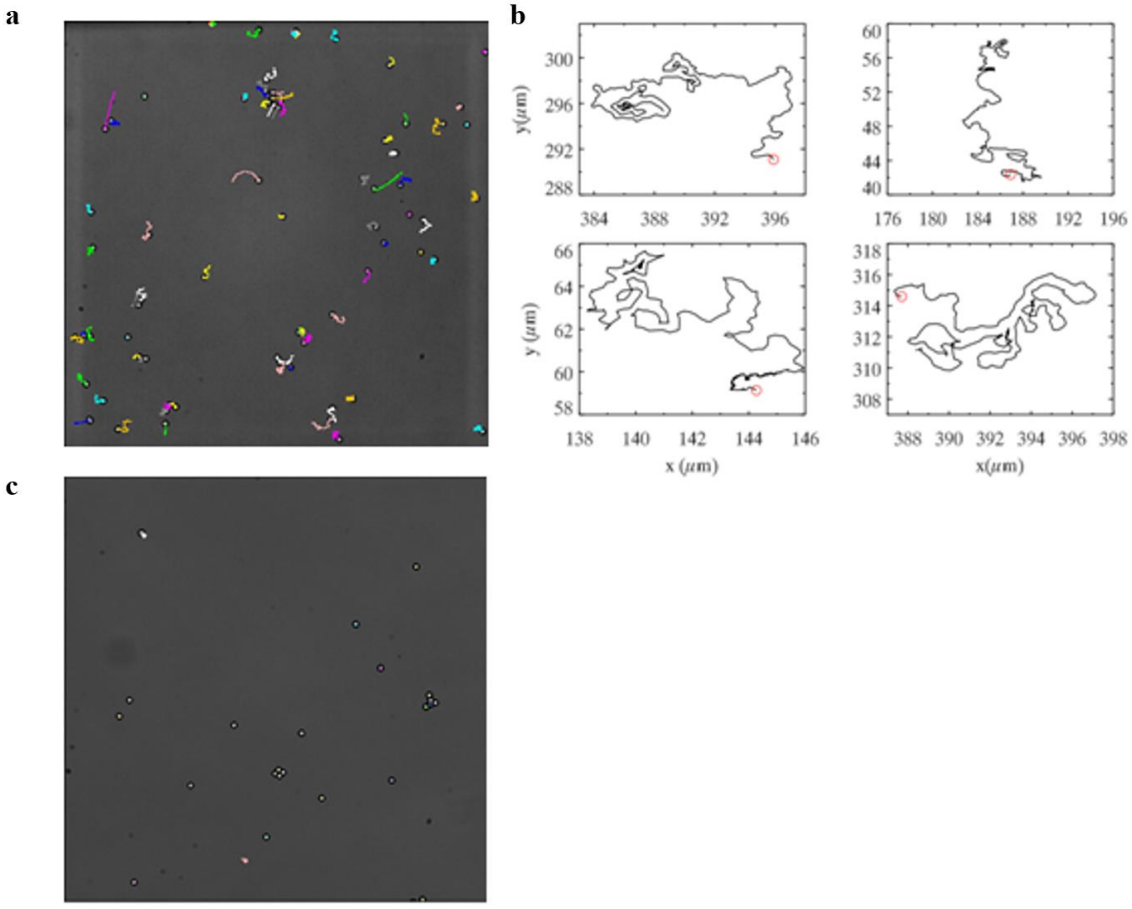

Figure 4.30. (**a**) Representative BF image superimposed with particle trajectories acquired over a 30 min duration following addition of RNase H. The time-lapse was collected at 5 s intervals and shows that the majority (>90%) of particles moved following RNase H addition. The colors are randomly assigned to different particle trajectories. (**b**) Representative zoomed in particle trajectories from **a** showing the self-avoiding diffusion of particles. (**c**) Representative BF image superimposed with particle trajectories when the RNA substrate is replaced with a DNA substrate. Note that none of the particle moved following RNase H addition.

4.4.17 Smartphone based SNP detection

Two focusing lenses (obtained from toy laser pointer, $2) were taped together and adhered to the cell phone camera via double sided tape. The smartphone was placed onto a lab jack, which was used to focus onto the sample. The sample was placed onto an optically transparent plastic sheet, where a battery powered LED was positioned underneath for illumination. Tape was used to immobilize both the smartphone to the jack

and the sample to the plastic sheet in order to minimize drift. Using the smartphone application Lapse It Pro, images were acquired at the desired time intervals, where the displacements were subsequently measured using ImageJ image processing software. The reaction buffer required higher salt concentrations (75 mM Tris pH 8.0, 110 mM KCl, and 4.5 mM $MgCl_2$) due to the lower stability of the shorter sequences used in the SNP assay.

4.5 References

(1) He, Y.; Liu, D. R. Autonomous multistep organic synthesis in a single isothermal solution mediated by a DNA walker. *Nat Nanotechnol* **2010**, *5*, 778.

(2) Lewandowski, B.; De Bo, G.; Ward, J. W.; Papmeyer, M.; Kuschel, S.; Aldegunde, M. J.; Gramlich, P. M.; Heckmann, D.; Goldup, S. M.; D'Souza, D. M.; Fernandes, A. E.; Leigh, D. A. Sequence-specific peptide synthesis by an artificial small-molecule machine. *Science* **2013**, *339*, 189.

(3) von Delius, M.; Geertsema, E. M.; Leigh, D. A. A synthetic small molecule that can walk down a track. *Nature chemistry* **2010**, *2*, 96.

(4) Paxton, W. F.; Sundararajan, S.; Mallouk, T. E.; Sen, A. Chemical locomotion. *Angewandte Chemie* **2006**, *45*, 5420.

(5) Pavlick, R. A.; Sengupta, S.; McFadden, T.; Zhang, H.; Sen, A. A polymerization-powered motor. *Angewandte Chemie* **2011**, *50*, 9374.

(6) Orozco, J.; Garcia-Gradilla, V.; D'Agostino, M.; Gao, W.; Cortes, A.; Wang, J. Artificial enzyme-powered microfish for water-quality testing. *ACS nano* **2013**, *7*, 818.

(7) Gu, H.; Chao, J.; Xiao, S. J.; Seeman, N. C. A proximity-based programmable DNA nanoscale assembly line. *Nature* **2010**, *465*, 202.

(8) Lund, K.; Manzo, A. J.; Dabby, N.; Michelotti, N.; Johnson-Buck, A.; Nangreave, J.; Taylor, S.; Pei, R.; Stojanovic, M. N.; Walter, N. G.; Winfree, E.; Yan, H. Molecular robots guided by prescriptive landscapes. *Nature* **2010**, *465*, 206.

(9) Wickham, S. F.; Endo, M.; Katsuda, Y.; Hidaka, K.; Bath, J.; Sugiyama, H.; Turberfield, A. J. Direct observation of stepwise movement of a synthetic molecular transporter. *Nat Nanotechnol* **2011**, *6*, 166.

(10) Omabegho, T.; Sha, R.; Seeman, N. C. A bipedal DNA Brownian motor with coordinated legs. *Science* **2009**, *324*, 67.

(11) Wickham, S. F.; Bath, J.; Katsuda, Y.; Endo, M.; Hidaka, K.; Sugiyama, H.; Turberfield, A. J. A DNA-based molecular motor that can navigate a network of tracks. *Nat Nanotechnol* **2012**, *7*, 169.

(12) Cha, T. G.; Pan, J.; Chen, H. R.; Salgado, J.; Li, X.; Mao, C. D.; Choi, J. H. A synthetic DNA motor that transports nanoparticles along carbon nanotubes. *Nat Nanotechnol* **2014**, *9*, 39.

(13) Yin, P.; Choi, H. M. T.; Calvert, C. R.; Pierce, N. A. Programming biomolecular self-assembly pathways. *Nature* **2008**, *451*, 318.

(14) Bath, J.; Green, S. J.; Turberfield, A. J. A free-running DNA motor powered by a nicking enzyme. *Angew Chem Int Edit* **2005**, *44*, 4358.

(15) Pei, R.; Taylor, S. K.; Stefanovic, D.; Rudchenko, S.; Mitchell, T. E.; Stojanovic, M. N. Behavior of polycatalytic assemblies in a substrate-displaying matrix. *Journal of the American Chemical Society* **2006**, *128*, 12693.

(16) Perl, A.; Gomez-Casado, A.; Thompson, D.; Dam, H. H.; Jonkheijm, P.; Reinhoudt, D. N.; Huskens, J. Gradient-driven motion of multivalent ligand molecules along a surface functionalized with multiple receptors. *Nature chemistry* **2011**, *3*, 317.

(17) Fang, S.; Lee, H. J.; Wark, A. W.; Kim, H. M.; Corn, R. M. Determination of ribonuclease H surface enzyme kinetics by surface plasmon resonance imaging and surface plasmon fluorescence spectroscopy. *Analytical chemistry* **2005**, *77*, 6528.

(18) Yehl, K.; Joshi, J. P.; Greene, B. L.; Dyer, R. B.; Nahta, R.; Salaita, K. Catalytic deoxyribozyme-modified nanoparticles for RNAi-independent gene regulation. *ACS nano* **2012**, *6*, 9150.

(19) Sbalzarini, I. F.; Koumoutsakos, P. Feature point tracking and trajectory analysis for video imaging in cell biology. *J Struct Biol* **2005**, *151*, 182.

(20) Gal, N.; Lechtman-Goldstein, D.; Weihs, D. Particle tracking in living cells: a review of the mean square displacement method and beyond. *Rheol Acta* **2013**, *52*, 425.

(21) Domb, C.; Gillis, J.; Wilmers, G. On Shape and Configuration of Polymer Molecules. *P Phys Soc Lond* **1965**, *85*, 625.

(22) Amit, D. J.; Parisi, G.; Peliti, L. Asymptotic-Behavior of the True Self-Avoiding Walk. *Phys Rev B* **1983**, *27*, 1635.

(23) Obukhov, S. P.; Peliti, L. Renormalization of the True Self-Avoiding Walk. *J Phys a-Math Gen* **1983**, *16*, L147.

(24) Family, F.; Daoud, M. Experimental Realization of True Self-Avoiding Walks. *Phys Rev B* **1984**, *29*, 1506.

(25) Diehl, M. R.; Zhang, K.; Lee, H. J.; Tirrell, D. A. Engineering cooperativity in biomotor-protein assemblies. *Science* **2006**, *311*, 1468.

(26) Kuijk, A.; van Blaaderen, A.; Imhof, A. Synthesis of Monodisperse, Rodlike Silica Colloids with Tunable Aspect Ratio. *Journal of the American Chemical Society* **2011**, *133*, 2346.

(27) Asenath-Smith, E.; Chen, W. How To Prevent the Loss of Surface Functionality Derived from Aminosilanes. *Langmuir* **2008**, *24*, 12405.

(28) Ostergaard, M. E.; Southwell, A. L.; Kordasiewicz, H.; Watt, A. T.; Skotte, N. H.; Doty, C. N.; Vaid, K.; Villanueva, E. B.; Swayze, E. E.; Bennett, C. F.; Hayden, M. R.; Seth, P. P. Rational design of antisense oligonucleotides targeting single nucleotide polymorphisms for potent and allele selective suppression of mutant Huntingtin in the CNS. *Nucleic Acids Res* **2013**, *41*, 9634.

(29) Berna, J.; Leigh, D. A.; Lubomska, M.; Mendoza, S. M.; Perez, E. M.; Rudolf, P.; Teobaldi, G.; Zerbetto, F. Macroscopic transport by synthetic molecular machines. *Nat Mater* **2005**, *4*, 704.

(30) Eelkema, R.; Pollard, M. M.; Vicario, J.; Katsonis, N.; Ramon, B. S.; Bastiaansen, C. W. M.; Broer, D. J.; Feringa, B. L. Nanomotor rotates microscale objects. *Nature* **2006**, *440*, 163.

(31) Liu, Y.; Flood, A. H.; Bonvallett, P. A.; Vignon, S. A.; Northrop, B. H.; Tseng, H. R.; Jeppesen, J. O.; Huang, T. J.; Brough, B.; Baller, M.; Magonov, S.; Solares, S. D.; Goddard, W. A.; Ho, C. M.; Stoddart, J. F. Linear artificial molecular muscles. *Journal of the American Chemical Society* **2005**, *127*, 9745.

(32) Wang, W.; Chiang, T. Y.; Velegol, D.; Mallouk, T. E. Understanding the Efficiency of Autonomous Nano- and Microscale Motors. *Journal of the American Chemical Society* **2013**, *135*, 10557.

(33) Slade, G. Self-Avoiding Walks. *Math Intell* **1994**, *16*, 29.

(34) Sponer, J.; Mladek, A.; Sponer, J. E.; Svozil, D.; Zgarbova, M.; Banas, P.; Jurecka, P.; Otyepka, M. The DNA and RNA sugar-phosphate backbone emerges as the key player. An overview of quantum-chemical, structural biology and simulation studies. *Physical Chemistry Chemical Physics* **2012**, *14*, 15257.

(35) Peterson, A. W.; Heaton, R. J.; Georgiadis, R. M. The effect of surface probe density on DNA hybridization. *Nucleic Acids Res* **2001**, *29*, 5163.

(36) Yan, L.; Zhao, X. M.; Whitesides, G. M. Patterning a preformed, reactive SAM using microcontact printing. *J Am Chem Soc* **1998**, *120*, 6179.

(37) Johnson, K. A.; Goody, R. S. The Original Michaelis Constant: Translation of the 1913 Michaelis-Menten Paper. *Biochemistry-Us* **2011**, *50*, 8264.

Chapter 5: Conclusion and Perspectives

5.1 Summary

5.1.1 DzNP model systems and their applications towards gene regulation

Confined catalytic reactions have been shown to have disruptive impacts on many different technologies (**Chapter 1**). However, controlling such reactions and predicting their properties still remains elusive. In this dissertation, I have described developments of two model systems in the hopes of expanding upon our understanding of surface confined enzymatic reactions. Both model systems possess unique emergent properties transcending that of individual enzymes due to their collective enzyme activity. In **Chapter 2**, we systematically studied the effects that Dz packing density and linker length on enzyme activity when immobilized onto a nanoparticle. Studying this model system, we were able to synthesize highly active and stable catalytic particles that could be used as a potent gene regulation therapeutic through a mechanism independent of RNAi. Specifically, we showed that DzNPs can down-regulate GDF15 mRNA expression by 60% in a cell culture model. In **Chapter 3**, we expanded upon these studies using a more therapeutically relevant model and showed that DzNPs are highly modular in that they can regulate TNFα protein expression by targeting the corresponding mRNA in primary rat macrophages. This is particularly impressive in that macrophages are a challenging target for gene regulation because of their biological role in digesting and degrading foreign objects. We further highlighted the therapeutic efficacy of DzNPs using a rat model showing that these particles can down-regulate TNFα mRNA to reduce inflammation post cardiac infarction. Rats with a surgically-induced cardiac infarction and treated with DzNPs specific towards TNFα mRNA led to a ~40% improvement in heart function as determined by fractional

shortening measurements of the infarct tissue. These studies represent initial works demonstrating the therapeutic potential of DzNPs.

5.1.2 DNA-based monowheels

Motivated by the multitude of multivalent interactions found in nature, we were next curious about the physical properties of catalytic particles exposed to substrate that was also surface immobilized. In this model system, we anticipated that the particles would move along the surface and could even follow a substrate patterned track through a 'burnt bridge' mechanism. However, due to the concern over the modest RNA hydrolysis rate of individual DNAzymes when immobilized onto a particle and the known trade-off for multivalent systems in that k_{off} slows down, we chose to investigate an alternate enzyme, RNase H (**Chapter 4**). RNase H is a highly efficient ribo-endonuclease enzyme that catalyzes RNA hydrolysis initiated by DNA hybridization. Specifically, it selectively hydrolyzes RNA when duplexed with DNA. Therefore, in the presence of RNase H, we expected DNA coated particles when exposed to immobilized RNA would function as a particle motor powered by RNA hydrolysis. Inspired by how motor proteins are driven by rapid ATP hydrolysis, up to 100 s^{-1}, we anticipated that RNase H powered particle motors could approach velocities similar to that of motor proteins since the rate of RNA hydrolysis catalyzed by RNase H is very efficient, approximately 10 s^{-1}.[1,2] In addition to being driven by a very efficient enzyme, we were also inspired by the mechanism in how cells translocate with high processivity, which requires coordinated, parallel activity of highly multivalent focal adhesion contacts bound to the extracellular matrix.[3] Therefore, we designed a massively multivalent DNA-based motor containing up to ~5,000 DNA-RNA duplexes at the particle-surface junction. We expected that

such massive multivalency would greatly enhance motor processivity and fidelity and enable particles to translocate through a rolling mechanism, which is a fundamentally distinct type of movement that can overcome the inherent tradeoffs of multivalent motors.[4-6]

Specifically, we showed that these particle motors do indeed translocate through a rolling mechanism, which is why we termed them DNA monowheels (DMWs). We found that the DMWs could reach rapid speeds up to 5 μm/min and processivity of several hundreds of μm's, thus approaching the capabilities of biological motor proteins. Because of the bead size, motor displacements were accurately tracked, allowing quantification of diffusion behavior. This analysis showed that this was the first experimental realization for self-avoiding diffusion, which we leveraged to control motor translocation along micro-patterned tracks. Moreover, due to the rolling mechanism, we were able to program DMWs to move in a linear fashion by incorporating anisotropy into the particle structure. This was the first example of directional without influence from an external field or patterned track. Because of the motor robustness, size, and molecular sensitivity, DNA monowheels could even be used to detect single nucleotide mutations using a simple smartphone readout, thus demonstrating the simplicity and usefulness of DNA-based motors towards real world applications.

5.2 Future Outlook

5.2.1 Other Enzymatic reactions

These two model systems (DzNPs and DMWs) demonstrate the emergent properties resulting from localizing ribonuclease reactions at surfaces. However, there are many other classes of enzymes to be explored. For example, a DNAzyme with nuclease activity was recently discovered and could have major implications towards regulating gene expression at the DNA level, although delivery past the nuclear envelope will be a significant hurdle.[7] However, bacteria do not possess

nuclei, therefore, nanoparticles functionalized with this class of DNAzyme targeting antibiotic resistant genes may have major implications in treating drug resistant bacteria. Along the same theme, other enzyme based monowheels could be studied, such as lipase, protease, kinase or phosphatase based monowheels. These constructs may surpass the speeds of DMWs or even that of biological motors.[8] Also, these motors may offer unique properties that have applications towards drug delivery or alternative therapies. However, these future directions involve simple model systems, in that they study confinement of single enzymes (solely DNAzymes or biological enzymes). A more interesting approach may be to combine both DNAzymes and biological enzymes into a single multi-enzyme construct.

5.2.2 Multi-enzyme model systems

5.2.2.1 Applications towards sensing

Multi-enzyme model systems can greatly expand upon the complexity of the constructs described in **Chapters 2-4**, thus more accurately recapitulating living systems and providing emergent properties that neither system alone possesses. For example, we have demonstrated that DMWs are an excellent platform for detection using a simple smartphone readout. However, this sensing platform can only detect single nucleotide mutations and expanding the scope of molecular inputs would greatly broaden its impact. One such strategy could be to incorporate a DNAzyme-based sensing domain because many sensing assays have already been developed using DNAzymes owing to their inherent properties: metal selectivity, catalytic amplification, and stability. However, DNAzyme based monowheels would require long response times to detect motor displacements because of the modest catalytic activity of DNAzymes. In addition, a highly multivalent interaction with the surface would limit motor sensitivity. However, a multifunctional particle modified with both RNase H antisense strands along with DNAzymes would provide a

synergistic solution to this problem, where only in the presence of the DNAzyme metal cofactor could the motor rapidly translocate. Such a sensing assay would greatly broaden the scope of DMWs to detect the myriad of metal cofactors (Hg^{2+}, Pb^{2+}, UO^{2+}, Mn^{2+}…).[9]

Moreover, based on a similar design, co-modification of DMWs with other functional nucleic acids, such as aptamers or aptazymes, could even further expand the DMW scope to detecting small molecules and proteins. Such a construct would take advantage of the fact that DMWs are highly sensitive to the local surface binding kinetics (k_{on} and k_{off}), and depending on the DMW design, the aptamers or aptazymes could function as molecular brakes or accelerators. Due to the motor's robustness and ability to be imaged using a smartphone, we believe that DMW–based sensors will have a major impact in tracking industrial contaminations and spread of diseases in remote locations.

5.2.2.2 Applications towards gene editing

Confined multi-enzyme networks are vital to living systems because they play a key role in enhancing cascading reactions through substrate shuttling and increasing local substrate concentrations. Many groups have replicated this phenomenon by controlling the distance between enzymes or enzymes and cofactors using synthetic scaffolds.[10,11] However, extending this concept to DNAzyme-enzyme cascades can broaden the scope chemical reactions and can even have a major impact on the field of gene editing. By templating a hydrolytic DNAzyme with a ligase enzyme onto a synthetic scaffold, one could rationally edit genetic mutations in a highly modular fashion (**Figure 5.1**). The current gold standard in gene editing technology involves the CRISPR/Cas9 system, which is a multi-enzyme cascade that targets DNA and is highly programmable by simply altering the sequence of the RNA guide strand.[12] However, this technique suffers the challenges of being low yielding, having off targeting effects, and delivery issues. A

multi-DNAzyme/enzyme scaffold may address these limitations by enabling high transfection efficiency due to the polyvalent DNAzyme scaffold, increased reaction yield by scaffolding enzymes together, and being highly selective due to the inherent properties of DNAzymes.

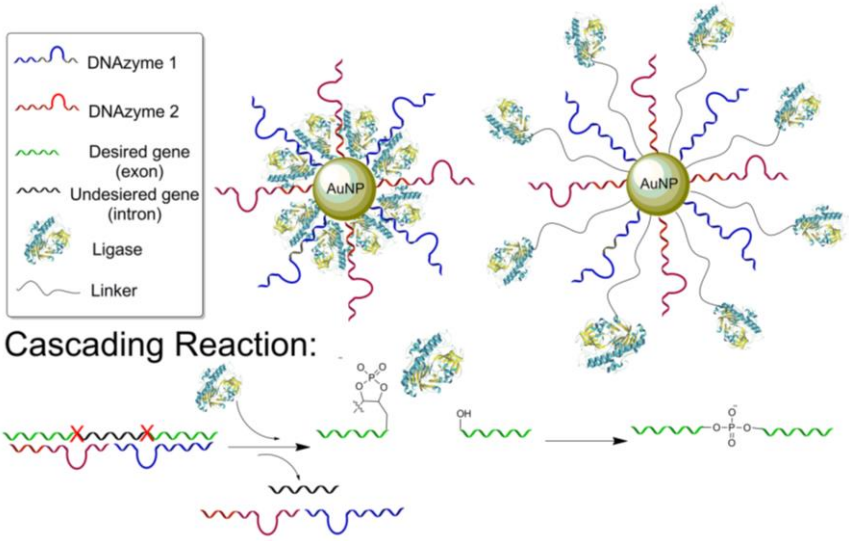

Figure 5.1. Schematic of a mutli-enzyme gene editing complex with varying geometrical configurations where the ligase enzyme is either directly functionalized to the gold nanoparticle or immobilized using a long linker such that it forms an outer layer.

5.3 References

(1) Fang, S.; Lee, H. J.; Wark, A. W.; Kim, H. M.; Corn, R. M. Determination of ribonuclease H surface enzyme kinetics by surface plasmon resonance imaging and surface plasmon fluorescence spectroscopy. *Analytical chemistry* **2005**, *77*, 6528.

(2) Coy, D. L.; Wagenbach, M.; Howard, J. Kinesin takes one 8-nm step for each ATP that it hydrolyzes. *J Biol Chem* **1999**, *274*, 3667.

(3) Kim, D. H.; Wirtz, D. Focal adhesion size uniquely predicts cell migration. *Mol Biol Cell* **2012**, *23*.

(4) Pei, R.; Taylor, S. K.; Stefanovic, D.; Rudchenko, S.; Mitchell, T. E.; Stojanovic, M. N. Behavior of polycatalytic assemblies in a substrate-displaying matrix. *Journal of the American Chemical Society* **2006**, *128*, 12693.

(5) Lund, K.; Manzo, A. J.; Dabby, N.; Michelotti, N.; Johnson-Buck, A.; Nangreave, J.; Taylor, S.; Pei, R. J.; Stojanovic, M. N.; Walter, N. G.; Winfree, E.; Yan, H. Molecular robots guided by prescriptive landscapes. *Nature* **2010**, *465*, 206.

(6) Perl, A.; Gomez-Casado, A.; Thompson, D.; Dam, H. H.; Jonkheijm, P.; Reinhoudt, D. N.; Huskens, J. Gradient-driven motion of multivalent ligand molecules along a surface functionalized with multiple receptors. *Nature chemistry* **2011**, *3*, 317.

(7) Chandra, M.; Sachdeva, A.; Silverman, S. K. DNA-catalyzed sequence-specific hydrolysis of DNA. *Nat Chem Biol* **2009**, *5*, 718.

(8) Saffarian, S.; Collier, I. E.; Marmer, B. L.; Elson, E. L.; Goldberg, G. Interstitial collagenase is a Brownian ratchet driven by proteolysis of collagen. *Science* **2004**, *306*, 108.

(9) Zhang, X. B.; Kong, R. M.; Lu, Y. Metal Ion Sensors Based on DNAzymes and Related DNA Molecules. *Annual Review of Analytical Chemistry, Vol 4* **2011**, *4*, 105.

(10) Fu, J. L.; Yang, Y. R.; Johnson-Buck, A.; Liu, M. H.; Liu, Y.; Walter, N. G.; Woodbury, N. W.; Yan, H. Multi-enzyme complexes on DNA scaffolds capable of substrate channelling with an artificial swinging arm. *Nat Nanotechnol* **2014**, *9*, 531.

(11) Fu, J. L.; Liu, M. H.; Liu, Y.; Yan, H. Spatially-Interactive Biomolecular Networks Organized by Nucleic Acid Nanostructures. *Accounts Chem Res* **2012**, *45*, 1215.

(12) Ran, F. A.; Hsu, P. D.; Wright, J.; Agarwala, V.; Scott, D. A.; Zhang, F. Genome engineering using the CRISPR-Cas9 system. *Nat Protoc* **2013**, *8*, 2281.